

International Journal of Thermodynamics

Editor-in-Chief

L. Kuddusi

Honorary Editors

A. Bejan

M. J. Moran

J. Szargut

G. Tsatsaronis

A. Valero

M. R. von Spakovsky

Abstracting and Indexing:

Chemical Abstracts Services, Copernicus, DOAJ, EBSCO, Emerging Sources Citation Index, Engineering Index, Google Scholar, Scopus, and ULAKBIM



*International Centre for
Applied Thermodynamics*

Editor-in-Chief

Prof. Dr. Lütfullah KUDDUSİ

Associate Editor-in-Chief

Assoc. Prof. Dr. Patrice ESTELLÉ

Prof. Dr. Enrico SCIUBBA

Associate Editor

Prof. Dr. Ali KOSAR

Prof. Dr. Derya Burcu ÖZKAN

Prof. Dr. Mustafa ÖZDEMİR

Prof. Dr. Ahmet DURMAYAZ

Assoc. Prof. Dr. Onur TAYLAN

Prof. Dr. Mehmet ARİK

Prof. Dr. Ayşegül ABUŞOĞLU

Prof. Dr. G. Reza VAKİLİ-NEZHAAD

Prof. Dr. Bayram ŞAHİN

Editorial Board

Prof. Dr. Yasar DEMİREL

Prof. Dr. Lütfullah KUDDUSİ

Prof. Dr. Ahmet DURMAYAZ

Prof. Dr. Derya Burcu ÖZKAN

Prof. Dr. Mustafa ÖZDEMİR

Prof. Dr. Ali KOSAR

Assoc. Prof. Dr. Ersin SAYAR

Prof. Dr. Mehmet ARİK

Assoc. Prof. Dr. Abdussamet SUBASI

Daniel FAVRAT

Francois MARECHAL

Prof. Silvia Azucena NEBRA

Luis SERRA

Assoc. Prof. Dr. Onur TAYLAN

Prof. Dr. Ayşegül ABUŞOĞLU

Vittorio VERDA

Gian Paolo BERETTA

Abel HERNANDEZ-GUERRERO

Nilufer EGRİCAN

Dr. Sean WRIGHT

Prof. Dr. Hakan Fehmi ÖZTOP

Prof. Dr. Enrico SCIUBBA

Prof. Dr. G. Reza VAKİLİ-NEZHAAD

Prof. Dr. Bayram ŞAHİN

Publishing Editor

Assoc. Prof. Dr. Abdussamet SUBASI

Dr. Mustafa Yasin GÖKASLAN

Res. Assist. Ali Murat BİNARK

Language Editor

Assoc. Prof. Dr. Abdussamet SUBASI

Journal Contacts

Editor-in-Chief

Prof. Dr. Lütfullah Kuddusi

ISTANBUL TECHNICAL UNIVERSITY

kuddusi@itu.edu.tr

+902122931300/2452

Department of Mechanical Engineering

Istanbul Technical University

Gumussuyu, 34437 Istanbul Turkey

Volume: 27

Issue: 1

Web: <https://dergipark.org.tr/tr/pub/ijot>

International Journal of Thermodynamics (IJoT)

ISSN:1301-9724 / e-ISSN:2146-1511

CONTENTS

<u>Research Article</u>	
1. Effects of Nozzle Diameter and Holes Number on the Performance and Emissions of a Gasoline Direct Injection Engine	1-12
O. M. Yousif, M. A. Mashkour	
<u>Research Article</u>	
2. Performance Evaluation of R1224yd as Alternative to R123 and R245fa for Vapor Compression Heat Pump System	13-21
N. Aisyah, H. M. Ariyadi	
<u>Research Article</u>	
3. Development and Economical Analysis of Innovative Parabolic Trough Collector Integrated Solar Still	22-34
M. Patil, I. Patil, S. Shekhawat, N. Nikam	
<u>Research Article</u>	
4. Computational Fluid Dynamics Analysis of a Solar Dryer with Various Phase Change Materials	35-42
C. Mamulkar, S. Ikhar, V. Katekar	
<u>Research Article</u>	
5. Use the Thermodynamic State Equations to Analyze the Non-ideality of Gas Mixtures	43-50
N. Manuel, T.C.F.S. Major, S.M. Pedro, A.A.C. Barros	
<u>Research Article</u>	
6. Pressure Effect on Thermodynamic Quantities for the Solid-Liquid Phase Transition in n-tridecane, n-hexadecane and n-octadecane	51-63
O. Tari, H. Yurtseven	
<u>Research Article</u>	
7. Thermodynamic Modeling of Solubility of Some Antibiotics in Supercritical Carbon Dioxide Using Simplified Equation of State Approach	64-71
G. Mahesh, C. Garlapati	

Research Article

Effects of Nozzle Diameter and Holes Number on the Performance and Emissions of a Gasoline Direct Injection Engine

¹*O. M. Yousif , ²M. A. Mashkour 

¹Mechanical Engineering Department, University of Technology -Iraq

²Mechanical Engineering Department, University of Technology -Iraq

E-mails: ¹*21980@student.uotechnology.edu.iq, ²Mahmoud.A.Mashkour@uotechnology.edu.iq

Received 29 March 2023, Revised 27 June 2023, Accepted 27 September 2023

Abstract

The goal of the current study is to estimate how a gasoline direct injection (GDI) engine's performance and emissions are affected by the fuel injector nozzle diameter and hole number of its injectors. A thermodynamic mathematical modelling has been created utilizing a software program written in the MATLAB language to simulate the two-zone combustion process of a four-stroke direct injection engine running on gasoline at (Rotation Engine Speed 3000 revolution per minute (rpm), 40 MPa injection pressure, compression ratio 9.5, and spark timing 145°). The first law of thermodynamics, equation of energy, mass conserving, equation of state, and mass fraction burned were all used in the creation of the software program. The study was carried out at five different nozzle diameters (0.250, 0.350, 0.450, 0.550, and 0.650 mm) and nozzle hole numbers (4,6,8,10,12). The results show that the GDI engine's performance and emissions are significantly influenced by variations in nozzle hole diameter and number. It was shown that engine power, heat transfer, cylinder pressure, and temperature increased with increasing nozzle hole diameter and number of nozzle holes and the maximum value was seen with nozzle hole diameter 0.650 mm and (12) holes. The lowest value for the nozzle hole diameter and number of holes was found to be 0.250 mm and 4 nozzle holes, which resulted in the lowest emissions of carbon monoxide CO and nitrogen monoxide NO. The study was also conducted for different operating conditions (Rotation Engine speed of 1000, 2000, 3000, 4000, 5000 rpm, 35 MPa injection pressure, compression ratio of 11.5, and spark timing of 140°) and the same nozzle diameters and nozzle holes number mentioned previously to estimate the maximum values for temperature, pressure, power, heat transfer and emissions. The results of the second part of the study showed that the highest of maximum values of temperature, pressure, and emissions were at of 1000 rpm, a nozzle diameter of 0.650 mm, and (12) holes. The highest values for maximum power at 4000 rpm, a nozzle diameter of 0.650 mm and (12) holes, while the highest maximum values for heat transfer are at 5000 rpm, a diameter of 0.65mm and (12) holes.

Keywords: Gasoline direct injection engine (GDI); nozzle diameter; hole number; mathematical model; performance; emissions.

1. Introduction

(GDI) engine technology has sparked considerable interest in recent years due to its several advantages over traditional fuel injection (PFI) engines, including reduced fuel consumption, improved efficiency, and lower hazardous emissions to comply with environmental requirements [1], [2]. Although GDI engines provide rapid reaction and flexible control, several aspects impact engine performance and engine emissions, including ignition and injection timings, injection pressure, injection duration, diameter of nozzles, and aperture numbers, among others. Studying combustion engines experimentally is a very challenging issue because of the sophisticated experimental facilities that are required to perform the experiments. Therefore, researchers tend to perform theoretical or analytical analyses such as simulation and numerical analysis before conducting any experimental activity.

Cost and time may be saved by using a simulation approach that enables GDI engine designers to adjust and examine a variety of factors with no need to actually create

any real part or even an entire engine. Numerous mathematical models, including combustion phasing modeling, thermophysical property models, injector models, and flow models into and out of a cylinder engine, have been developed to aid in understanding, correlating, and investigating the process of engine cycles [3].

The impact of engine settings on a DI engine's performance and emission characteristics has been examined in several studies related to diesel and gasoline. Kumbhar *et al.* [4] used computation fluid dynamics CFD codes with a combustion model to test four different nozzle throat diameters and their influence upon the engine performance, emissions, as well as spraying features. They discovered that improvements in spray cone angle, fuel atomization, and effective air-fuel mixture resulted to a 0.230 mm nozzle throat diameter, which led to the highest in-cylinder temperatures and pressures. Hydrocarbon (HC), Carbon monoxide (CO), and soot emission got decreased as nozzle hole diameter dropped; nevertheless, Nitric oxide (NO) emissions were reported to rise because of improved

atomizing as well as a general increase within cylinder gas temperatures of nozzle holes by smaller sizes. As a result, nozzle throats having smaller diameters have a tendency to lower emission at the cost of increased NO_x emission. Lee *et al.* [5] investigated the development of fuel spray-air mixing, combustion, and emitting as the number of injector throats changed. The researchers found that there is an optimal number of holes for better efficiency and emission of the diesel engine. Furthermore, the findings demonstrate that evaporating, atomizing, and combustion are significantly impacted by the amount of holes present. On the other hand, when the number of injector holes exceeds a certain limit, the combustion and emissions deteriorate as a result of an absence of air entraining necessary to create a stoichiometric mixture. By using a flux dynamometer, a four-stroke single-cylinder diesel engine, a water-cooled direct injection diesel engine operated by computer, a typical injection timescale of 23° before top dead center (BTDC), and a variety of throat diameters, Kumar *et al.* [6] studied the performance, combustion, and emitting of the engine for the different nozzles hole dimension (3 holes × Ø = 0.20 mm), (3 holes × Ø = 0.28 mm) and (3 holes × Ø = 0.20 mm) as shown in figure 1. The results of this study showed that among all different nozzle throats, the 3 holes × Ø = 0.20 mm (adapted) improved the time. The findings were outstanding in terms of performance, combustion, and emitting. The only disadvantage was that NO_x numbers rise when the aperture nozzle hole size is reduced.

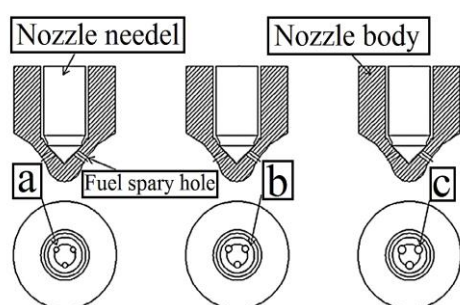


Figure 1. Schematic drawing of 3-holes of different nozzle diameters (a) Ø = 0.20 mm, (b) Ø = 0.28 mm, (c) Ø = 0.31 mm.

Jiang C and Parker M., *et al.* [7] studied the influence of injection nozzle design upon the (GDI) engine fuel spray features. Inside a pressure- and temperature-controlled constant volume chamber as well as outside, testing on two custom three-hole injectors were carried out. The measuring was made at intervals of 15 mm, 25 mm, and 40 mm from the injection tip, radially outwards from the injection axis to the external edge of the jet. The researchers found that the spray penetration length before collapsing is determined by the injection pressure rise within extending such length. To understand the performance during flash boiling circumstances, average velocity and droplet diameter information were also studied. Additionally, the results showed that droplet size decreases whereas droplet velocity greatly rises during flash boiling circumstances. Researchers discovered that various hole geometries had distinct effects on sprays when exposed to a flash boiling setting. Some hole configurations provide more protection from spray collapsing. The researchers discovered that the spray produced by the middle of the three-hole sizes studied dispersed more easily than the spray produced by either smaller and greater hole diameters. Moreover, the convergent hole was more likely to show spray collapsing

during flash boiling circumstances. Ahmed and Mekonen [8] conducted a simulation study by using ANSYS the influence of different injector nozzle hole numbers (INHNs) and fuel injection pressures (IPs) of the performance, and emissions characteristics of engine. The study performed for different fuel IPs 190, 200, 210, and 220 bar with a change of INHN of 1 (default), 3, and 4), each 0.84, 0.33, and 0.25 mm in orifice diameter, respectively as showing in figure 2. The results show the increasing of INHNs and fuel IPs have an essential improvement of atomization and mixing rates, as well as combustion and engine efficiency as well as minimize of CO and HC emissions with a small raise in NO_x.

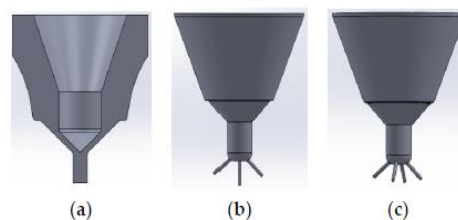


Figure 2. A diagram of fluid in nozzles: (a) single hole, (b) 3-holes, (c) 4-holes.

Reddy and Mallikarjuna [9] studied the impact of fuel injection settings on the performance, combustion, and emitting features of GDI engines by using CFD. For a variety of fuel injection pressures, spark timing, holes number, and multiple stage injection strategies, turbulence, combustion, and fuel spraying break-up analyses were carried out. The findings demonstrate that, relative to 110-bar fuel injection pressure, soot emission decreased for various fuel injection pressures by roughly 77.8 and 88.5% for 150 and 200-bar fuel injection pressures, respectively. When spark timing was advanced, the soot emission rose by an amount that was about 3.3 and 4.5 orders of magnitude more, correspondingly, at the spark time of 15° and 20° BTDC than at the spark time of 7.5° BTDC. Additionally, relative to a 6-hole injection, the soot emission is lower when 8 or 10 fuel injection holes were employed. The soot emission dropped by around 72.8 and 76.1%, correspondingly, in comparison to single-stage fuel injection, when two different multiple stage fuel injection techniques were taken into account. Eventually, it was determined that a GDI engine's preparing of the mixture and soot emission are significantly influenced by the fuel injection pressure, amount of injection holes, spark time, and multiple stage fuel injection technique. Employing (CFD) research and information from literatures, Jadhav and Mallikarjuna [10] investigated the impact of fuel injection-hole diameter and fuel injection time upon the mix formation in a four-stroke, wall-guided GDI type of engines. GDI engine at a compression ratio of 11.5. CFD simulating is run at an engine velocity of 2000 revs per minute. Three crank angle measures, three fuel injection times, as well as three fuel injection hole sizes of 0.1, 0.14, and 0.18 mm were used. The findings demonstrate that larger nozzle-hole diameters produced extremely rich mixing zones close to the spark plug. Furthermore, a greater suggested mean effective pressure was seen with a smaller nozzle-hole diameter and delayed fuel injection time.

According to the preceding discussion, numerous researchers have concentrated on various elements of engine parameters of GDI engines utilizing various approaches and

techniques. The injector setting effect upon the performance as well as emitting characteristics of a GDI engine, on the other hand, has not been well examined. As a result, the present work aims at using MATLAB to investigate such effect. This work will be useful in enhancing the GDI engine settings for optimal performance.

2. Theoretical Model

This model examines a direct injection engine. The model depends on a two-zone thermodynamic study of the combustion process, which separates the combustion chamber into burned and unburned areas. The ideal gas law is assumed for the in-cylinder gases, and the first law of thermodynamics, state equation, and mass and volume conservation are used. For the temperature, pressure, mass, and volume of the burned and unburned gases, a set of equations may be constructed. The Wiebe function has the following definition. [11]:

$$X_{b(\theta)} = 1 - \exp \left[-a \left[\frac{\theta(i) - \theta(o)}{\theta(b)} \right]^{k+1} \right] \quad (1)$$

where $\theta(i)$ represents the immediate crank angle, $\theta(o)$ represents the spark angle at the beginning of combustion, and $\theta(b)$ represents the combustion duration. The values of a and k represent adjustable constants (5 and 2 are typical values). The burn profile is engine-specific, and the constants a and k can be changed on a specific engine or application since the burn profile is engine-specific.

The following equation is created by differentiating the ideal gas equation of state:

$$\frac{dp}{d\theta} = \left(-\frac{P}{V} \right) \left(\frac{dV}{d\theta} \right) + \left(\frac{P}{T} \right) \left(\frac{dT}{d\theta} \right) \quad (2)$$

In which the instantaneous quantities P , V , T , are modeled in relation to the crank angle of the engine. The first law of thermodynamics, which has the following formal formulation, may be implemented using the same procedure:

$$\Delta U = Q - W \quad (3)$$

Here Q represents the overall heat input into the system, W represents the work output from the system, and U represents the change in internal energy inside the system. Equation 4 may be produced by diffusing "Eq. (3)" [11]:

$$\frac{dU}{d\theta} = \left(\frac{dQ}{d\theta} \right) - \left(\frac{dW}{d\theta} \right) = m C_v \left(\frac{dT}{d\theta} \right) \quad (4)$$

Here C_v denotes the specific heat of the gas in the combustion chamber. The change in temperature as a function of crank angle is given by "Eq. (5)", which we get at by dividing the specific heat by the universal gas constant, utilizing η (the combustion efficiency), and L.H.V. (the lower heating values of the provided fuel):

$$\frac{dT}{d\theta} = T(\gamma-1) \left[\left(\frac{1}{PV} \right) \left(\frac{dQ}{d\theta} \right) - \left(\frac{1}{V} \right) \left(\frac{dV}{d\theta} \right) \right] \quad (5)$$

The changing in pressure as a product of the crank angle may be determined using the heat input from the fuel. The definition of the fuel's heat input is [12]:

$$Q_{in} = \eta_c \cdot \text{LHV} \left(\frac{1}{AF_{ac}} \right) \left(\frac{P}{RT} \right) V_d \quad (6)$$

In which the actual air-fuel rate is Q_{in} in. The final definition of the pressure change would be:

$$\frac{dp}{d\theta} = \left(-\frac{\gamma P}{V} \right) \left(\frac{dV}{d\theta} \right) + \left(\frac{\gamma-1}{V} \right) Q_{in} \frac{dX_b}{d\theta} + (\gamma-1) \left(\frac{1}{V} \right) \left(\frac{dQ_w}{d\theta} \right) \quad (7)$$

"Eq. (7)" serves as the foundation for a numeric model that mimics engine performance.

2.1 Modeling Engine Friction

The Several studies, notably Heywood [11] and Blair [13], have used general linear equations to forecast Friction mean effective pressure FMEP loses like a function of rpm. Although this approach only offers rough estimates of friction loses, it serves as a starting point for a numerical simulation. The following is Blair's equation for the linear FMEP loss:

$$FMEP = a + b(L)(RPM) \quad (8)$$

In which L represents the engine's stroke [m], rpm represents the engine speed [rev/min], while a and b represent constants that depend on the type of engine. According to the engine displacement, Blair has aspired to several variations of the FMEP loss equations for a spark-ignition engine with simple internal bearings ($V_d > 500 \text{ cm}^3$) and ($V_d < 500 \text{ cm}^3$) respectively :

$$FMEP = 100000 + 350(L)(RPM) \quad (8a)$$

$$FMEP = 100000 + 100(500 - V_d) + 350(L)(RPM) \quad (8b)$$

The indicated, relative FMEP losses are given in [Pa] units.

2.2 Burned and Unburned Areas

Assumptions must be made regarding the burned and unburned areas because this model ignores heat transmission between the burned and unburned zones and doesn't explore the geometric location of the flame front. The definitions of the unburned and burned zones are given in Rakopoulos and Michos' article [14]:

$$A_u(i) = A(i) \left(1 - (X_b(i))^2 \right) \quad (9)$$

$$A_b(i) = A(i) \left(\frac{X_b(i)}{(X_b(i))^2} \right) \quad (10)$$

The mass fraction burned like a function of crank angle gets denoted by X_b . The area of the cylinder that is now in touch with combustion chamber gases is known as $A(i)$.

Although this technique ignores heat transmission between zones and presupposes a surface area of the cylinder head, it could be demonstrated to have physical consistency because the fractional heat transfer between the burned gas and the cylinder wall has always been greater in the burned region [18].

2.3 Burned, Unburned Mass, Volume, Temperature Calculations

The equation of state can be applied to the unburned and burned gas regions at any instant:

$$PV_b = m_b R_b T_b \quad (11a)$$

$$PV_u = m_u R_u T_u \quad (11b)$$

For the assumption of no mass loss from the combustion chamber, the total mass in the system at any stage can be expressed as:

$$m = m_b + m_u \quad (12)$$

The total volume at any stage

$$V = V_b + V_u \quad (13)$$

These are the main equations used; at any instant during combustion, there are seven unknown parameters to be solved ($T_b, T_u, m_b, m_u, V_b, V_u, P$). In order to solve these parameters, an extra equation that specifies the burning rate is required. In the simple form of the model, the burning rate can be expressed by the exponential form of Wiebe function "Eq. (1)",

2.4 Heat Transfer Estimation

The main modes of heat transfer from each zone are convection and radiation, this heat is determined using relationships based on the work of Annand [15]. Nusselt and Reynolds number correlations for forced convection are:

$$Nu_i = 0.94 Re^{0.7} \quad (14)$$

The coefficient of radiation heat transferring is calculated as:

$$hr = 4.25 * 10^{-9} * \left(\frac{T^4 - T_w^4}{T - T_w} \right) \quad (15)$$

Convective losses into the wall are calculated as a function of the crank angle as follows:

$$DQ_1 = (hg(i) + hr(i)) A_b(i) (T_b(i) - T_w) * \frac{60}{360 * RPM} + (hg(i) + hr(i)) A_u(i) (T_u(i) - T_w) * \frac{60}{360 * RPM} \quad (16)$$

Calculates change in heat transfer (total) as A function of crank angle

$$DQ_2 = \eta * m_f * L.H.V * Dx_i - DQ_1 \quad (17)$$

2.5 Injector Calculations

Fuel velocity in model accounts as follows [16]:

$$U_{fuel} = \frac{C_d}{C_a} \sqrt{\frac{2 * (P_{inj} - P) * 1000}{\rho_{fuel}}} \left(\frac{m}{s} \right) \quad (18)$$

The following is accounted for by mass flow ratio in kilograms per millisecond:

$$\dot{m}_f = C_a A_{inj} \rho_f U_f \text{ (kg/s)} \quad (19)$$

The following is how mass flow rate per crank angle unit is calculated:

$$\dot{m}_{CA} = \frac{\text{holes} * \dot{m}_f}{0.006 * N_s * MW_f} \left(\frac{\text{kmol}}{\text{deg}} \right) \quad (20)$$

Crank angle unit injection duration is calculated as follows:

$$dur_{CA} = \frac{m_f}{\dot{m}_{CA}} \text{ (deg)} \quad (21)$$

The following relationship is accounted for by the pressure injection for each time step:

$$P_{inj} = P_{injmin} + \left(\frac{P_{injmax} - P_{injmin}}{dur_{CA}} \right) * \theta \quad (22)$$

Where, P_{injmax} is maximum injection pressure, P_{injmin} is minimum injection pressure, and θ is crank angle.

2.6 Power, Torque, and Efficiency Calculations

The power is represented by the braking power W_b , and the engine torque τ , represents the amount of work completed per unit revolution (radians) of the crank [12].

$$\dot{W}_b = 2\pi \tau N \quad (23)$$

The network transmitted from the gas to the piston throughout a cycle is the stated work W_i , that represents the integration of the pressure over the cylinder volume.

$$W_i = \int P dV \quad (24)$$

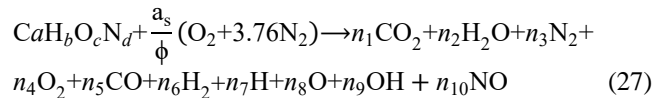
while the designated power W_i , for any engine using η_c cylinders, is

$$\dot{W}_i = \eta_c W_i N / 2 \quad (25)$$

Mechanical efficiency η_m is determined by the braking power to indicate power rate:

$$\eta_m = \frac{\dot{W}_b}{\dot{W}_i} \quad (26)$$

2.7 The Combustion Reaction (Equilibrium Equations) [17]



Where a_s and ϕ are stoichiometric air--fuel ratio and equivalence ratio. The following four formulas are produced via atom balance:

$$C: a = (y_1 + y_5) N$$

$$H: b = (2y_2 + 2y_6 + y_7 + y_9) N$$

$$O: c + \frac{2a_s}{\phi} = (2y_1 + y_2 + 2y_4 + y_5 + y_8 + y_9 + y_{10}) N$$

$$N: d + 7.52a_s / \phi = (2y_3 + y_{10}) N \quad (28)$$

where N stands for moles' total number. By definition, the mole fractions sum to 1:

$$\sum_{i=1}^{10} y_i = 1 \quad (29)$$

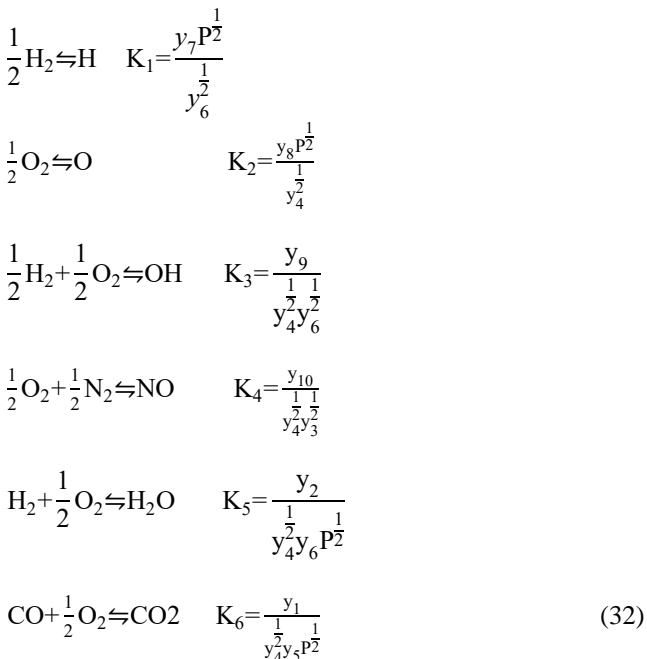
These equations define the following three constants:

$$d_1 = \frac{b}{a}, \quad d_2 = \frac{c}{a} + 2 \frac{a_s}{\phi a}, \quad d_3 = \frac{d}{a} + \frac{7.52a_s}{\phi a} \quad (30)$$

After some rearranging and replacement into the atom balancing equations, we have:

$$\begin{aligned}
 2y_1 + 2y_6 + y_7 + y_9 + d_1y_1 - d_1y_5 &= 0 \\
 2y_2 + y_2 + 2y_4 + y_5 + y_8 + y_9 + y_{10} - d_2y_1 - d_2y_5 &= 0 \\
 2y_3 + y_{10} - d_3y_1 - d_3y_5 &= 0 \\
 \sum y_i &= 1
 \end{aligned} \tag{31}$$

Six gas-phase equilibrium processes are now shown. Such reactions result in the creation of OH and NO as well as the dissociating of hydrogen, oxygen, water, and carbon dioxide:



The equilibrium constants had been curve-fit to the JANAF Table data for the temperature range $600 < T < 4000$ K by Olikara and Borman [18]. Their expressions take the following form:

$$\log_{10} K_i(T) = A_i \ln \left(\frac{T}{1000} \right) + \frac{B_i}{T} + C_i + D_i T + E_i T^2 \tag{33}$$

Where T is the temperature in kelvin, and $(A_i, B_i, C_i, D_i, E_i)$ are the curve-fitting equilibrium constants. The unburned and burned mixed zones are regarded as independent open systems according to thermal characteristics. The atom balance equations are changed to correspond to the six separate equilibrium reacting equations, resulting in four equations with four unknowns (y_3, y_4, y_5, y_6) . Such four equations have numerical solutions.

2.8 Variable Specific Heats Ratio Model

For combustion processes including iso-octane and other fuels, Krieger and Borman created this polynomial approach in 1966 [19]. The Krieger and Borman technique simulates changes in internal energy by using "correction factors" for ideal gas constants that correlate to temperature variations (based on a given reference temperature). Using this

approach and the related polynomials, it is possible to derive the exact heats rate as a temperature function.

3. MATLAB Model

Figure 3 illustrates the flow chart of the model's mathematical formulation. Sub-models are created by the primary model to carry out certain tasks. The mathematical model's structure is as follows,

The piston's isentropic compressing and expanding in the cylinder are simulated by the isentropic sub-model. This model calculates the thermodynamic properties of cylinder in each step, which is theta equal 1 of crank angle degree, in piston movement according to the isentropic relation and by employing the engine geometry relations.

3.1 Injection sub-model

It replicates the processes of fuel injection and association, such as combustion, heat release, and heat transfer. This model, which is regarded as the most significant model, includes a number of sub-models for the injector, fuel characteristics, heat releasing and transmission, and ignition delay.

3.2 Equilibrium Sub-Model

In this model, the mole fraction of the combustion products and their specifications are calculated. The general algorithm of this model is shown in figure 4. The equilibrium model comprises several sub-models, such as minimum step *fmin* sub-model, guess sub-model, newton sub-model, and line search sub-model.

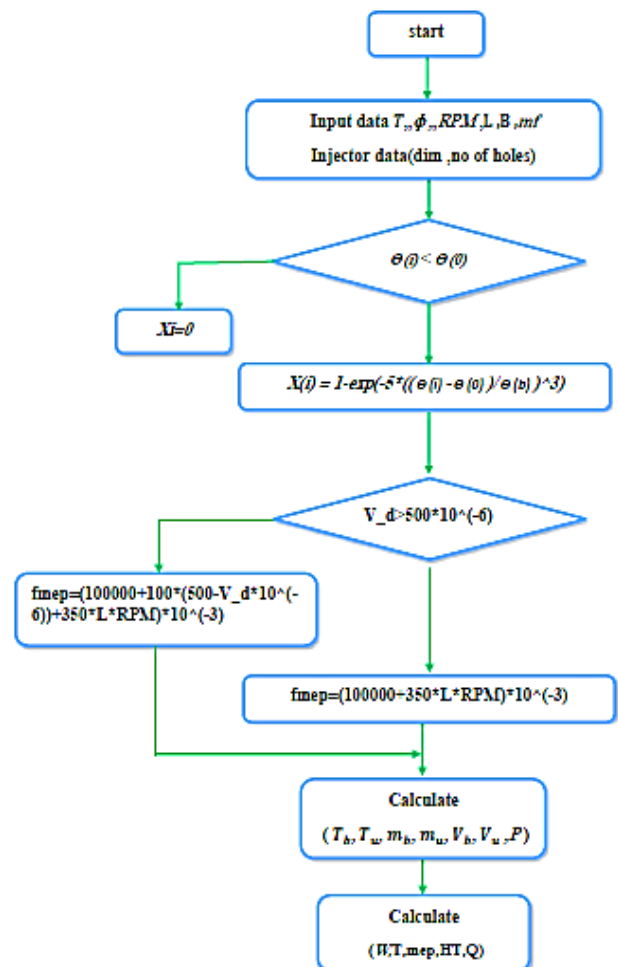


Figure 3. Algorithm of Main Model.

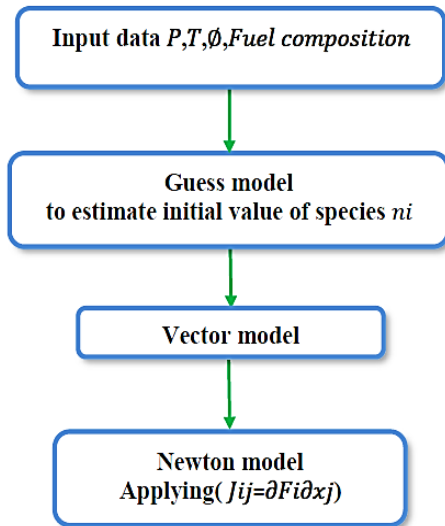


Figure.4 Algorithm of Equilibrium Model.

4. Results and Discussion

4.1 Validation of the Matlab Model

Figure 5 shows the comparison of in-cylinder pressures obtained from the present Matlab Model and CFD simulation results of [Reddy A. et al., 9] for holes number 8 and compression ratio 9.3. From Figure 3, It can be observed that, there is a reasonably good agreement among the results. Therefore, the models used in this Matlab Model are working well and therefore they can be used with confidence for further study.

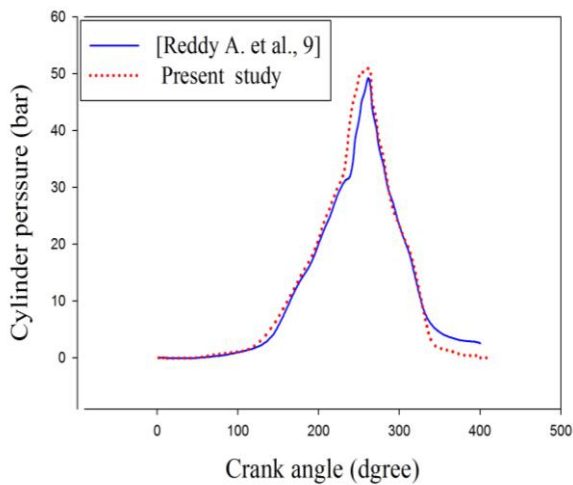


Figure 5. Comparison of in-cylinder pressures.

4.2 Variation of Orifice Diameter

The mathematical model for a GDI engine at (3000 rpm and 40 MPa injection pressure and compression ratio 9.5 spark timing 145°) is shown in Figure 6 the influence of nozzle hole diameter on the variation of cylinder pressure with crank angle. Increasing the hole diameter led to increase the cylinder pressure, as it can be observed. The maximum value of in-cylinder pressure is at the nozzle hole with a diameter of 0.650 mm due to the increase in injection area, which led to an increasing within fuel mass flow rate and quantity of heat release.

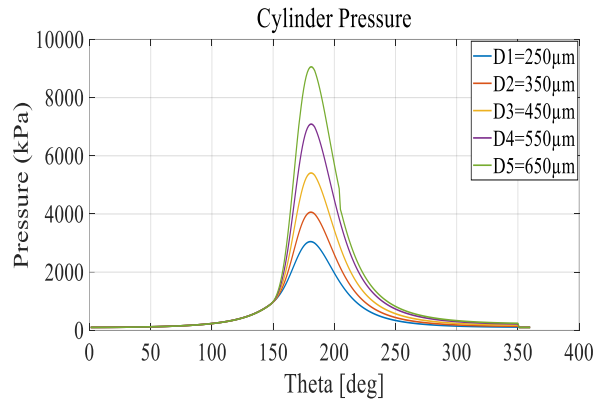


Figure 6. Cylinder pressure for different hole diameters.

The impact of nozzle hole diameter on the changing burned and unburned gas temperatures with crank angle is shown in figure 7. Although the impact of hole width on unburned gas temperature is minimal, it has a significant influence on burned temperature. By increased the diameter of the nozzle as it can be noticed, the burned gas temperature also increased. The 0.650 mm diameter nozzle hole produced a greater in-cylinder gas temperature due to the increased injection area, increased fuel mass flow rate, and increased heat release.

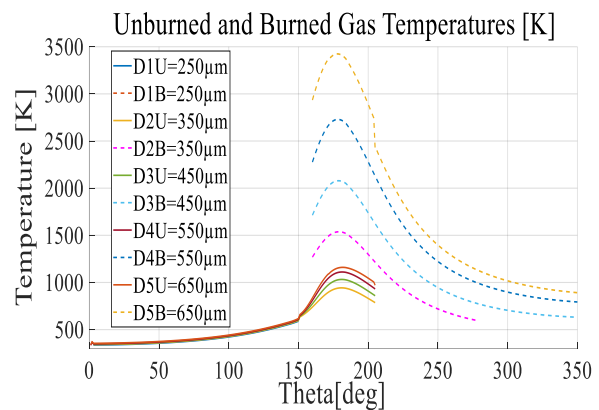


Figure 7. burned and unburned gas temperature for different hole diameters.

Figures 8 and 9 depict the impact of hole diameter on engine power and heat transfer as a function of crank angle. By increment the diameter of the nozzle as it can be observed, the engine power and heat transfer also increase because of the increased gas pressure brought on by an increase in the injection area, which leads to increase the fuel mass flow rate and heat release.

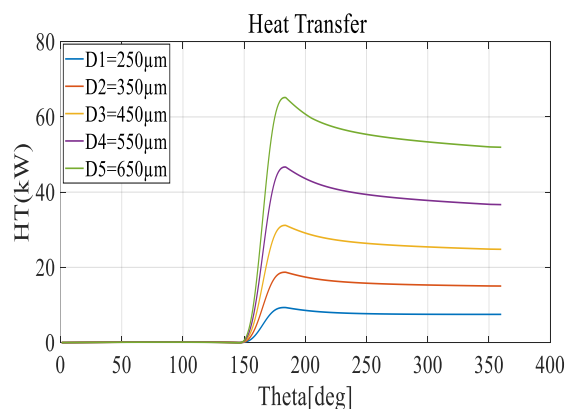


Figure.8 Engine power for different hole diameters.

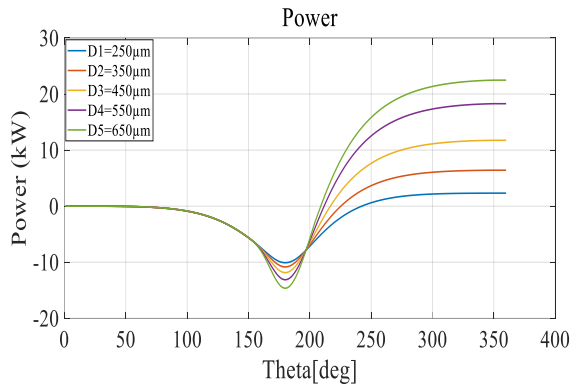


Figure 9. Heat transfer for different hole diameters.

Figure 10 shows CO emissions, as a function of crank angle at various fuel injector nozzle-hole sizes. These emissions of CO rise as the diameter of the nozzle hole increases. This is due to the fact that local rich zones begin to form as the injection area and fuel mass flow rate increase.

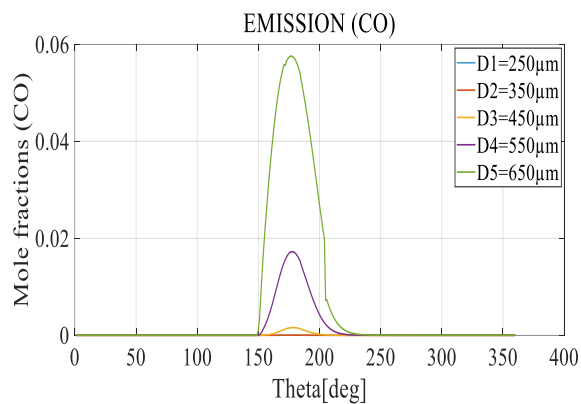


Figure.10. Effect of hole diameter on emissions of CO.

Figure 11 depicts NO emissions as a function of crank at various fuel injector nozzle-hole sizes. It is observed that the NO emissions rise as the diameter of the nozzle hole grows. This is due to the fact that bigger nozzle-hole sizes led to rich mixture and then higher in-cylinder temperatures.

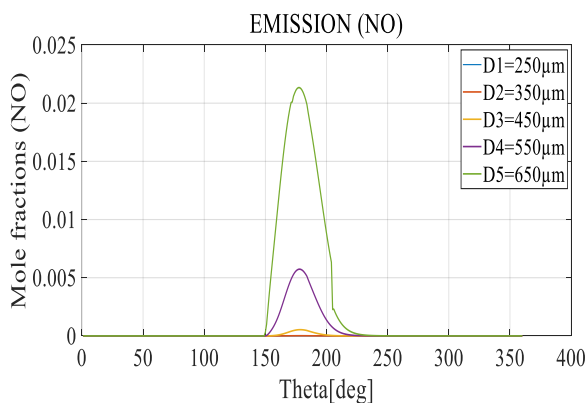


Figure.11. Effect of hole diameter on emissions of NO.

Figures 12 and 13 demonstrate the greatest power per cycle and optimal nozzle diameter vs. engine compression ratio as the number of holes is varied. It was shown that the greatest engine power per cycle was attained when the nozzle diameter (0.630 mm) and compression ratio (11) with (6) holes number were used.

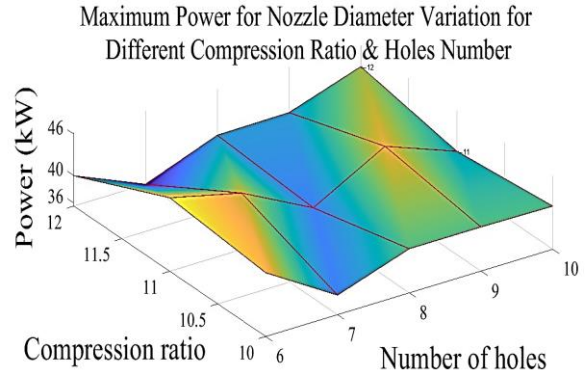


Figure 12. Maximum power for nozzle diameter variation for different compression ratio & holes number.

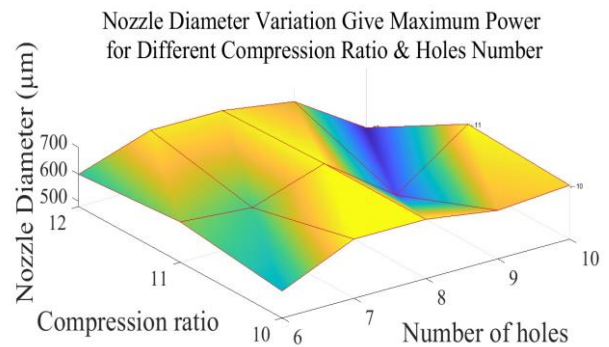


Figure 13. Nozzle diameter variation give maximum power for different compression ratio & holes number.

4.3 Variation of Orifice Diameter with Rotation Engine Speed.

Data in the table 1 show the influence of the variation of nozzle hole diameter on the maximum values for temperature, pressure, power, heat transfer and emissions. The mathematical model for a GDI engine at (Rotation Engine speed of 1000, 2000, 3000, 4000, 5000 rpm, 35 MPa injection pressure, compression ratio of 11.5, and spark timing of 140°). The highest of maximum values of temperature, pressure, and emissions were at a 1000 rpm and diameter of 0.650 mm. The highest values for maximum power at 4000 rpm and nozzle diameter of 0.650 mm, while the highest maximum values for heat transfer are at 5000 rpm and diameter of 0.65mm.

4.4 Variation of the Number of Nozzle Holes

Figure 14 shows the effect of injector holes' number on the variation in-cylinder pressure with crank angle as determined by the mathematical model for the GDI engine at (3000 rpm, 40 MPa injection pressure, compression ratio 9.5, and spark timing 145°) by using the MATLAB software. Because of the regular distribution of equivalence ratios throughout the spark plug area, it is observed that when the fuel injector holes' number rises, the in-cylinder pressure also rises. This is due to the creation of excellent fuel droplets with an increasing within the fuel injector holes number.

Figure 15 depicts the influence of hole number on burned and unburned gas temperatures as a function of crank angle. The influence of hole number on unburned temperature is minimal, whereas the hole number influence upon burned gas temperature is significant. By increased the injector holes number as it can be noticed, the burned gas temperature also increased. and highest gas temperature among the others at (12) nozzle holes number.

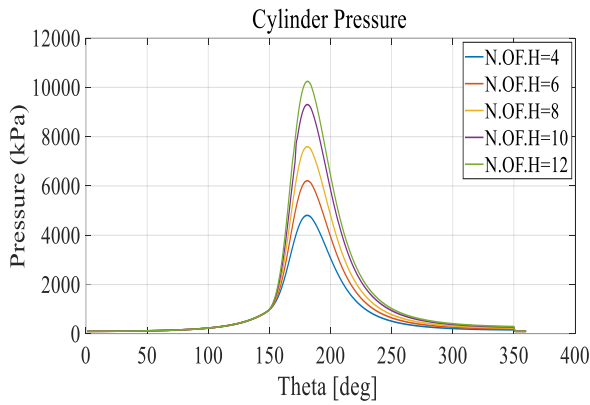


Figure 14. Cylinder pressure for different holes number.

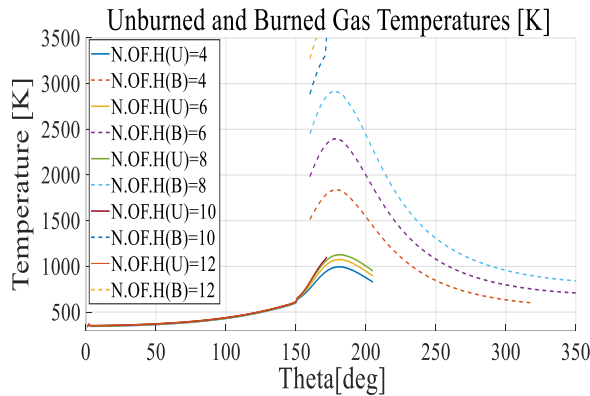


Figure 15. Burned and unburned gas temperature for different holes number.

Table 1. Variation of Maximum Values of Operating Engine Parameters with Nozzle Diameter.

Temperature(K)					
	Speed (rpm)				
D(mm)	1000	2000	3000	4000	5000
0.25	1767	1789	1536	1356	1124
0.35	1916	1921	1754	1527	1343
0.45	2467	2671	2224	1734	1542
0.55	2976	2987	2685	2223	1936
0.65	3187	3165	3013	2775	2430

Pressure (kPa)					
	Speed (rpm)				
D(mm)	1000	2000	3000	4000	5000
0.25	5284	4471	3852	3541	3354
0.35	7331	6300	5088	4474	4103
0.45	8974	7724	6729	5715	5102
0.55	9750	8654	7773	6563	6028
0.65	10674	9476	8537	7663	6940

Power (kW)					
	Speed (rpm)				
D(mm)	1000	2000	3000	4000	5000
0.25	2.261	1.807	1.183	0.5134	0.3456
0.35	4.918	5.051	4.639	4.095	3.492
0.45	7.667	9.19	9.118	8.767	8.296
0.55	11.48	13.34	14.56	14.48	14.19
0.65	11.35	20.92	21.38	24.84	21.16

Heat transfer (kW)					
	Speed (rpm)				
D(mm)	1000	2000	3000	4000	5000
0.25	8.643	8.991	9.352	9.793	10.04
0.35	17	17.35	17.42	17.8	18.39
0.45	27.79	28.8	29.05	30.16	30.97
0.55	37.54	42.85	43.53	44.79	45.93
0.65	52.36	59.07	60.72	61.17	63.56

Mole fraction of CO (Xi)					
	Speed (rpm)				
D(mm)	1000	2000	3000	4000	5000
0.25	6.1 e-04	2.3 e-07	1.47e-06	1.8 e-6	7.53e-07
0.35	0.02874	6.24 e-04	3.47e-05	6.33 e-06	8.53e-06
0.45	0.07289	0.01387	0.00132	1.83 e-07	3.63e-05
0.55	0.08544	0.053	0.01437	0.002918	0.00068
0.65	0.1582	0.07495	0.05509	0.03227	0.00592

Mole fraction of NO(Xi)					
	Speed (rpm)				
D(mm)	1000	2000	3000	4000	5000
0.25	0.00021	3.61 e-06	7.74e-06	4.79e-07	4.49e-07
0.35	0.00989	0.000222	1.37e-05	3.88e-06	3.88e-06
0.45	0.02439	0.004718	0.00046	6.79E-05	1.44e-05
0.55	0.03021	0.01895	0.00489	0.001002	0.00024
0.65	0.03976	0.0258	0.02021	0.01134	0.00201

Figures 16 and 17 demonstrate impact of nozzle hole number on engine power and heat transfer as a function of crank angle. we can notice as the number of holes rise, so does engine power and heat transfer. This is due to increase in-cylinder pressures, as well as better atomization and a faster heat transfer rate.

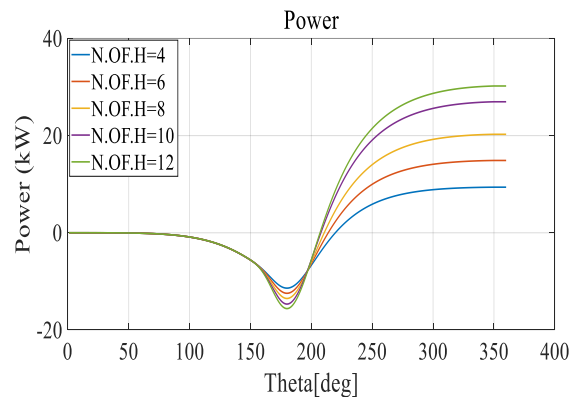


Figure.16. Engine power for different holes numbers.

The CO emissions are shown in Figure 18 at different fuel injector nozzle-hole numeral as a function of the crank angle. We can see that as the of nozzle-holes increase, so do the amount of CO emissions. This is because increased injection area and subsequent rise in fuel mass flow rate that result in local rich zones and dissociation of combustion products at high temperatures.

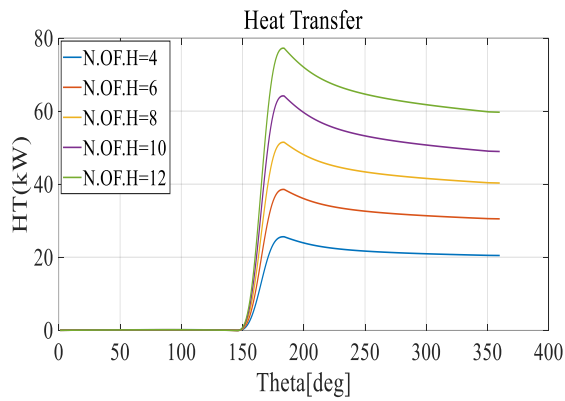


Figure.17. Heat transfer for different hole numbers.

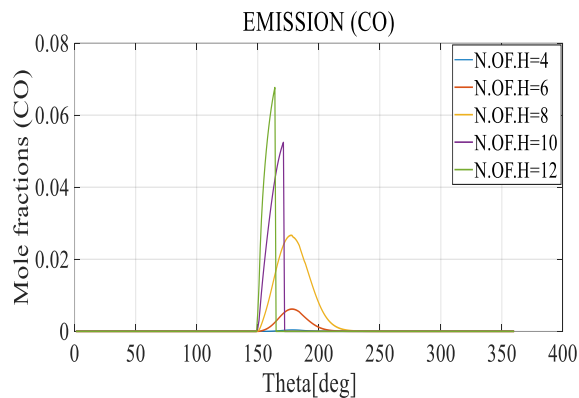


Figure18. Effect of holes number on emissions of CO.

Figure 19 explain NO emissions as a function of crank at various fuel injector nozzle-hole numeral. We can observe that NO emissions increase with increase in nozzle holes number. This is because the generation of NO is known to be significantly influenced by the thermal NO mechanism, which is extremely dependent on the temperature and the environment inside the cylinder. Higher numbers of nozzle holes result rich mixture zone and then higher in-cylinder temperature.

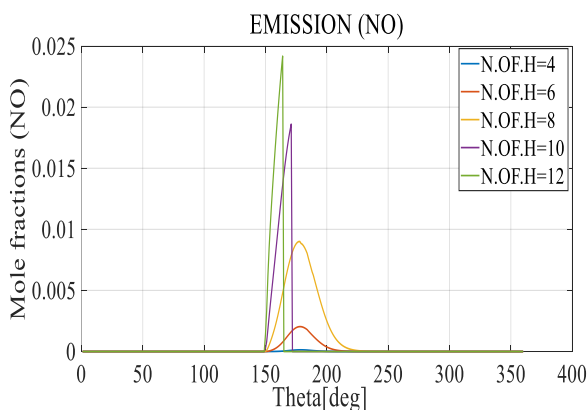


Figure.19. Effect of holes number on emissions of NO.

Figures (20) and (21) show the maximum power per cycle and the ideal number of nozzle holes in relation to engine compression ratio and nozzle diameter change. Figure 18 shows that the highest power per cycle generated at nozzle diameter (0.450 mm), the number of holes is (14) and the compression ratio is (12).

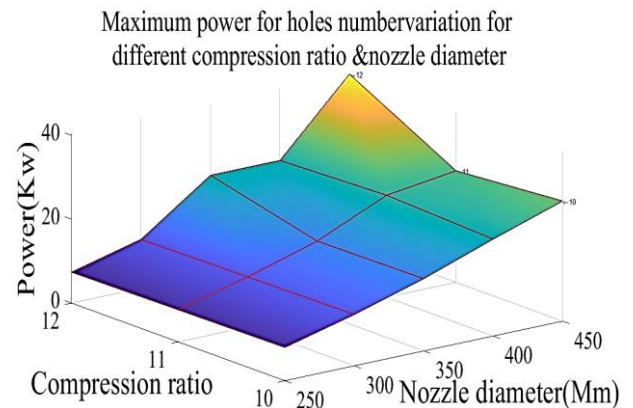


Figure 20. Maximum power for holes number variation for different compression ratio & nozzle diameter.

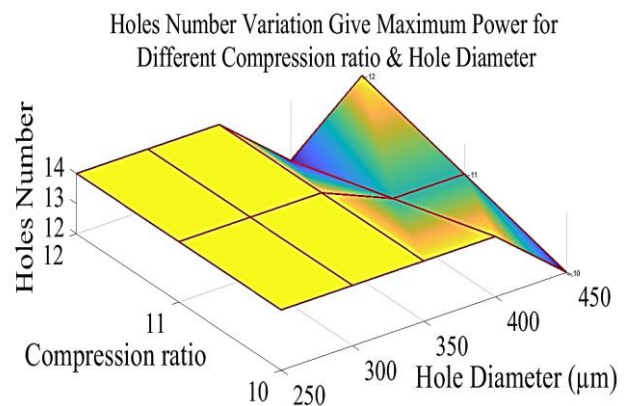


Figure 21. Holes number variation give maximum power for different compression ratio & Nozzle diameter.

4.5 Variation of the Number of Nozzle Holes with Rotation Engine Speed.

Data in the table 2 show the influence of the variation of nozzle diameter number on the maximum values for temperature, pressure, power, heat transfer and emissions. for the mathematical model for a GDI engine at (Rotation Engine speed of 1000, 2000, 3000, 4000, 5000 rpm ,35 MPa injection pressure, compression ratio of 11.5, and spark timing of 140°). The highest of maximum values of temperature, pressure, and emissions were at a rotation engine speed of 1000, and (12) holes. The highest values for maximum power at 4000 rpm and (12) holes, while the highest maximum values for heat transfer are at 5000 rpm and (12) holes.

5. Conclusion

A 4-stroke cycle of a gasoline direct injection engine was mathematically modeled. The mathematical model may be used to analyze the emissions of pollutants from a gasoline direct injection engine as well as its performance. Modeling the combustion with various nozzle hole diameters and numbers was done using the MATLAB algorithm. The following are the key findings from the current investigation.

- Cylinder pressure and temperature were observed to rise as nozzle hole diameter increased, as did maximum peak pressure and burned temperature when nozzle hole diameter was 0.650mm.
- Engine power and heat transfer increased as nozzle hole diameter increased, with a maximum value when nozzle hole diameter was 0.650mm.
- The lowest value of nozzle hole diameter, 0.250mm, was found to have the lowest CO and NO emissions.

Table 2. Variation of Maximum Values Operating Engine Parameters *s* with Nozzle Holes Number.

Temperature(K)					
	Speed (rpm)				
holes	1000	2000	3000	4000	5000
4	2203	2040	1825	1559	1367
6	2653	2506	2361	1970	1728
8	3087	2984	2883	2372	2057
10	3156	3080	2929	2759	2381
12	3347	3230	3189	3019	2693
Pressure (kPa)					
	Speed (rpm)				
holes	1000	2000	3000	4000	5000
4	7954	7643	5997	5161	4656
6	8198	7892	7704	6453	5695
8	8973	8763	8460	7742	6734
10	9983	9958	9763	9014	7770
12	11019	10943	9987	9597	8805
Power (kW)					
	Speed (rpm)				
Speed rpm/holes	1000	2000	3000	4000	5000
4	7.736	6.364	6.132	5.691	5.16
6	9.133	7.364	11.73	12.5	13.12
8	11.57	14.95	16.53	16.23	17
10	11.3	26.92	20.3	20.93	16
12	10.7	21.58	24.63	45.01	25.62
Heat transfer (kW)					
	Speed (rpm)				
Speed rpm/holes	1000	2000	3000	4000	5000
4	22.97	23.69	24.86	25.91	27.92
6	33.82	35.59	36.95	38.13	38.22
8	44.99	47.35	49.99	50.31	51.49
10	51.42	58.12	59.54	61.47	63.73
12	58.53	70.01	72	74.72	75.95
Mole fraction of CO (Xi)					
	Speed (rpm)				
Speed rpm/holes	1000	2000	3000	4000	5000
4	0.06334	0.004746	0.000341	4.32e-05	8.53e-06
6	0.07814	0.03322	0.005082	0.000828	0.000175
8	0.08852	0.06363	0.02332	0.005306	0.001334
10	0.09082	0.07345	0.09452	0.01744	0.005479
12	0.1049	0.07875	0.06435	0.03249	0.01471
Mole fraction of NO (Xi)					
	Speed (rpm)				
Speed rpm/holes	1000	2000	3000	4000	5000
4	0.02345	0.001616	0.000124	1.69e-05	8.74e-06
6	0.02549	0.01172	0.001729	0.000292	6.5e-05
8	0.02768	0.02338	0.008061	0.001807	0.000465
10	0.03028	0.02504	0.009561	0.005969	0.001865
12	0.3568	0.0258	0.01872	0.01114	0.005018

- When using a nozzle diameter of 0.630 mm and a compression ratio of 11, with nozzle holes ranging from 6 to 12, the maximum power per cycle for the engine was obtained.
- The cylinder pressure and temperature were observed to rise as the number of nozzle holes increased, with 12 nozzle holes producing the highest peak pressure and burned temperature.
- By increasing the number of nozzle holes, up to a maximum of 12, engine power and heat transfer increased.
- With lowest nozzle holes number (four nozzle holes) it was found that CO and NO emissions were the lowest.
- Maximum power per cycle (0.450 mm) and the ideal number of nozzle holes in relation to engine compression ratio with respect to nozzle diameter variation were found to be (14) for nozzle holes and (12) for compression ratio, respectively.
- The highest of maximum values of temperature, pressure, and emissions were at a speed of 1000, and nozzle diameter of 0.650 mm, and (12) holes. The highest values for maximum power at 4000 rpm and nozzle diameter of 0.650 mm and (12) holes, while the highest maximum values for heat transfer are at 5000 rpm, a diameter of 0.65mm and (12) holes.

From the conclusions above, injector parameters (nozzle diameter & holes number) it plays an important role in engine performance and emissions. Knowing the optimal injector parameters and its effect with other parameters on engine performance is necessary. Accordingly, fuel injector must be designed for best engine operation and emissions as low as possible. Therefore, in the future, it is necessary to know the effect of the rest of the parameters, such as fuel injection pressure, engine load, and engine geometry etc., with injector parameters on the performance and emissions of the GDI engine.

Acknowledgements:

The authors are grateful for the assistance they received from the staff at the Mechanical Department of the University of Technology-Iraq.

Nomenclature

a_s	air--fuel ratio	Unit less
A_{inj}	Orifice Area	m ²
A_u	unburned area	m ²
A_b	Burnt area	m ²
C_v	specific heat	kJ/kg.k
C_d	Discharge Coefficient	Unit less
Ca	Area Contraction Coefficient	Unit less
(CR)	compression ratio	Unit less
DQ_1	Convective losses	kW
DQ_2	change in heat transfer	KW
dur_{CA}	Injection Duration	degree
FMEP	Friction mean effective pressure	Pa
hr	radiation heat coefficient	W/m ² .K
H	Heat transfer coefficient	W/m ² .K
L	engine's stroke	m

LH V	lower heating values of the provided fuel	kJ/kg
m	mass	Kg
\dot{m}_f	Fuel flow rate	kmol/s
\dot{m}_{CA}	Fuel flow rate	kmol/deg
MW_f	Molecular weight	kmol/kg
N_s	Rotation Engine Velocity	rpm
Nu_i	Nusselt number	Unit less
P	Pressure	kPs
P_{inj}	Injection Pressure	kPa
P_{injmax}	Maximum Injection Pressure	kPa
P_{injmin}	Minimum Injection Pressure	kPa
Q	overall energy input into the system	kJ
U_{fuel}	Fuel velocity	m/s
ΔU	changing within internal energy	kJ
R	Gas constant	kJ/kg.k
Re	Reynolds number	Unit less
T	Temperature	K
T_w	Wall temperature	K
V	Volume	m ³
V_d	Displaced Volume of Engine	m ³
W	work output from the system	kJ
\dot{W}_b	Brake power	kW
W_i	Work	kJ
\dot{W}_i	indicate power	kW
Xb	mass fraction	Unit less

Greek Symbols

η	combusting efficiency	Unit less
η_m	Mechanic efficiency	Unit less
τ	torque	N.m
γ	Gas index	Unit less
θ	crank angle.	degree
$\Theta(i)$	immediate crank angle	degree
$\Theta(o)$	spark angle at the beginning of combustion	degree
$\Theta(b)$	the burn length	degree
ϕ	equivalence ratio	
ρ_{fuel}	Fuel Density	kg/m ³

Subscripts

B	burn
U	unburned

Abbreviations

BTDC	Before top dead center
CO	Carbon monoxide
DI	Direct-injection (DI)
Holes	Number of holes in injector
PFI	Port fuel injection
INHNS	Injector nozzle hole numbers
IPs	Fuel injection pressures
GDI	Gasoline direct injecting
NO	Nitrogen monoxide

References:

- [1] F. Zhao, M. C. Lai, and D. L. Harrington, "Automotive spark-ignited direct-injection gasoline engines," *Prog. Energy Combust. Sci.*, vol. 25, no. 5, pp. 437–562, 1999, doi: 10.1016/S0360-1285(99)00004-0.
- [2] J. Gao, D.-M Jiang, Z.-H Huang, X.-B Wang, "Numerical Study on Spray and Mixture Stratified Combustion in a Direct Injection Gasoline Engine," *Chinese Society for Internal Combustion Engines.*, vol 23 (4), pp. 297-306, 2005
- [3] M. A. Mashkour, "Investigation of Spark Ignition Engine Mathematical Model Using MATLAB (GUI)," *Advances in Natural and Applied Sciences.* vol 11 (11) ,pp 36-50, 2017, [Online]. Available: <http://www.aensiweb.com/ANAS>.
- [4] R. Sharma, "Experimental study of the Effect of Fuel Injector nozzle holes on Direct Injection Diesel Engine," *IOSR J. Mech. Civ. Eng.*, vol. 7, no. 4, pp. 67–74, 2013, doi: 10.9790/1684-0746774.
- [5] Y. J. C. and C. H. J. B. H. LEE, J. H. SONG, "Effect of The Number of Fuel Injector Holes on Characteristics of Combustion and Emissions in A Diesel Engine," *Int. J. Automot. Technol.*, vol. 11, no. 6, pp. 783–791, 2010, doi: 10.1007/s12239.
- [6] M. Vijay Kumar, A. Veeresh babu, P. Ravi Kumar, and T. Manoj Kumar Dundi, "Influence of different nozzle hole orifice diameter on performance, combustion and emissions in a diesel engine," *Aust. J. Mech. Eng.*, vol. 18, no. 2, pp. 179–184, 2020, doi: 10.1080/14484846.2018.1453975.
- [7] C. Jiang, M. C. Parker, J. Helie, A. Spencer, C. P. Garner, and G. Wigley, "Impact of gasoline direct injection fuel injector hole geometry on spray characteristics under flash boiling and ambient conditions," *Fuel*, vol. 241, no., pp. 71–82, 2019, doi: 10.1016/j.fuel.2018.11.143.
- [8] M. B. Ahmed and M. W. Mekonen, "Effects of Injector Nozzle Number of Holes and Fuel Injection Pressures on the Diesel Engine Characteristics Operated with Waste Cooking Oil Biodiesel Blends," *Fuels*, vol. 3, no. 2, pp. 275–294, 2022, doi: 10.3390/fuels3020017.
- [9] A. A. Reddy and J. M. Mallikarjuna, "Parametric Study on a Gasoline Direct Injection Engine - A CFD Analysis," *SAE Tech.*, Paper no 2017-26-0039, 2017, doi: 10.4271/2017-26-0039.

- [10] P. D. Jadhav and J. M. Mallikarjuna, "Effect of fuel injector hole diameter and injection timing on the mixture formation in a GDI engine - A CFD study," *Int. J. Comput. Methods Exp. Meas.*, vol. 6, no. 4, pp. 737–748, 2018, doi: 10.2495/CMEM-V6-N4-737-748.
- [11] J. B. Heywood, *Internal Combustion Engine Fundamentals*. N. York: McGraw-Hill, pp. 389–716, 1988
- [12] Y. G. Guezennec and W. Hamama, "Two-zone heat release analysis of combustion data and calibration of heat transfer correlation in an I. C. engine," *SAE Tech. Paper.*, no. 724, 1999, doi: 10.4271/1999-01-0218.
- [13] G. P. Blair, *The Basic Design of Two-Stroke Engines*, USA. Society of Automotive Engineers, Inc 400 commonwealth engine, pp.205-297, 1990 doi: 10.4271/r-104.
- [14] W. J. D. Annand, "Heat Transfer in The Cylinders of Reciprocating Internal Combustion Engines," *Thermodynamics and Fluid Mechanics Group*, vol. 177, no. 36, pp. 973–996, 1963, doi: 10.1243/PIME.
- [15] D. L. Siebers, "Scaling liquid-phase fuel penetration in diesel sprays based on mixing-limited vaporization," *SAE Tech. Paper*, no. 724, 1999, doi: 10.4271/1999-01-0528.
- [16] C. R. F. A. T. Kirkpatrick, *Internal Combustion Engines Applied Thermosciences*, 3rd ed., John Wiley & Sons, Ltd, pp.84-120, 2016.
- [17] C. Olikara and G. L. Borman, "A computer program for calculating properties of equilibrium combustion products with some applications to I.C. engines," *SAE Tech. Paper* no 750468., 1975, doi: 10.4271/750468.
- [18] G. L. B. R. B. Krieger, *The computation of apparent heat release for internal combustion engines*. New York: ASME, pp66-WA/DGP-4 1966.

Research Article

Performance Evaluation of R1224yd as Alternative to R123 and R245fa for Vapor Compression Heat Pump System

¹*N. Aisyah , ²H. M. Ariyadi 

¹ Department of Mechanical Engineering, Vocational School, Universitas Gadjah Mada, Jl. Yacaranda, Sekip Unit IV, Yogyakarta 55281, Indonesia

² Department of Mechanical and Industrial Engineering, Faculty of Engineering, Universitas Gadjah Mada, Jl. Grafika No. 2 Yogyakarta 55281, Indonesia
E-mail: ¹*nyayuaisyah@ugm.ac.id

Received 6 June 2023, Revised 25 August 2023, Accepted 8 October 2023

Abstract

The search for environmentally friendly refrigerants for vapor compression systems has been a significant focus recently due to environmental concerns such as ozone depletion and global warming. In this study, the potential of R1224yd as an alternative refrigerant is investigated. A thermodynamic analysis of a 4-kW air conditioning system is conducted to assess the performance of R1224yd. The system is analyzed from a thermodynamic perspective, and key performance indicators such as the Coefficient of Performance and exergy efficiency. The results are then compared to R245fa and R123. Furthermore, a parametric study is performed to examine the impact of key parameters, such as evaporating and condensing temperatures, on the system's performance. This analysis provides insights into the sensitivity of the system's performance to variations in these parameters. The results indicate that R1224yd is a promising candidate as an environmentally friendly alternative refrigerant compared to R123 and R245fa. Because R1224yd has the lowest environmental impact. It has about 700 kg CO₂ indirect emission, but about zero kgCO₂ for direct emission. While, based on the thermodynamic results, R1224yd offers better performance compared to R245fa which has 1-3% higher in performance value and exergy efficiency, and has comparable performance to R123. This suggests that R1224yd can be a viable option for the systems, providing improved energy efficiency and lower environmental impact.

Keywords: *Warming impact; exergy efficiency; performance; refrigerant; thermodynamic analysis.*

1. Introduction

Recently, one of the hot topics in High Ventilating Air Conditioning and Refrigeration (HVACR) system are the search for alternative working fluid and refrigerant [1]–[9]. Chloro Fluoro Carbons (CFCs) as the first refrigerant for HVAC system banned in 1987 in Montreal Protocol and are being replaced by Hydro Fluoro Carbon (HFC) and Hydro Chloro Fluoro Carbon (HCFC). In 1996, the phase out of CFC refrigerant had been completed. HFC and HCFC were suggested as the alternative of CFC because it has low Ozone Depletion Potential (ODP). However, in 1990, it was found that suggested refrigerant which have low ODP, contribute to global warming phenomenon. So, in 1997, Kyoto Protocol was issued, the objective is to mitigate global warming by reducing greenhouse gas emissions, which entails advocating for the adoption of refrigerants with low Global Warming Potential (GWP) [10].

The GWP becomes the parameter in identifying priority actions to reduce Green House Gas (GHG) emissions and the impact of climate change. GWP is often used in international environmental regulations and agreements, such as in the Kyoto Protocol, to measure and compare the relative impact of various greenhouse gases on global warming. GWP is a concept used to measure the extent to which certain GHG can have an impact on global warming compared to carbon

dioxide (CO₂). This measurement is generally used in comparative contexts, where the GWP of a particular gas is measured in units relative to the CO₂ GWP which has a value of 1. For example, if a gas has a GWP of 25 over a 100 year time period, that means it has a global warming impact 25 times greater than the same amount of CO₂ over the same time period.

Many experts have introduced some alternative refrigerants to replace the conventional refrigerant [1], [3], [6], [11], [12]. For example, R1234ze series refrigerant have been widely pointed out as one of the potential alternative refrigerant due to their low flammability, low GWP value, and comparable performance to replace conventional refrigerant such as R134a [11], [13]–[15]. R32 and L41a are also suggested by some researchers as a candidate for R410A replacement because they are characterized by their low GWP value, same characteristics to R410A and having a good performance [10], [12], [16], [17]. Researchers also mention the return to natural refrigerants as alternative refrigerants have raised special interest recently. Nasruddin et al have been conducted research using working fluid mixture 86% R601 and 14% R744 for binary cycle system [2]. Yamaguchi et al also have been done research about using R744 for heat pump system [18]. Hydrocarbons as natural refrigerants are considered as harmless working

fluids, non-toxic, non-flammable and the important thing that they do not contribute to global warming issue [5], [19]–[22].

To assess the performance of alternative refrigerants and their potential as replacements for conventional ones, a thermodynamic analysis is needed. The study conducted by Park et al [21] in 2008 provides valuable insights into the thermodynamic analysis of a residential heat pump system using R433A as a replacement for R22. R433A is a refrigerant with zero ODP and a lower GWP of less than 5, making it an environmentally friendly alternative. The key finding of the study indicates that coefficient of performance of the system using R433A is 4.9% higher than using R22. The study concludes that R433A is a good substitution for conventional refrigerants with better performance [21]. J Alberto also reported the system's COP and exergy efficiency of cooling system that using alternative refrigerants, R744 [23]. Nawaz K et al, 2017 were having residential heat pump system performance evaluation to compare R600a and R290 refrigerant with R134a. The analysis revealed that both refrigerants could be the option with comparable performance [11]. Recently in 2023, Zhou Dong et al conducted a theoretical study about low GWP refrigerant. The research investigates the thermal efficiency of three refrigerants with low global warming potential, namely R1224yd(Z), R1223zd(E), and R1336mzz(Z), as potential replacements for R245fa. The findings indicated that both R1224yd(Z) and R1223zd(E) exhibited a slightly improved coefficient of performance (COP) compared to R245fa, with R1224yd(Z) showing a 2% increase, and R1223zd(E) showing a 1% increase [24]. While Jiang et al examine the performance of the environmentally friendly refrigerant R1233zd(E) when operating at a temperature lift of 50°C. The experiments were carried out under specific working conditions, including a heat source temperature range of 30–50°C and an output temperature range of 60–100°C. The system achieved a heating capacity of 381 kW and a coefficient of performance (COP) of 3.67 [25].

The purpose of this work is to evaluate the energy and exergy performance of low GWP refrigerant R1224yd theoretically and compare it with the relatively high GWP refrigerants: R245fa and R123. In this paper, parameter study is conducted to investigate the low GWP refrigerant performance, including the effect of different evaporation and condensation temperature. The Total Equivalent Warming Impact (TEWI) analysis also conducted in this paper to examine the best refrigerant among 3 discussed refrigerants. By conducting this study, the suitable refrigerant for vapor compression heat pump system in performance and environmental point of view can be known. It gives recommendations to scientists about the method to select the refrigerant for a system.

2. Working Fluids and System Modelling

In this paper, the working fluids evaluation and system modeling are discussed. Refrigerant evaluation was conducted by examining the fluid properties while the system modelling of heat pump was done by using MATLAB software through thermodynamic considerations.

2.1 Fluid Properties

The selection of a suitable working fluid for a heat pump system involves evaluating several criteria, including thermophysical properties, safety considerations (toxicity and flammability), and environmental factors [2], [26].

Thermo-physical properties such as critical temperature and pressure play a crucial role in this selection process, while environmental factors, especially Global Warming Potential (GWP) becomes an important consideration. Table 1 provides information on the refrigerants discussed in this study, while Figure 1 and 2 illustrates the Ph and Ts diagram for each refrigerant.

Table 1. Properties of discussed refrigerants.

Parameter	R123	R245fa*	R1224yd**
Critical Temp (°C)	183.8	154	155.5
Critical Pressure (MPa)	3.66	3.65	3.33
GWP	77	1030	<1
Safety Group	A2L	B1	A1
Glide Temperature (°C)	-0.2	2	0

Source: *[27], **[28]

R123 and R245fa have relatively good thermal efficiency and tend to be more chemically stable over a wide range of operating conditions and temperatures compared to some of the other alternatives. Wang et al have been conducted a simulation of heat pump system using R123, the results showed that the highest performance of the system can be achieved by using R123 [29].

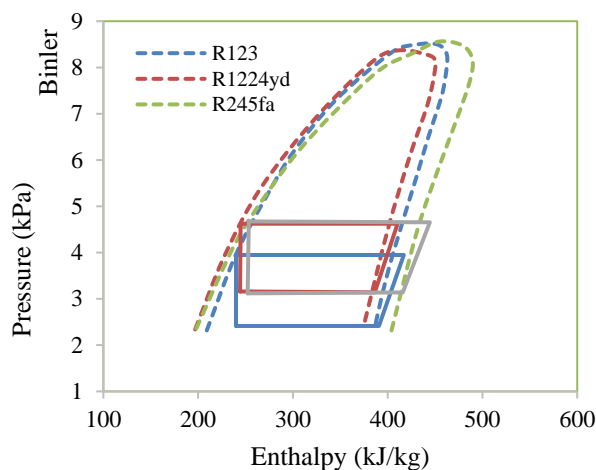


Figure 1. P-h diagram of heat pump cycle with discussed refrigerants.

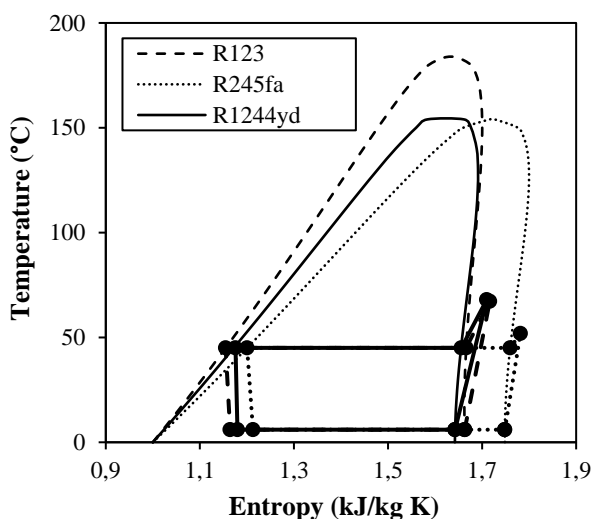


Figure 2. T-s diagram of heat pump cycle with discussed refrigerants.

However, the use of R-123 and R245fa refrigerants have been restricted due to their negative impact on the environment, this can be seen from their GWP value of 77 for R123 and 1030 for R245fa. Thus, many scientists carried out the research for the replacement of R245fa with another alternative refrigerant such as R1233zd(E) [30], [31] and R1336mzz(Z) [32].

Thus, R1224yd appeared to be the replacement of high GWP refrigerant [33]. As an alternative, R1224yd is designed to have minimal impact on the ozone layer, becoming one of alternative refrigerants with a reduced ozone-depleting potential or very small chlorine atom in its structure. Based on the investigation conducted by Akasaka et al. (2017), R1224yd exhibits a high critical temperature and possesses non-flammable and non-toxic properties, making it suitable for use in heat pump systems [34] or even industrial heat pump [33].

2.2 Cycle Description

The vapor compression heat pump cycle depicted in Figure 3 consists of several key components: an evaporator, a compressor, a condenser, and an expansion valve. The cycle operates by supplying external energy to the compressor, which increases the refrigerant temperature and pressure. Subsequently, the high-temperature refrigerant moves into the condenser, where the heat is transferred to the surroundings, resulting in the refrigerant's condensation into a liquid state.

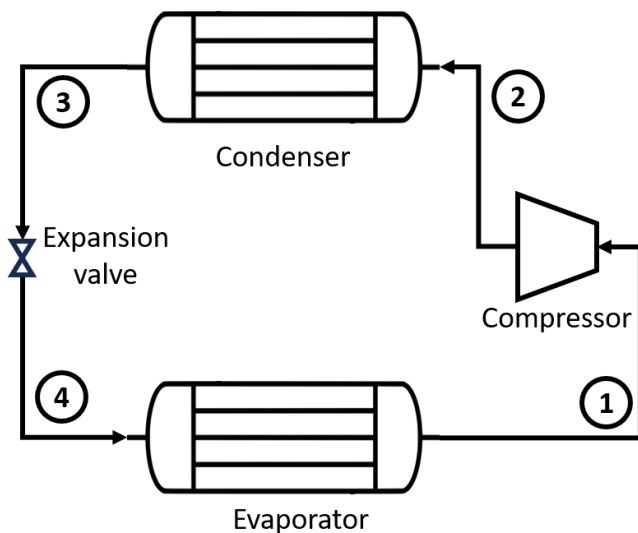


Figure 3. Heat pump system configuration.

The high-pressure refrigerant then passes through the expansion valve, where its pressure is significantly reduced, causing a drop in temperature. The refrigerant, which is at a low pressure and temperature, enters the evaporator and effectively absorbs heat from its surroundings, typically from the environment or a heat source. As a result, the refrigerant evaporates into a gas state, and the heat absorbed during this process is utilized for heating purposes in a heat pump system.

Table 2. Assumed values for the computation process.

Variables	Values
Compressor Isentropic Efficiency	70%
Superheat or subcooled Temperature	0
Heating capacity (kW)	4

The cycle is completed as the low-pressure refrigerant is drawn back into the compressor, and the process begins again. This continuous cycle allows the heat pump system to supply heat to a desired location by transferring heat from a low-temperature source to a higher-temperature destination, utilizing the refrigerant's phase changes and thermodynamic properties.

2.3 Thermodynamic Modelling

In this paper, a thermodynamic model is conducted to compare R1224yd with R245fa and R123. The modelling involves incorporating mass and energy balances, which are crucial for improving the system's efficiency. Some assumptions are made during the component modelling process, including:

1. The system operates under steady-state conditions
2. The impact of pressure and heat loss in the system's pipelines is disregarded.
3. Saturated refrigerant conditions are assumed at the exit of both the evaporator and the condenser, simplifying the analysis by considering the refrigerant in a fully vapor or fully liquid state.
4. The kinetic and potential energies of the refrigerant are not considered in the exergy analysis. This assumption allows the focus to be on the internal energy of the refrigerant and its potential to do useful work.

To conduct simulations and analyze the performance of the cycles, the researchers used MATLAB 2017b software which integrated with REFPROP version 9.0. MATLAB is a widely used programming and numerical computation software that provides various tools and functions for conducting simulations, data analysis, and mathematical modeling. Its integration with REFPROP, which is a program commonly used for thermophysical properties calculations of refrigerants, allowed the researchers to obtain accurate and reliable data for the refrigerants being studied. By utilizing MATLAB and REFPROP together, the researchers were able to perform simulations of the heat pump cycles, incorporating the properties and behavior of the refrigerants at different operating conditions. This combination of software provided the necessary tools and resources to analyze and compare the performance of the different refrigerants under consideration.

Energy and exergy balances play a crucial role in analyzing the performance of system components and evaluating overall system efficiency. Exergy, also known as available energy or useful work potential, represents the maximum work that can be obtained from a given energy source. It provides a measure of the quality of energy within a system, reflecting its potential to do useful work. To conduct a comprehensive analysis, the general equation of mass, energy, and exergy balances for each component in the system are considered. These balances are defined as follows [35]:

$$\sum \dot{m}_{in} = \sum \dot{m}_{out} \quad (1)$$

While \dot{m} is the mass flow rate and the subscripts in to describe input and out is output. The first law of thermodynamic is written as:

$$\dot{Q}_{in} + \dot{W}_{in} + \dot{m}h_{in} = \dot{Q}_{out} + \dot{W}_{out} + \dot{m}h_{out} \quad (2)$$

Where \dot{Q} is the heat transfer rate between control volume and its surroundings, \dot{W} is the work rate, and h is the specific enthalpy.

The Coefficient of Performance (COP) is a metric used to evaluate the energy efficiency of a heat pump system. It is defined as the ratio of the heat rejected in condenser to the total power consumption (the compressor total energy consumed). The calculation of COP can be expressed as:

$$\text{COP} = \frac{\dot{Q}_{\text{cond}}}{\dot{W}_{\text{comp}}} \quad (3)$$

With the second law of thermodynamics and exergy principles, the following general exergy rate balance can be written:

$$\dot{E}x_Q + \sum_i \dot{m}_i \dot{e}x_i = \sum_e \dot{m}_e \dot{e}x_e + \dot{E}x_W + \dot{E}x_D \quad (4)$$

The energy and exergy analysis are conducted based on thermodynamic analysis and mass balance equations which are listed in Eqs. (5-16).

For evaporator,

$$\dot{m}_1 = \dot{m}_4 \quad (5)$$

$$\dot{Q}_c = \dot{m}_{\text{ref}}(h_1 - h_4) \quad (6)$$

$$\dot{E}x_e = \dot{m}_{\text{ref}}(Ex_4 - Ex_1) + [1 - (T_a - T_{cl})] \dot{Q}_e \quad (7)$$

For compressor,

$$\dot{m}_1 = \dot{m}_2 \quad (8)$$

$$W_{\text{co}} = \dot{m}_{\text{ref}}(h_2 - h_1) \quad (9)$$

$$Ex_{\text{co}} = W_{\text{co}} - \dot{m}_{\text{ref}}(Ex_2 - Ex_1) \quad (10)$$

For condenser,

$$\dot{m}_2 = \dot{m}_3 \quad (11)$$

$$Q_c = \dot{m}_{\text{ref}}(h_2 - h_3) \quad (12)$$

$$Ex_c = \dot{m}_{\text{ref}}(Ex_2 - Ex_3) - [1 - (T_a - T_c)] Q_c \quad (13)$$

For expansion valve,

$$\dot{m}_3 = \dot{m}_4 \quad (14)$$

$$h_3 = h_4 \quad (15)$$

$$Ex_v = \dot{m}_{\text{ref}}(Ex_5 - Ex_6) \quad (16)$$

Exergy analysis is based on the first and second laws of thermodynamics. These equations, along with other thermodynamic relationships, are used to evaluate the energy and exergy transfers, efficiencies, and losses within a system. They provide valuable insights into the performance and optimization potential of the system. In vapor compression heat pump, the work of compressor considers as the input exergy while the exergy of product is the exergy of heat in

evaporator from the space to be cooled in which the equation is given by:

$$Ex_{\text{in}} = W_{\text{co}} \quad (17)$$

Then, the exergy destruction and exergy efficiency of the system can be calculated by using:

$$Ex_{D,\text{tot}} = Ex_e + Ex_{\text{co}} + Ex_c + Ex_v \quad (18)$$

$$Ex_{\text{eff}} = 1 - \frac{Ex_{D,\text{tot}}}{Ex_{\text{in}}} \quad (19)$$

2.4 Total Equivalent Warming Impact (TEWI) Analysis

In evaluating the selection of the refrigerant used, this research analyzed the environmental aspects, specifically focusing on the Total Equivalent Warming Impact (TEWI) as outlined in Mastrullo's work (2016). The TEWI values considered in this investigation are provided in Eq. (20).

$$\begin{aligned} \text{TEWI} &= \text{direct emissions} + \text{indirect emissions} \\ &= (\text{GWP} \times L \times N) + (Ea \beta n) \end{aligned} \quad (20)$$

where

TEWI : Total Equivalent Warming Impact (TEWI)

GWP: Global Warming Potential value

L : Leakage rate in kg (Estimated 3% of charge)

N : System lifetime (years)

Ea : Energy consumption (KWh/year)

β : CO₂ emission factor (0.483 kg CO₂/kWh)

n : System running time in one year.

3. Results and Discussions

In this paper, three refrigerants are discussed: R123, R245fa, and R1224yd. These refrigerants are evaluated based on their physical properties and environmental impact called TEWI analysis. Then, a system was modelled, and exergy analysis was carried out.

3.1 Evaluation of Refrigerants

The evaluation of refrigerants typically considers their physical properties and environmental effects. Physical properties such as critical temperature, and critical pressure are important factors in determining the suitability of a refrigerant for a particular application. These properties affect the refrigerant's performance in terms of heat transfer, energy efficiency, and system design.

In addition to physical properties, environmental factors are crucial considerations. These include ODP, GWP and Total Equivalent Warming Index (TEWI) of the refrigerant. ODP measures the potential for a substance to deplete the ozone layer, while GWP quantifies the impact of a substance on global warming compared to carbon dioxide. Low ODP and GWP values are desirable as they indicate a reduced environmental impact. But, in this study the ODP value was considered absolute, and it was known that the ODP value of the three discussed refrigerants was 0. So only GWP is included in the consideration.

The evaluation of these three refrigerants, R123, R245fa, and R1224yd, likely involves a comparison of their physical properties, and GWP values. This analysis helps determine their suitability for various applications, considering both performance and environmental considerations. The goal is to identify whether R1244yd is the best alternative refrigerant. Figure 4 illustrates the trend of thermodynamic

properties, including pressure and temperature of discussed refrigerants.

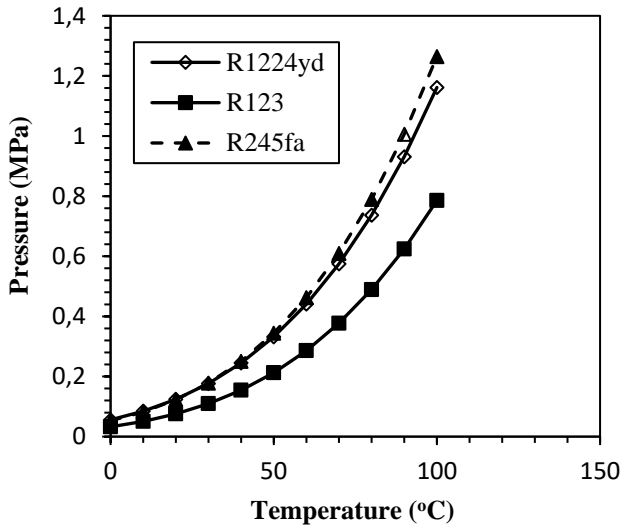


Figure 4. Temperature vs pressure of discussed refrigerants.

From figure 4, three refrigerants have nearly the same temperature and pressure range. Due to their similar properties, R1224yd can be a potential candidate compared to R123 and R245fa without any change in design pressure. Besides considering the thermodynamic properties of refrigerants, some parameters such as GWP and safety group of refrigerants were considered. Table 3 gives the result of refrigerant evaluation from 5 parameters including critical pressure, critical temperature, safety group, GWP, and glide temperature.

Table 3. Standardized data.

Parameters	R123	R245fa	R1224yd
Critical Temperature	1	1	1
Critical Pressure	0.956	0.959	1
GWP	0.77	0	1
Safety Group	0.75	0.5	1
Glide Temperature	1	0.2	1

In order to easier understand the data from Table 2, a spider plot is designed. Figure 5 shows spider plot of refrigerant evaluation procedure.

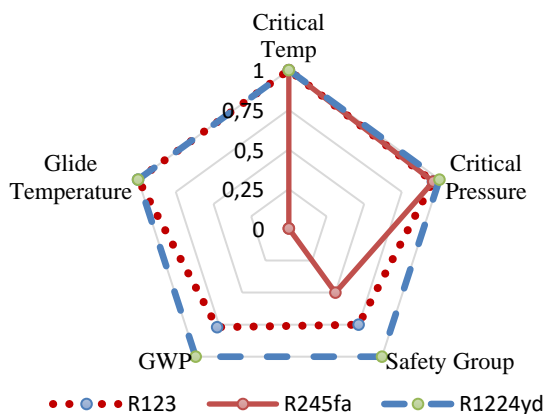


Figure 5. Evaluation of physical properties of three discussed refrigerants using spider plot.

From Figure 5, Based on the mentioned criteria and considerations, it can be concluded that R1224yd is the best refrigerant which is environmentally friendly. Its properties, such as low GWP and favorable safety characteristics, make it a promising option. To further evaluate the environmental impact, TEWI analysis was conducted as seen in Figure 6. TEWI takes into account both direct and indirect emissions of greenhouse gases throughout the life cycle of the refrigeration system. This analysis helps assess the overall environmental performance of different refrigerants, including R1224yd, R245fa, and R123.

By comparing the TEWI values for these refrigerants, it is possible to determine their respective contributions to global warming potential and environmental impact. This analysis provides valuable insights into the sustainability and efficiency of the heat pump system using each refrigerant.

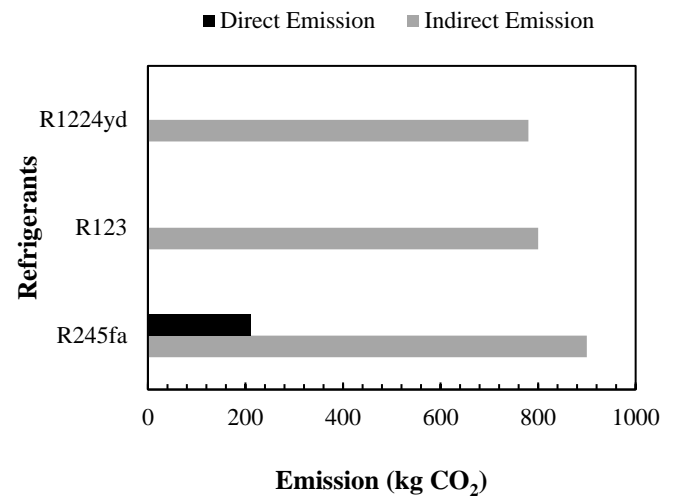


Figure 6. TEWI of refrigerant regarding to environmental effect.

From Figure 6, it can be seen that R245fa has the highest value both of indirect emission and direct emission of CO₂ compared to others. It has about 900 kgCO₂ indirect emission and about 200 kgCO₂ for direct emission. The suggested refrigerant, R1224yd has the lowest environment impact. It has about 700 kg CO₂ indirect emission, but about zero kg CO₂ for direct emission. Overall, considering the environmental criteria, thermodynamic properties, safety considerations, and TEWI analysis, R1224yd demonstrates favorable characteristics systems as a potential replacement refrigerant for heat pump systems.

3.2 Comparison Performance of R1224yd, R123, and R245fa

After considering the physical properties and environmental impact parameters, R1224yd emerges as the most promising candidate among the others. The next step is to evaluate the performance of the system using this refrigerant. This involves conducting a parameter study and system performance evaluation. In the parameter study, the evaporating temperature varies within a specific range, such as from 8°C to 16°C. Additionally, the condensing temperature varies at different set points, such as 40°C, 43°C, 46°C, and 49°C. These variations allow for an analysis of the system's performance under different operating conditions.

This evaluation enables engineers and researchers to make informed decisions regarding the selection of the

refrigerant and optimize the system's performance for specific applications. Under the same condition the result was compared and are shown in Fig 7-12. A computer program developed in MatLab and integrated with REFPROP was used to solve the equations. With the given input parameters including evaporator temperature, condenser temperature, ambient temperature, cooling capacity, the program calculates all thermodynamic properties of each point of the cycle, energy and exergy efficiencies and exergy destruction.

3.2.1 Effect of Evaporation and Condensation Temperature on the COP System

Refrigerant changes its phase from liquid to vapor in evaporator. If the evaporator temperature is increased constantly from 8 °C to 16 °C, the performance of the system, which is indicated by COP is increased as illustrated in Figure 7. This is due to the complete refrigerant evaporation occurring at higher temperature of evaporator. The value of COP ranges from 4.6 to 6.5, with the work of compressor ranges from 0.61 – 0.85 kW. There is the same tradeoff for R1224yd, R123 and R245fa.

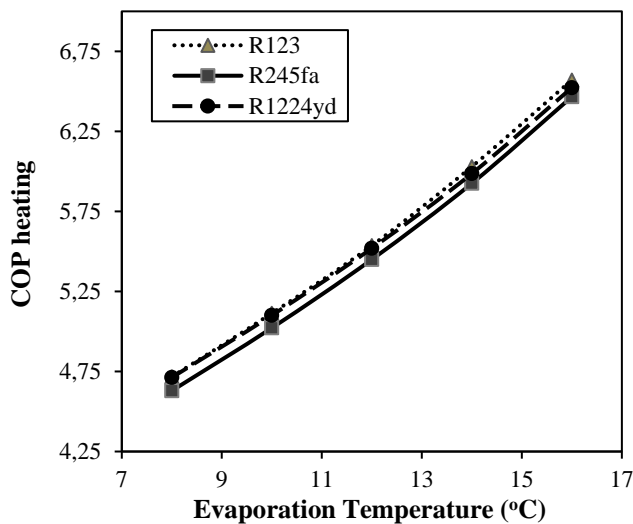


Figure 7. COP comparison for R245fa, R123 and R1224yd at various evaporating temperatures.

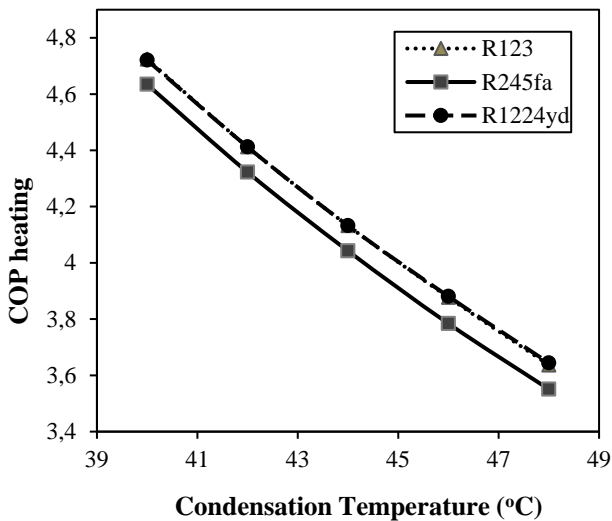


Figure 8. COP comparison for R245fa, R123 and R1224yd at various condensing temperatures.

While the increase in condensation temperature from 40 °C to 48 °C, decreases the COP from 4.7 to 3.6 as seen in Figure 8. This reveals that the heat pump could improve the system COP by increasing the evaporating temperature and decreasing condensing temperature. From Figure 8, performance of R1224yd has nearly the same trend as R123. COP of both refrigerants increase linearly with increasing evaporation temperature. As it is illustrated in the graph, R1224yd has better performance than R245fa with COP difference between both refrigerants is 1-3%. Finally, considering the performance evaluation and the environmental effect, R1224yd which has <1 of GWP value is a good replacement for R245fa.

3.2.2 Effect of Evaporation and Condensation Temperature on the Exergy

As is known, exergy is an important parameter to evaluate the maximum work that can be produced by the system. Exergy indicates the performance of the system. Figures 9 and 10 present the exergy efficiency of the system while Figures 11 and 12 show the exergy destruction of the system with various evaporation and condensation temperatures.

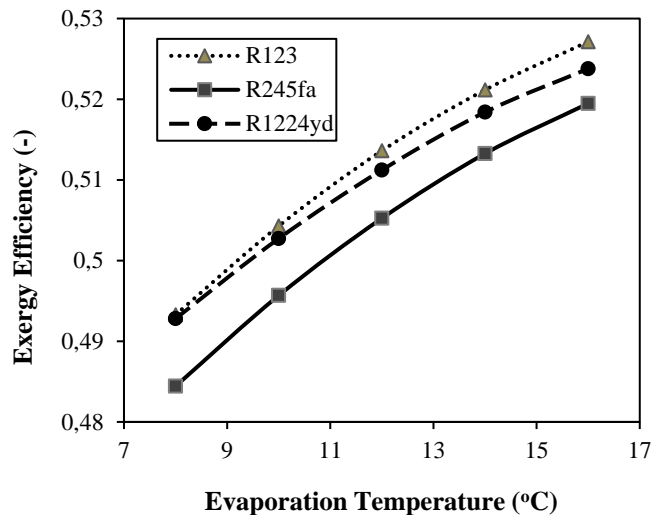


Figure 9. Exergy efficiency of the system at various evaporator temperatures.

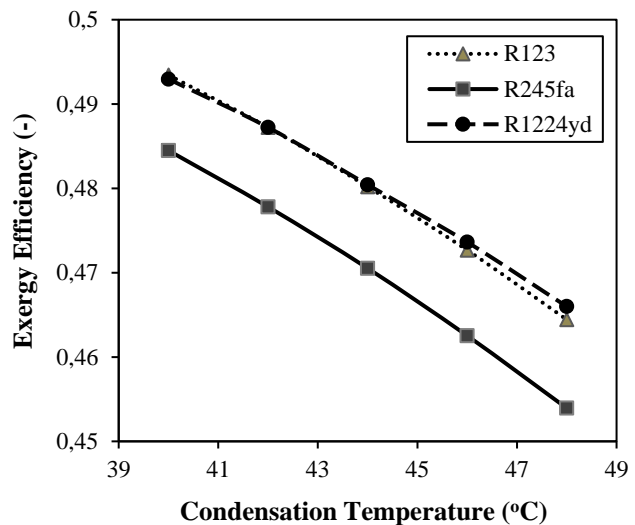


Figure 10. Exergy efficiency of the system at various condenser temperatures.

From Figure 9 and Figure 10, the exergy efficiency of the system using R1224yd is higher than R245fa and nearly has the same amount as R123. Relevant to the result from Figure 9, in Figure 11, the exergy destruction total of R1224yd has the lowest amount compared to R123 and R245fa.

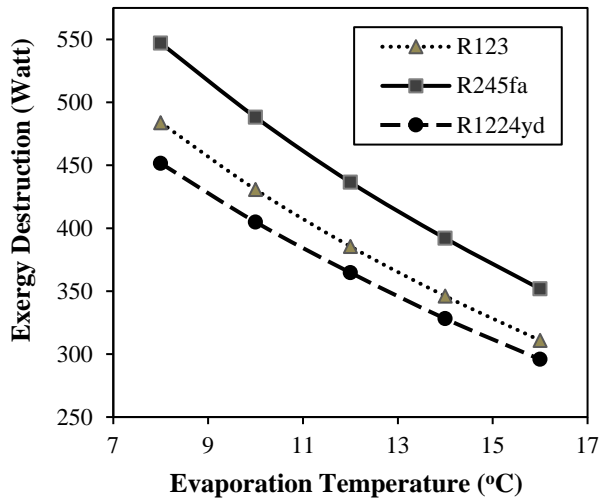


Figure 11. Exergy destruction of the system at various evaporator temperatures.

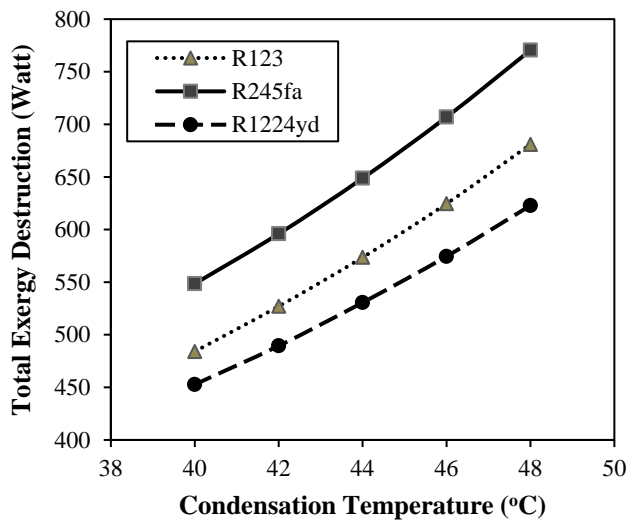


Figure 12. Exergy destruction of the system at various condenser temperatures.

From this parametric study, it observed that energy and exergy efficiencies increase when evaporating temperature increases and decrease when the condensation temperature increases. The increase in the evaporating temperature, causing the augmentation of the cooling capacity and the reduction of the compressor pressure ratio and the compressor work. Thus, COP and exergy efficiency increase. The increase in the condenser temperature is causing an increase of the pressure ratio across the compressor and its required work. Then the COP and exergy efficiency decreases.

3.3 Exergy Analysis for Each Component of the System

Figure 13 represents the exergy destruction total of four main components with variation in evaporating temperature, while Figure 14 shows the percentage of exergy destruction for each system component.

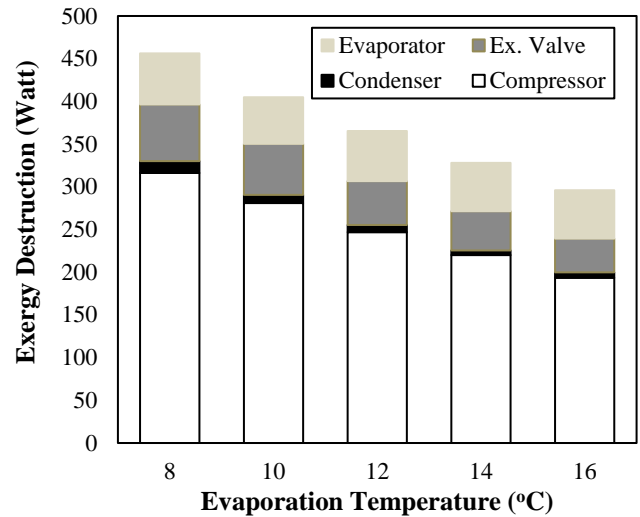


Figure 13. Effect of evaporation temperature on total exergy destruction at each component.

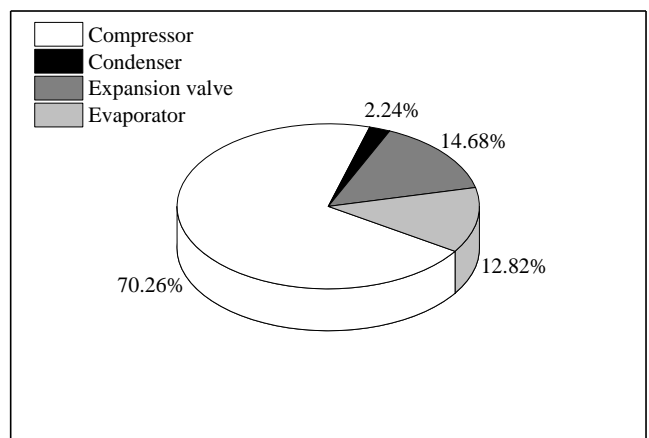


Figure 14. Percentage of exergy destruction at each component of the system.

According to Figure 14, the analysis reveals that the compressor causes the most significant loss of exergy in the heat pump system, followed by the expansion valve, evaporator, and condenser. This observation is consistent with the fact that compressors typically exhibit higher exergy losses compared to other components. The exergy destruction in the compressor is primarily due to several factors such as electrical losses, mechanical losses, and isentropic efficiency losses. These losses contribute to a significant portion of the total exergy destruction within the system. In the given analysis, it is observed that the compressor alone accounts for approximately 70% of the total exergy destruction, which amounts to around 300 Watts. The second largest component of exergy loss is found in the expansion valve and evaporator. The losses in the evaporator can be attributed to several factors, including the rise in temperature at the end of the evaporation process, which creates a temperature difference in the heat transfer process and with the surroundings.

Understanding the distribution of exergy destruction among the system components is crucial for identifying areas of potential improvement and optimization. By focusing on minimizing exergy losses in the compressor, as well as improving the performance of the expansion valve and evaporator, engineers can enhance the overall efficiency and performance of the heat pump system.

4. Conclusions

A vapor compression heat pump system with capacity of 4 kW was performed in this work. The energy and exergy analysis of low GWP refrigerant, R1224yd compared to R245fa to investigate the feasibility of using R1224yd as a substitute for R245fa which has high GWP value. R1224yd has similar physical properties to R245fa. A parametric study was conducted to ascertain the effect of evaporation and condensation temperature on energy and also exergy efficiencies. From the result, it is observed that energy and exergy efficiencies increase when evaporating temperature increases and decrease when the condensation temperature increases. Also, based on the thermodynamic modeling results, R1224yd offers better performance compared to R245fa which has 1-3% higher both in COP value and exergy efficiency. While R1224yd has the comparable performance with R123. In other words, it can be concluded that in thermodynamic and environmental point of view R1224yd is found to be potential candidate to replace R245fa and R123.

Nomenclature

\dot{m}_{in}	: massflow rate input (kg/s)
\dot{m}_{out}	: massflow rate output (kg/s)
\dot{Q}_{in}	: heat transfer rate input (Watt)
\dot{W}_{in}	: work input (Watt)
h_{in}	: enthalpy input (kJ/kg)
\dot{Q}_{out}	: heat transfer rate output (Watt)
\dot{W}_{out}	: work output (Watt)
h_{out}	: enthalpy output (kJ/kg)
COP	: Coefficient of Performance
Q_e	: heat transfer rate in evaporator (Watt)
Q_c	: heat transfer rate in condenser (Watt)
\dot{W}_{comp}	: work of compressor (Watt)
$\frac{Q_t}{T_i}$: entropy rate transfer (Watt/K)
s	: specific entropy (kJ/kh K)
S_{gen}	: entropy rate generation (kJ/kh K)
m_{ref}	: mass flowrate of refrigerant (kg/s)
Ex_e	: exergy destruction in evaporator (Watt)
Ex_{co}	: exergy destruction in compressor (Watt)
Ex_c	: exergy destruction in condenser (Watt)
Ex_v	: exergy destruction in valve (Watt)
T_a	: Ambient temperature (°C)
Ex_{in}	: exergy input (Watt)
$Ex_{D,tot}$: total exergy destruction (Watt)
Ex_{eff}	: exergy efficiency (%)

References:

[1] R. Yildirim, A. Ş. Şahin, and E. Dikmen, “Comparative Energetic, Exergetic, Environmental and Enviroeconomic Analysis of Vapour Compression Refrigeration Systems Using R515B as Substitute for R134a,” *International Journal of Thermodynamics*, 25(1), 125–133, 2022.

[2] N. Nasruddin, S. Sholahudin, N. Giannetti, and Arnas, “Optimization of a cascade refrigeration system using refrigerant C3H8 in high temperature circuits (HTC) and a mixture of C2H6/CO2 in low temperature circuits (LTC),” *Appl Therm Eng*, 104, 96–103, 2016.

[3] S. Khatoon and M. N. Karimi, “Thermodynamic analysis of two evaporator vapor compression refrigeration system with low GWP refrigerants in automobiles,”





International Journal of Air-Conditioning and Refrigeration., doi: 10.1007/s44189-022-00017-1.

- [4] M. U. Siddiqui, et al., “Recent Developments in the Search for Alternative Low-Global-Warming-Potential Refrigerants: A Review,” *International Journal of Air-Conditioning and Refrigeration*, 28, 03, 2020.
- [5] R. M.E Ahamed, J. Hossain and S. Hossain, “A Review On Hydrocarbon (HCs) As An Alternative,” *Mechanical Engineering Research Journal*, 11, 89–96, 2018.
- [6] M. Direk, M. S. Mert, F. Yüksel, and A. Keleşoğlu, “Exergetic investigation of a R1234yf automotive air conditioning system with internal heat exchanger,” *International Journal of Thermodynamics*, 21, 103–109, 2018.
- [7] H. M. Ariyadi, S. Yamaguchi, and K. Saito, “Assessment of thermal and transport properties of ionic liquids as suitable absorbent for absorption cooling applications,” in *IOP Conference Series: Materials Science and Engineering*, doi: 10.1088/1757-899X/539/1/012005.
- [8] H. M. Ariyadi, N. Giannetti, S. Yamaguchi, and K. Saito, “Comparative analysis of ionic liquids as sorptive media for absorption cooling systems,” in *Refrigeration Science and Technology*, doi: 10.18462/iir.icr.2019.1033.
- [9] H. M. Ariyadi and A. Coronas, “Absorption Capacity of Ammonia into Ionic Liquids for Absorption Refrigeration Applications,” *J Phys Conf Ser*, 745, 032105, 2016.
- [10] C. Yildirim, D.B Ozkan and C. Onan, “Theoretical study of R32 to replace R410A in variable refrigerant flow systems,” *International Journal of Ambient Energy*, 39, 87–92, 2018.
- [11] K. Nawaz, B. Shen, A. Elatar, V. Baxter, and O. Abdelaziz, “Le R1234yf et le R1234ze(E) comme frigorigènes à faible GWP pour des chauffe-eau domestiques à pompe à chaleur,” *International Journal of Refrigeration*, 82, 348–365, 2017.
- [12] F. Botticella, F. de Rossi, A. W. Mauro, G. P. Vanoli, and L. Viscito, “Multi-criteria (thermodynamic, economic and environmental) analysis of possible design options for residential heating split systems working with low GWP refrigerants,” *International Journal of Refrigeration*, 87, 131–153, 2018.
- [13] D. Wu, B. Hu, and R. Z. Wang, “Performance simulation and exergy analysis of a hybrid source heat pump system with low GWP refrigerants,” *Renew Energy*, 116, 775–785, 2018.
- [14] S. Fukuda, C. Kondou, N. Takata, and S. Koyama, “Low GWP refrigerants R1234ze(E) and R1234ze(Z) for high temperature heat pumps,” *International Journal of Refrigeration*, 40, 161–173, 2014.
- [15] C. Kondou and S. Koyama, “Thermodynamic assessment of high-temperature heat pumps using low-GWP HFO refrigerants for heat recovery,” *International Journal of Refrigeration*, 53, 126–141, 2015.
- [16] I. Y. Cho, H. J. Seo, D. Kim, and Y. Kim, “Performance comparison between R410A and R32 multi-heat pumps with a sub-cooler vapor injection in the

- heating and cooling modes,” *Energy*, *112*, 179–187, 2016.
- [17] A. Alabdulkarem, R. Eldeeb, Y. Hwang, V. Aute, and R. Radermacher, “Testing, simulation and soft-optimization of R410A low-GWP alternatives in heat pump system,” *International Journal of Refrigeration*, *60*, 106–117, 2015.
- [18] S. Yamaguchi, D. Kato, K. Saito, and S. Kawai, “Development and validation of static simulation model for CO₂ heat pump,” *Int J Heat Mass Transf*, *54*, 1896–1906, 2011.
- [19] M. Badache, M. Ouzzane, P. Eslami-Nejad, and Z. Aidoun, “Experimental study of a carbon dioxide direct-expansion ground source heat pump (CO₂-DX-GSHP),” *Appl Therm Eng*, *130*, 1480–1488, 2018.
- [20] A. H. P. Antunes and E. P. Bandarra Filho, “Étude expérimentale de la performance et de l’impact environnemental planétaire d’un système frigorifique rénové avec des frigorigènes alternatifs,” *International Journal of Refrigeration*, *70*, 119–127, 2016.
- [21] K. J. Park, T. Seo, and D. Jung, “Performance of alternative refrigerants for residential air-conditioning applications,” *Appl Energy*, *84*, 985–991, 2007.
- [22] M. Mohanraj, S. Jayaraj, and C. Muraleedharan, “Environment friendly alternatives to halogenated refrigerants-A review,” *International Journal of Greenhouse Gas Control*, *3*, 108–119, 2009.
- [23] J. A. Dopazo, J. Fernández-Seara, J. Sieres, and F. J. Uhía, “Theoretical analysis of a CO-NH cascade refrigeration system for cooling applications at low-temperatures”, *Applied Thermal Engineering*, doi: 10.1016/j.applthermaleng.2008.07.006i.
- [24] D. Zhou *et al.*, “Theoretical study of low-GWP refrigerants in high-temperature heat pump systems,” *International Journal of Low-Carbon Technologies*, *18*, 881–886, 2023.
- [25] J. Jiang *et al.*, “Experiments of advanced centrifugal heat pump with supply temperature up to 100 °C using low-GWP refrigerant R1233zd(E),” *Energy*, *263*, 2023.
- [26] F. Molés, J. Navarro-Esbri, B. Peris, A. Mota-Babiloni, and Á. Barragán-Cervera, “Theoretical energy performance evaluation of different single stage vapour compression refrigeration configurations using R1234yf and R1234ze(E) as working fluids,” *International Journal of Refrigeration*, *44*, 141–150, 2014.
- [27] Y. qiang Feng *et al.*, “Operation characteristic and performance comparison of organic Rankine cycle (ORC) for low-grade waste heat using R245fa, R123 and their mixtures,” *Energy Convers Manag*, *144*, 153–163, 2017.
- [28] S. Eyerer, F. Dawo, J. Kaindl, C. Wieland, and H. Spliethoff, “Experimental investigation of modern ORC working fluids R1224yd(Z) and R1233zd(E) as replacements for R245fa,” *Appl Energy*, *240*, 946–963, 2019.
- [29] S. Wang *et al.*, “Performance analysis on parallel condensing air-source heat pump water heater system,” *Energy Reports*, *8*, 398–414, 2022.
- [30] T. Chen and O. K. Kwon, “Experimental Analyses of Moderately High-Temperature Heat Pump Systems with R245fa and R1233zd(E),” *Energy Engineering: Journal of the Association of Energy Engineering*, *119*, 2231–2242, 2022.
- [31] Sulaiman A.Y., “Thermodynamic analysis of subcritical High-Temperature heat pump using low GWP Refrigerants: A theoretical evaluation,” *Energy Convers Manag*, *268*, 1–18, 2022.
- [32] J. Navarro-Esbri and A. Mota-Babiloni, “Experimental analysis of a high temperature heat pump prototype with low global warming potential refrigerant R-1336mzz(Z) for heating production above 155 °C,” *International Journal of Thermofluids*, doi: 10.1016/j.ijft.2023.100304.
- [33] C. Watanabe, Y. Uchiyama, S. Hirano, and H. Okumura, “Industrial Heat Pumps and Their Application Examples in Japan,” presented at *The 12th IEA Heat Pump Conference*, Rotterdam. 2017.
- [34] R. Akasaka and E.W. Lemmon, “A helmholtz energy equation of state for CIS-1-Chloro-2,3,3,3-Tetrafluoropropene(R1224yd),” in *European Conference on Thermophysical Properties*, 2017.
- [35] I. Dincer, M.A Rosen and P. Ahmadi, *Optimization of energy systems*, 1st Edition. Chennai, India. John Wiley & Sons, 2017.

Research Article

Development and Economical Analysis of Innovative Parabolic Trough Collector Integrated Solar Still

¹*M. Patil , ²I. Patil , ³S. Shekhawat , ⁴N. Nikam 

¹ Guru Gobind Singh College of Engineering and Research Centre, Nashik (MS), INDIA

² Maratha Vidya Prasarak Samaj's Karmaveer Adv. Baburao Ganpatrao Thakare College of Engineering, Nashik, INDIA

³ G. H. Rasoni Institute of Engineering and Business Management, Jalgaon (MS), INDIA

⁴ Guru Gobind Singh College of Engineering and Research Centre, Nashik (MS), INDIA

E-mails: ¹*mspiso2012@yahoo.com, ²patilishan40@gmail.com, ³spshekhawat@rediffmail.com,
⁴neelkanth.nikam@ggsf.edu.in

Received 13 June 2023, Revised 31 August 2023, Accepted 09 October 2023

Abstract

Experimental setup of the integrated parabolic trough collector (PTC) with solar still was developed. PTC was designed considering the solar geometry and the physical laws of parabolic shape and the concentrators. Test were conducted at the location with latitude 19.9975°N and longitude 73.7898°E. Theoretical analysis was done using ray tracing and engineering equation solver (EES) software while designing the system. PTC system was developed with dimensions of 1.5 m length, 1 m width and a concentration ratio (CR) of 21.22. Theoretical thermal efficiency was predicted as 48.1% whereas experimental average thermal efficiency is observed as 42.76%. The observed temperature difference between the vapor and the glass cover is about 17 °C and between ambient air and vapor is about 24.4 °C. Maximum water temperature in the conventional solar still was 64.6 °C where as for the PTC coupled solar still was 74.4 °C. PTC coupled solar still is having averagely 37% higher production rate. This has definitely added an advantage because of higher energy absorption rate compare with the conventional solar still. PTC coupled solar still system has nearly 35% more heat absorption. Total embodied energy of the system is around 896.875 kWh. Total capital cost of the system is Rs. 41300/-. Total annual output of pure water is around 3 L/Day. Estimated energy payback period is around 2.29 years and the total carbon credit earned is Rs. 2165.38 per year.

Keywords: Solar energy; solar still; parabolic trough collector, embodied energy.

1. Introduction

Three fuels coal, biomass and oil meet India's 80% of total energy demand. In India coal is the primary fuel for the electricity generation. With increase in vehicles and transportation requirements oil consumption and its import has significant impact on the economy of the India. Even the availability of the various resources of energy in India still many of the Indians not switched towards the modern fuel and relying on the conventional resources for needs like cooking [1].

Total solar radiation that reaches the Earth's surface is a dispersed because of water vapors and other gases. This radiation because of the photons is directly converted in to the electricity using photovoltaic devices, or, in to the heat energy using various concentrators. In case of the solar concentrators the solar radiation is used to heat the fluid known as heat transfer fluid (HTF). This fluid is then used for driving the thermodynamic cycle. Flat plate solar collectors and the photovoltaic cells uses both direct as well as diffuse solar radiation. However, in concentrating solar collectors scattered sunlight cannot be concentrated, CSP uses only direct sunlight and not the diffused. In

concentrating solar plants, mirrors provided on the collector surface concentrates the sun light as a point focus or line focus that's create a sufficiently high temperature level with relatively smaller heat loss. Various technologies are developed and demonstrated in CSP technologies. Based on the methods of concentration it is divided in two groups viz point focus and line focus. Trough like mirrors are used in line focus technology. This mirror concentrates the solar radiation on receiver tube that uses single axis tracking system. Parabolic Trough Collectors (PTC) and Linear Fresnel Reflector Systems (LFRS) are the examples of concentrating solar power.

PTC and LFRS designs can concentrate the solar radiation about 30 – 80 times and heats up the HTF up to the temperature of 400 °C. Generally the receiver tube is mounted at the focus point and made of steel or cooper and the tube is coated with a heat resistant black paint. Technological and financial risks involved are very low in parabolic trough technology as it is now a matured technology. Various parts of the parabolic trough collector are parabola shaped trough, mirrors, receiver tube with glasscover and support structure. Collector with parabolic

shaped mirrors focuses the sunlight towards absorber tube [2].

India facing fresh water crises and it also varies with the location and time of the year as well as on varying scale and intensity. Need of India's fresh water is changing due to continuous rise in population and the change of life style. Due to extensive use of water in all sectors like domestic, agricultural and industry ground water table availability is deeper and deeper. Same time the spreading pollution reducing the ground water quality. Millions of people of India do not have the adequate quality of the safe water during the summer season. Pollutants like arsenic, fluoride and ingress of the salt affected millions of people of India. In many parts of India still the girls and women have to walk a long distance and spend many hours to collect the fresh water for their daily needs. Gujrat, Maharashtra and Rajasthan are the major areas where such scenes are observed by the authors. In spite of the good rain fall in the state of Maharashtra shortage of fresh water is observed and large quantity of ground water is the saline water [3-6].

R.K. Khanna et al. [7] reported his findings about the water quality from the village Chui located in the state of Rajasthan. He observed that in this village nearly all the family members need to search the fresh water, collect it and store the same. He also reported that the test of water was carried at the Ajmer and it is observed that water quality was very poor and not suitable for human health. He majorly finds that the people are expecting the suitable purification device (desalination of water) that can be easily operated by them and the group of people can offer the cost. Conventional desalination technology uses the conventional energy and needs a maintenance with skilled operators. Use of solar energy for distillation is a very good solution for the need of fresh water. Solar technology is simple and clean [8]. India is located in the tropical zone and receives the plenty of sunshine with average solar radiation in the range of 4 to 7 kW/h.m². Studies so far are focused on increasing the solar still output which depends on various factors. Sathyamurthy et al. [9] reported various methods to increase the yield of solar still. Methods that improves the solar still performance and productivity includes the use of flat plate collectors with evacuated tube, heat pipes, and use of parabolic trough collector.

Initial double slope desalination system was developed by IIT Delhi during 1984 and is represented in Figure 1. Developed system has multi-wick stills with an area of 1m² each and 85 L/day capacity [10].

Garg and Mann [11] and Tiwari and Madhuri [12] reported experimental analysis on solar passive still. They observed the year round performance and concluded that Glass covers with small angle gives higher output optimum angle was reported as 10° and for low and high altitude locations single slope solar stills are recommended. It was reported that fixed height and width of the solar still with change in length output does not changes.

If the temperature difference between stored basin water and the glass-condensing surface is high solar still can have a higher production rate. Thus, it becomes important to increase the basin water temperature or to decrease the condensing glass surface temperature. Condensing surface is the surface of glass cover of the solar still. The evaporated water from the absorber tube of the PTC condenses on this surface. This surface temperature can be reduce by the water flowing over the surface.

Tiwari and Bapeshwara Rao [13] reported the study on single slope solar still as shown in Figure 2. During the experimentation they maintained the constant flow velocity of water over the glass surface. S.A. Lawrance et al. [14, 15] conducted the similar study and observed the significant yield of solar still with the large heat capacity of mass of water in the basin.

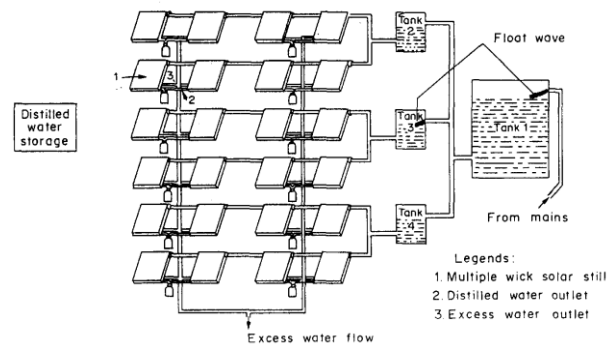


Figure 1. Multi wick distillation plant [10].

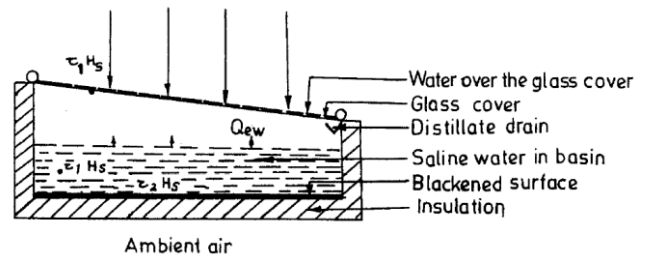


Figure 2. Solar still with water flow on glass [13].

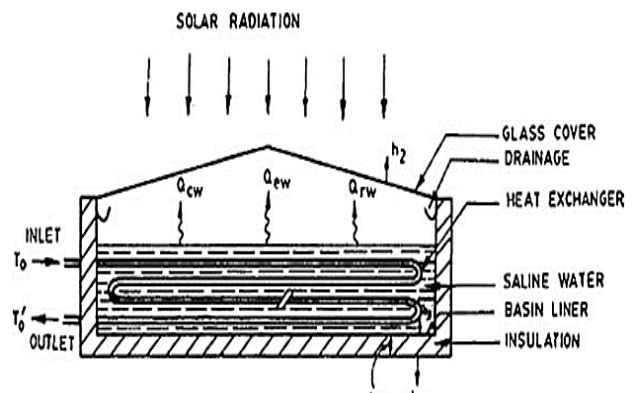


Figure 3. Solar still with internal heat exchanger [16].

Ashok Kumar and G.N. Tiwari [16] studied the use of heat exchanger in the solar still basin (Figure 3). They have developed the double slope solar still and conducted the experiment with heat exchanger installed into the basin. In this heat exchanger hot water exchanges heat energy with cold water in the basin. This way they increased the basin cold water temperature. They observed that the evaporation rate was increased with increase in the temperature of the hot water.

Materials like black rubber, aluminum sheets and gravels stores the heat energy. In addition to absorb solar radiation use of such a material in the basin increases the heat capacity. P. Valsaraj [17] reported an experimental findings using the gravels inside the solar basin. They used aluminum sheet as a floating absorber as shown in Figure 4. It was observed that compared with conventional solar still the rate of evaporation was higher. M. Sakthivel and S.

Shanmugasundaram [18] reported the similar studies using the black granite gravels and reported rise of 20% of yield.

Conventional type of solar stills have following limitations

- Since the absorbing surface is horizontal it intercepts the less solar radiation.
- Due to higher water storage capacity distilled output is also small since it has larger water heat capacities.

One solution to above limitations is decreasing the mass of water and exposing the small quantity of water to large solar radiation. This is possible by using a water wick. Blackened wet jute clothes are used for this purpose. This way water present in the jute can be heated to higher temperature and evaporation will be faster. In this case a series of jute threads separated by the polythene sheets are formed along the inclined plane whose one end is inserted in a saline water tank. Suction of water is then achieved by capillary action. Sodha et al. [19] reported the experimental study using the wick type of solar still. They observed that the cost of such a still is lower than the conventional for the same area. It was also observed that yield of the distilled water is higher and the thermal efficiency is 4% more than the conventional still. G.N. Tiwari et al. [20] also conducted the similar experiments with multiple solar stills and observed 20% more yield than the conventional still. Dhiman and Tiwari [21] conducted the experimental study with the use of wet wick and water flowing on the glass surface. They observed that the yield was increased by 10%.

Gupta et al. [22] reported the experimental study on the double basin solar still as shown in Figure 5. During the experimentation they used the waste hot water in the lower basin during the off sunshine hours. They observed that the still yield increases as the waste hot water temperature increases. Similar studies was also reported by the Ashok Kumar [23].

S.N. Rai et al. [25] has reported his experimental study with use of single basin using jute cloth inside the basin and coupled with single flat plate collector. He also added the black dye of a small quantity to water in order increase the absorptivity and improve the rate of evaporation. The Y.P. Yadav [26] he reported 30-35% more yield compare to conventional solar still reported similar experiment with use flat plate collector.

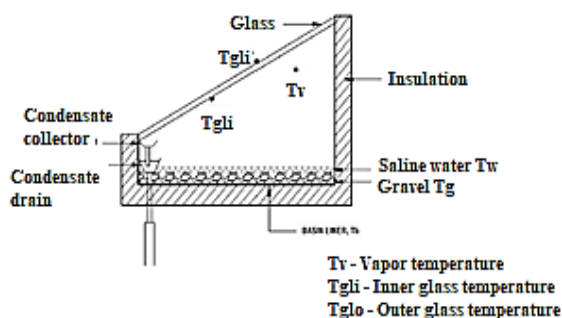


Figure 4. Solar still with internal heat exchanger [18].

Sanjeev Kumar, G.N. Tiwari [27] during their experimental studies using flat plate collector concluded that productivity of the solar still will be maximum when collector inclination is 20° and inclination of the glass cover is 15° . H.N. Singh, G.N. Tiwari [28] reported that when the condensing glass cover inclination is equal to

latitude of the location yield from the solar still will be higher.

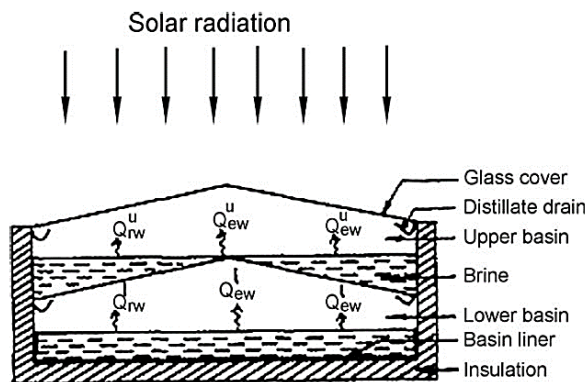


Figure 5. Double slope double basin solar still [23].

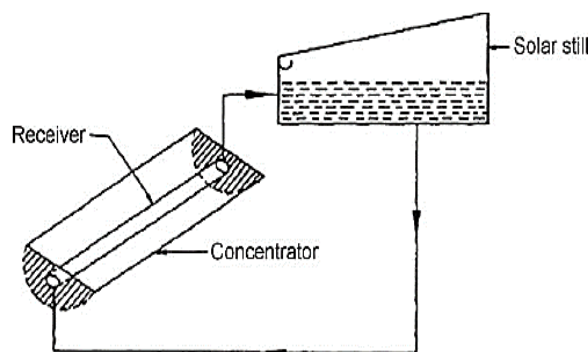


Figure 6. Solar still coupled with parabolic trough collector [29].

S.K. Singh et al. [29] reported the experimental study with the use of solar parabolic trough collector as shown in the Figure 6. They reported the 35% rise in the yield of the solar still with single basin.

Literature review findings are as summarized below

- Glass covers with small angle give higher output.
- It is better to face the solar still in east-west directions at high altitude locations.
- For low and high altitude locations single slope solar stills are recommended.
- Dyes are helpful to increase the absorptivity that leads to more evaporation.
- Decreasing the depth of water in the solar still increases the evaporation rate.
- Productivity of the solar still increases with increase in initial temperature of water.
- For the fixed height and width of the solar still with change in length output does not changes.
- Solar still can have a higher production rate if the temperature difference stored basin water and the condensing glass surface is high. Thus it become important to increase the basin water temperature or to decrease the condensing glass surface temperature.
- Use of internal heat exchanger increase evaporation rate.
- Performance of solar still will be improved by increasing the temperature of water in the basin. This is possible by making an active solar still coupled with solar PTC.

The process of integration of the PTC considers the use of solar energy for heating of water in the receiver and this hot water is then supplied to the solar still for desalination. However, this results in to the major heat losses that

includes heat loss through receiver, solar still and transmission pipe. These losses can be avoided by integrating the PTC receiver and solar still as a single device. Hence, main aim of this study was to develop integrated solar PTC solar still. The receiver of the PTC is designed to vaporize the water and the cover of the receiver was used to condense the steam. Thus it acts as a coupled solar PTC still.

2. Thermal Modeling

2.1 Introduction

System thermal modeling was conducted using the various aspects of the solar energy and its utilization. Following section discusses the details of the same.

2.1.1 Extraterrestrial Solar Radiation

Radiation following on the earth outside surface is known as extraterrestrial solar radiation. NASA has recommended the value of 1353 W/m^2 for a mean distance of $1.496 \times 10^{11} \text{ m}$. The orbit of the earth around the sun is elliptical and hence the distance of the sun from the earth has a variation of about 1.7% and hence extraterrestrial solar radiation varies by the inverse square law according to the "Eq. (1)" [30-34, 35].

$$I_o = I_{sc} \left(\frac{D_m}{D_{es}} \right)^2 \quad (1)$$

Where,

D_{es} = Distance between the sun and earth

I_{sc} = Solar constant 1353 W/m^2

"Eq. (2)" is used to calculate the value of I_o

$$I_o = I_{sc} \left[1 + 0.034 \cos \left(\frac{360 \times d_n}{365.25} \right) \right] \quad (2)$$

Where d_n is day number.

2.1.2 Terrestrial Solar Radiation

The radiation from the sun outside the earth's atmosphere is around 1353 W/m^2 . However, as it reached the earth surface its value reduces due to the effects of absorption and reflection due to the clouds, dust particles and various gas molecules. The radiation reaching on the earth surface has two different components known as beam radiation (I_b) and diffuse radiation (I_d). Beam radiation is the radiation that reaches the earth surface without scatter and the diffuse radiation is the radiation that has scattered significantly [32]. Sum of I_b and I_d is known as the global radiation (I_G). For solar concentrating collector only beam radiation is important and diffuse radiation is not considered.

2.1.3 Geometry of Parabola

PTC consist of a collector of a parabolic shape and has the cylindrical receiver at its focal distance as shown in the Figure 7. Parabolic reflector reflects all the incoming solar radiation towards the focal distance at which the cylindrical receiver tube is mounted. This reflection forms a line at the base of the receiver tube hence PTC is a line focus concentrator. The main dimensions of the parabolic collector are length (L) and the width (W) that forms the aperture area ($A_a = W \times L$). The distance between center of the parabola and outer rim is the rim radius. Rim angle (θ_r)

is the angle between reflected beam radiation by outer rim and the line joining of parabola centre and the focal point.

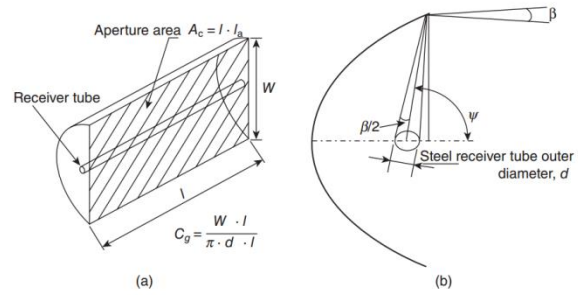


Figure 7. Geometry of the Parabola [45].

Focal length (f) of the parabola is given by the "Eq. (3)" [32, 33, 34, 35] where W is the width of parabola

$$W = 4 f \tan \left(\frac{\theta_r}{2} \right) \quad (3)$$

The geometric concentration ratio is given by the "Eq. (4)".

$$C = \frac{\text{Effective aperture area}}{\text{Receiver tube area}} = \frac{W D_{ro} L}{\pi D_{ro} L} \quad (4)$$

Concentration ratio in terms of rim angle is given by the "Eq. (5)".

$$C = \frac{\sin(\theta_r)}{\pi \sin(\theta_a)} \quad (5)$$

Where,

θ_r is the rim angle

θ_a is the acceptance angle Receiver tube diameter is given by the "Eq. (6)".

$$D_r = 2r \sin(\theta_a) = \frac{W \sin(0.267)}{\sin(\theta_r)} \quad (6)$$

2.1.4 Optical Efficiency of the PTC

The ratio of fraction of solar radiation absorb by the receiver tube to fraction of solar energy collected is known as optical efficiency and is given by the "Eq. (7)" [34, 35].

$$\eta_o = \frac{S}{I_b} \quad (7)$$

The actual amount of the solar radiation absorb by the receiver tube is given by the "Eq. (8)".

$$S = I_b (\rho_a \tau_g \alpha_r \gamma_i) K_{\theta_i} X_{END} \quad (8)$$

Where,

I_b = Beam radiation (W/m^2)

ρ_a = Absorptivity of receiver material

τ_g = Transmissivity of the glass material

γ = Intercept factor (Generally taken as 0.9 due to imperfections of reflector surface

K_{θ_i} = Incidence angle modifier

Incidence angle modifier takes care of the errors due to manufacturing defects of the collector, error due to the displacement of the receiver from focus, tracking error etc.

This incidence angle modifier factor is calculated by the “Eq. (9)” [36, 37].

$$K(\theta_i) = \cos(\theta_i) + 0.000884(\theta_i) - 0.00005369(\theta_i)^2 \quad (9)$$

Towards the end of the PTC receive tube small portion does not receive the reflected beam as shown in the Figure 8. This loss is not much significant in the long PTC system however for the short length PTC these losses must have to be considered and are given by the “Eq. (10)” [37].

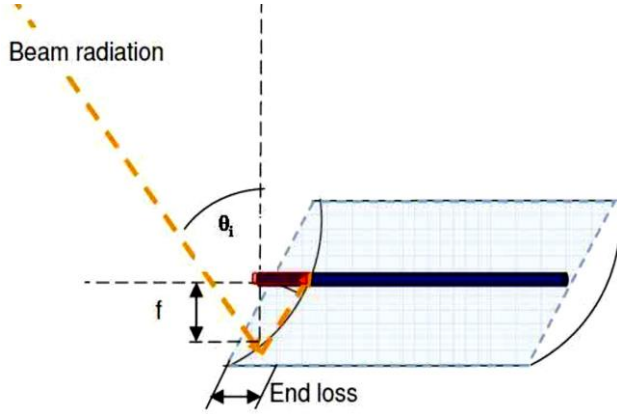


Figure 8. End loss for PTC system.

$$X_{\text{END}} = 1 - \frac{f}{L} \tan(\theta_i) \quad (10)$$

2.1.5 Heat Transfer Analysis of the PTC System

HTF flows through the receiver tube of the PTC system. HTF may be water or any thermal fluid. Thermal efficiency is then defined as ratio of heat energy absorbed by the HTF to the energy incident collector of the system [38].

2.1.5.1 Overall Heat Loss Coefficient (U_L)

Heat loss from absorber tube is because of conduction, convection and radiation. All these losses are combined together to represent them single coefficient known as overall heat transfer coefficient. Considering the convection inside the glass tube then U_L value is evaluated by “Eq. (11)”.

$$U_L = \left[\frac{A_r}{A_g(h_{c, g-amb} + h_{r, g-amb})} + \frac{1}{h_{r, r-g}} \right] \quad (11)$$

Where,

A_r = Receiver area

A_g = Receiver glass area

$h_{c, g-amb}$ = Convective heat transfer coefficient between glass and ambient due to flow of wind around glass cover

$$h_{c, g-amb} = \frac{N_U k_a}{D_g} \quad (12)$$

N_U is the Nusselt number of the air and is given by

$$N_U = 0.4 \times 0.54 \times R_e^{0.53} \quad \text{for } 0.1 < R_e < 1000 \quad (13)$$

$$N_U = 0.3 \times R_e^{0.6} \quad \text{for } 1000 < R_e < 50000 \quad (14)$$

$h_{r, g-amb}$ = Radiation heat transfer coefficient between glass and ambient

$$h_{r, g-amb} = \varepsilon_g \delta (T_g + T_{amb})(T_g^2 + T_{amb}^2) \quad (15)$$

$h_{r, r-g}$ = Radiation heat transfer coefficient between receiver tube and the glass tube

$$h_{r, r-g} = \frac{\delta(T_r + T_g)(T_r^2 + T_g^2)}{\frac{1}{\varepsilon_r} + \frac{A_r}{A_g} \left(\frac{1}{\varepsilon_g} - 1 \right)} \quad (16)$$

Where

T_r = Temperature of the receiver tube

T_g = Temperature of the glass tube

ε_r = Emissivity of receiver tube material

ε_g = Emissivity of glass tube material

δ = Stephan Boltzmanns constant = $5.67 \times 10^{-8} \text{ W/m}^2 \text{ K}^4$

2.1.5.2 Heat Transfer to HTF

Evaluation of the heat energy transfer to HTF depends on the type of flow inside the receiver tube and it is the function of Reynolds number. For flow through the tube Reynolds number is given by the “Eq. (17)”.

$$R_e = \frac{4\dot{m}}{\pi D_r \mu_f} \quad (17)$$

If $R_e < 2200$ then $Nu = 3.7$ and If $R_e > 2200$ then

$$N_U = \frac{(f_f/8) R_{ef} P_{rf}}{1.07 + 12.7 \sqrt{\left(\frac{f_f}{8}\right) [P_{rf}^3 - 1]}} \quad (18)$$

Where friction factor f_f is given by,

$$f = (0.79 \ln(R_{ef} - 1.64))^{-2} \quad (19)$$

Heat transfer coefficient, h_f is then evaluated by the equation

$$h_f = \frac{N_U f k_f}{D_r} \quad (20)$$

2.1.5.3 Heat Transfer Coefficient

Overall heat transfer coefficient was evaluated using “Eq. 21”.

$$U_O = \left[\frac{1}{U_L} + \frac{D_{ro}}{h_f D_{ri}} + \frac{D_{ro} \ln\left(\frac{D_{ro}}{D_{ri}}\right)}{2k_{rt}} \right]^{-1} \quad (21)$$

Where k_{rt} is the thermal conductivity of absorber tube material.

Collector heat removal factor for the evaluation of the thermal efficiency is calculated by the “Eq. (22)”.

$$F' = \frac{U_O}{U_L} \quad (22)$$

Thus the “Eq. (21)” is now represented as following,

$$F' = \frac{1/U_L}{\frac{1}{U_L} + \frac{D_{ro}}{h_f D_{ri}} + \frac{D_{ro} \ln\left(\frac{D_{ro}}{D_{ri}}\right)}{2k_{rt}}} \quad (23)$$

Collector heat removal factor is the ratio of the actual heat energy collected to the heat energy collected if receiver tube would be at the constant temperature and is given by the “Eq. (24)” [39].

$$F_R = \frac{\dot{m}_f c_p}{A_r U_L} \left[1 - \exp\left(-\frac{A_r U_L F'}{\dot{m}_f c_p}\right) \right] \quad (24)$$

The collector flow factor is given by the “Eq. (25)”.

$$F'' = \frac{F_R}{F'} \quad (25)$$

2.1.5.4 Thermal Efficiency of the Parabolic Trough Collector System

Thermal efficiency is the ratio of the useful energy gain by the receiver to the total solar insolation falling the aperture area.

$$\eta_{\text{thermal}} = \frac{Q_u}{A_a I_b} \quad (26)$$

The useful energy gain can be estimated as,

$$Q_u = A_a F_R \left[S - \frac{U_L (T_{fi} - T_{amb})}{C} \right] \quad (27)$$

Combining the “Eqs. (26) and (27)”,

$$\eta_{\text{thermal}} = F_R \left[\eta_o - \frac{U_L (T_{fi} - T_{amb})}{I_b C} \right] \quad (28)$$

2.1.6 Modeling Results

- Number of models were studied and found that many key parameters like, incidence angle, PTC receiver end loss, factor for cleanliness, shadow effect and day number in a year are not considered simultaneously for the analysis.
- Hence, an effort was made to develop the thermal model using EES programming language to consider these factors in one dimensional analysis of PTC receiver.
- Outcome of such model analysis will be used for development of experimental setup.

All above equations were solved simultaneously using EES for obtaining the mathematical model with following assumption

- One dimensional heat transfer analysis.
- ambient temperature is monthly average of the selected site.
- External HTC (convection coefficient is constant).
- Radiative properties of the surface are constant.
- Heat loss (Q_{loss}) was estimated assuming the grey body radiative heat exchange from the receiver tube.

The Engineering equation solver (EES) program was developed for performance estimation. Figure 9 represents the simulation results for optical efficiency and thermal efficiency of the collector evaluated for the year round thermal performance. Clean factor is assumed as 0.9 and row shading factor was 1. Maximum optical efficiency was observed as 77.19%, which, agrees with the experimental reported value of 77% by Dudley, V. E., and Workhoven [39] who reported the experimental study on parabolic

trough collector with similar setup and the glass mirror with the same range of the irradiance.

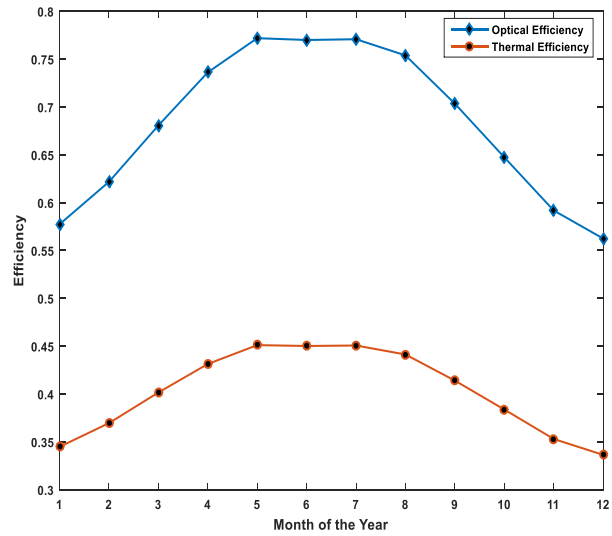


Figure 9. Optical and Thermal efficiency of the PTC System (Theoretical Modeling).

Since the results are deviated only with 0.2% model has a good validity with the published results. Model was then tested with solar trace software for validating the dimensions of the PTC. Figure 10 represents the output of the ray-tracing and it was observed that 90% of the solar radiation following on the aperture software are concentrated at the base of receiver tube with the selected dimensions of the PTC.

3. Experimental Setup

Experimental setup was installed at the institute at the location with details as Latitude 19.9975 °N and longitude 73.7898 °E. Single slope solar still was developed and is coupled with PTC system. The solar still contains a saline water at its basin (dark black color as represented in Figure 11) which is the receiver of the parabolic trough as illustrated in Figure 11.

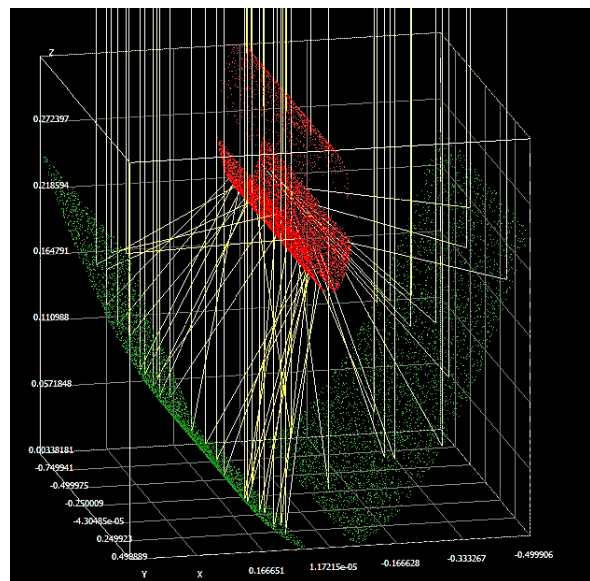


Figure 10. Validation of the system design using ray tracing.

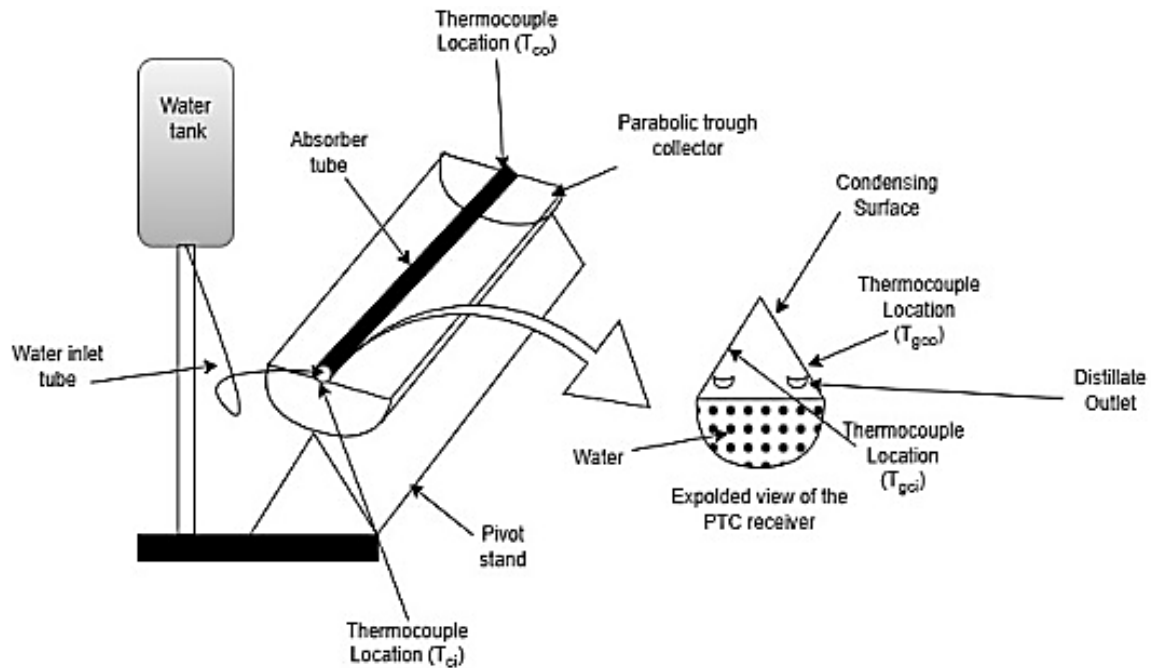


Figure 12. Schematic of the test setup.

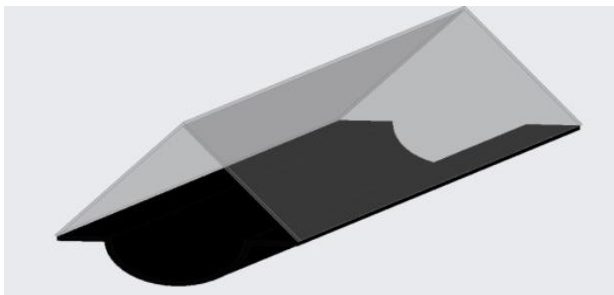


Figure 11. Inbuilt PTC receiver-solar still.

Acrylic sheets attached (light brown color in the Figure 11) forms the condensing surface. The basin is made of MS material half pipe of 1.5 mm thickness and receiver is divided in three parts throughout the length containing the porous material. For increasing the basin absorptivity receiver tube is painted with black paint (both at inside and outside). The receiver tube is fitted with an acrylic sheet covers as represented by the outline diagram Figure 11. These acrylic sheets forms the condensing surface and condensate is collected with the half cut PVC pipe provided at the bases of condensing surface. Figure 12 represents the photograph of the experimental setup with the innovative receiver tube.

Acrylic sheet is a transparent material of 4 mm thickness and two sheets were fixed with the receiver tube and angle between them is 45° with the horizontal which is the sum of the locations latitude angle and declination angle. This arrangement ensures the fall of radiations at an angle of approximately 90° and ensures maximum absorption of energy by receiver. During experimentation, system was oriented in south-north direction of the city as the maximum sun radiation falls in this direction. Silicon material was used at the joints to prevent any leakage. Distillate channels are made from the PVC pipe and are attached with the condensing surface of the still to collect the condensed freshwater. PTC system was inclined at an angle equal to latitude of the location.

Cylindrical parabolic collector was developed and the glass strips were attached on the collector sheet this concentrates solar beam radiation on the absorber tube.

Concentrator was made from the MS sheet of 0.3 mm thickness with width of 1 m and length equal to 1.5 m and aperture area of 1.5 m^2 having concentration ratio 22.6. PTC receiver tube is made of half MS pipe of 102 mm diameter. Table 1 represents the dimensions of the system.

Table 1. Test model specifications.

Sr. No	Description	Design values
01	Collector length (L)	1.5 m
02	Collector width (W)	1 m
03	Concentration ratio (CR)	22.6
04	Receiver Outer Diameter (r_o)	25.4 mm (1")
05	Receiver Inner Diameter (r_i)	21.4 mm
06	Rim Angle (Φ)	90°
07	Receiver length (L_r)	0.9 m
08	PTC Diameter (D)	1 m
09	Focal length (f)	0.250 m
10	PTC linear Diameter	1.114733 m
11	F/W ratio (f/W)	0.25

4. Results Discussion and Economical Analysis

4.1 Thermal Performance

The experimental measurements were carried out from morning at 8:00 am to evening till 5:00 pm during April 2023. Parameters like wind velocity (V), ambient temperature (T_a), inside and outside glass cover temperature (T_{gi}), (T_{go}), and temperature of water (T_w) etc. were recorded. Water temperature was measure at the center receiver tube using K-type thermocouples and temperature indicator with an accuracy of 0.1°C . The intensity of solar radiation (I) was evaluated by using developed ANN model and the HTC make solar pyranometer. Wind velocity was measured with hot wire anemometer of HTC make with a range of 0.1 to 25 m/s. Calibrated flask was used for the measurement of the condensate.

Figure 14 shows the variation of the water temperature for conventional and PTC Coupled Solar Still and Figure 13 indicates the variation in solar radiation it was observed that solar intensity increases with time till 1 PM and after this

time solar intensity decreases with increasing time. Maximum solar radiation intensity was observed at 12:45 PM. Water temperature changes with the variation in solar intensity and after 12:45 PM the temperatures decrease as shown in Figure 15. Maximum temperature difference between the vapor and the glass cover was around 17 °C and the maximum temperature difference between the receiver tube vapor and ambient air is around 24.4 °C.

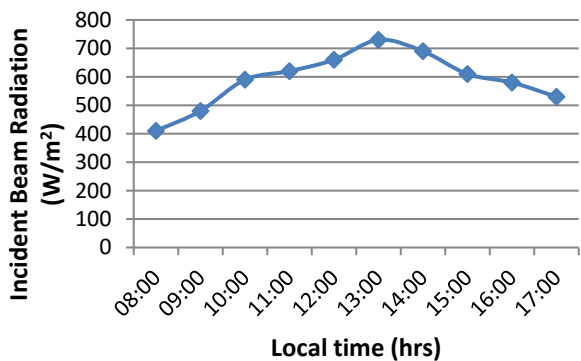


Figure 13 Incident Beam Radiation falling on the collector surface area.

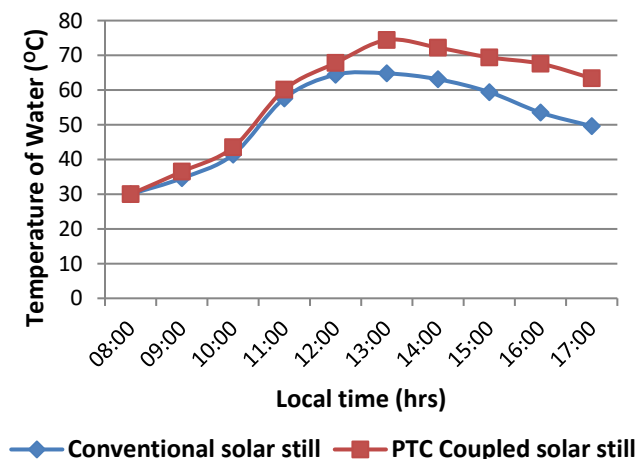


Figure 14. Comparative analysis of Conventional and PTC Coupled Solar Still.

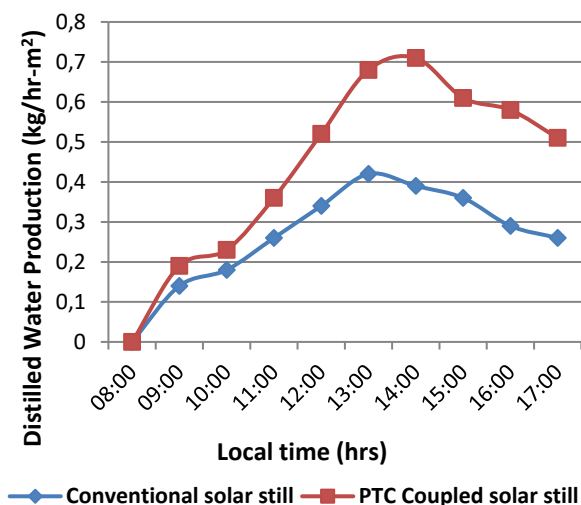


Figure 15. Comparative study of the distilled water production rate.

Figure 14 indicates that water temperature for PTC coupled solar still is more than conventional solar still this confirms the faster evaporation of the water due to the PTC use. It was observed that the temperature difference between the outer and inner acrylic sheet is around 1 °C and the maximum water temperature in case of conventional solar still is 64.6 °C and for the PTC coupled solar still is 74.4 °C.

Figure 15 shows the comparative analysis of the conventional and PTC coupled solar still for the production rate of the distilled water. It was observed that the PTC coupled solar still is having averagely 37% higher production rate. This has definitely added an advantage because of higher energy absorption rate compare with the conventional solar still.

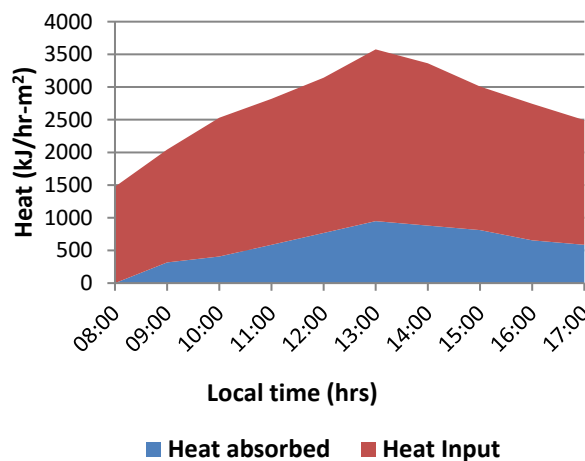


Figure 16. Heat input and absorbed for conventional solar still.

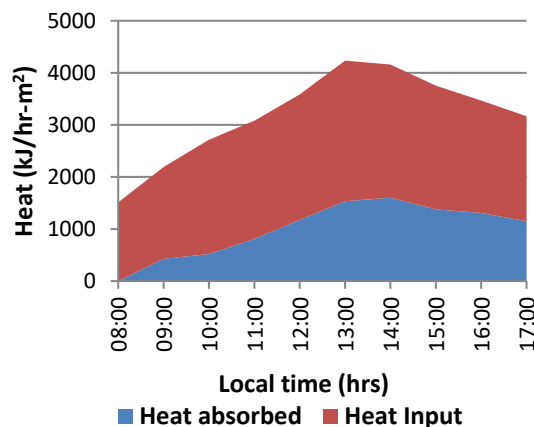


Figure 17. Heat input and absorbed for PTC coupled solar still.

Figure 16 and 17 shows the rate of heat energy absorbed by these two different systems. Section 4.2 discusses in detailed economic analysis of the system. Blue shaded area represents the heat absorbed by the conventional and PTC coupled solar still system. It was observed that the PTC coupled still system is having nearly 35% more heat absorption. Hence it would be better to propose the direct steam generation and condensation system for further studies.

Figure 18 represents the thermal efficiency performance of conventional and PTC coupled systems under this study. Since the heat absorbed across the total absorbing surface is

higher in PTC coupled system the thermal efficiency is higher by 35% in terms of production rate of the distilled water.

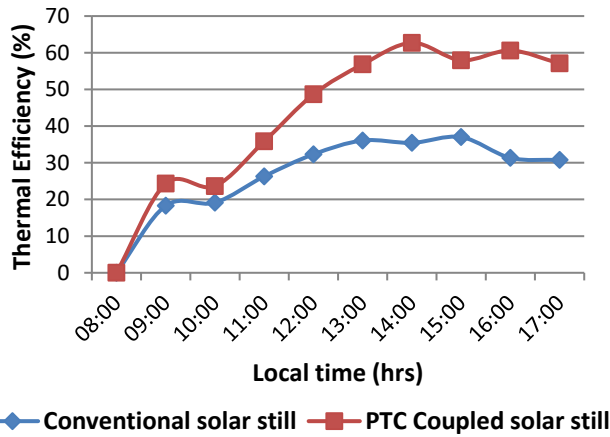


Figure 18. Comparative thermal efficiency of the systems based on distilled water production.

4.2 Economical and Energy Analysis

For any experimental setup economical and energy analysis is critical since it involves various cost including the charges for fuel, material, transportation and other.

4.2.1 Embodied Energy

Energy required for developing the system and its various parts is referred as embodied energy. This consists of the manufacturing of all parts of the PTC system as represented in Table 2.

Table 2. Embodied energy of the system.

Sr. No	Components	Material	Quantity (kg)	Embodied energy (MJ/kg)	Total (kWh)
1	Collector	MS	20	35	194.44
2	PTC stand	MS	20	35	194.44
3	Receiver tube	MS	2.5	35	24.31
4	Collector and Receiver	Glass	10	26.2	72.78
5	Inlet and exit pipe	Rubber	8	110	244.44
6	Water tank	Plastic	5	70	97.22
7	Tank insulation	Heat loan	1	14.6	4.06
8	Paint	Paint	1.5	98.1	40.88
9	Iron bush	MS	1	35	9.72
10	Receiver side flat plate	MS	1.5	35	14.58
Total Embodied Energy					896.875

4.2.2. Energy Payback Time

This is the required time to payback the entire systems embodied energy. Payback period is calculated by the “Eq. (29)” and annual output energy by “Eq. (30)” [40-44].

$$\text{Energy Payback Time} = \frac{\text{Embodied Energy (kWh)}}{\text{Annual Output Energy (kWh)}} \quad (29)$$

$$\text{Annual Output Energy (E}_{\text{out}}) = \frac{\text{Yearly distillate water (kg)} \times h_{\text{fg}} \text{ (kJ/kg)}}{3600} \quad (30)$$

h_{fg} = Latent heat of vaporization

Note: 1 kWh = 3600 kJ.

Thermal efficiency is evaluated using “Eq. (31)”,

$$\eta_{\text{thermal system}} = \frac{Q_u}{I \times A_a} \quad (31)$$

Where

$Q_u = M_y \times L_w$ Daily useful energy (W)

A_a = Total aperture area in m^2

I = Total incident solar radiation (W/m^2)

M_y = Daily output of pure water (kg/sec)

L_w = Latent heat of vaporization (kJ/kg)

4.2.3 CO₂ Emission

CO₂ released by the electricity generation from the coal has an intensity of around 0.98 kg of CO₂ /kWh and it can be calculated by “Eq. (32)” [40-44].

$$\text{CO}_2 \text{ emission per year} = \frac{\text{Embodied Energy} \times 0.98}{\text{Life Time}} \quad (32)$$

The average transmission losses are considered as 40% the distribution losses are considered as 20% for the Indian system of transmission. To consider these losses CO₂ intensity value of 0.98 is increased to 1.58 and “Eq. (32)” was modified and given by “Eq. (33)” [40-41].

$$\text{CO}_2 \text{ emission per year} = \frac{\text{Embodied Energy} \times 1.58}{\text{Life Time}} \quad (33)$$

4.2.4 CO₂ Mitigation

CO₂ is a green gas and hence mitigation is a factor that evaluates the climate change potential and it is calculated by “Eq. (34)” [40-44].

$$\text{CO}_2 \text{ Mitigation per year} = E_{\text{out}} \times 1.58 \quad (34)$$

For the entire life span CO₂ mitigation is calculated by the “Eq. (35)” [40-41].

$$\text{Total CO}_2 \text{ mitigation over the lifespan} = ((E_{\text{out}} \times \text{Life Span}) - E_{\text{in}}) \times 1.58 \times 10^{-3} \quad (35)$$

4.2.5 Earned Carbon Credit

The carbon credit is evaluated by “Eq. (36)” [40-44].

$$\text{Earned carbon credit} = \text{Net CO}_2 \text{ mitigation over the life span} \times D \quad (36)$$

Where D = Carbon credit earned.

This value varies from \$2 to \$25/ton of CO₂ mitigation Presently \$1 = Rs. 82.49 INR (dated 17 March 2023).

4.2.6 Economic Analysis

It is important to conduct the economic investigation to understand the economic feasibility of the developed setup [40-41]. Table 3 represents the cost of fabrication of the experimental test setup.

4.2.6.1 Capital Cost (CC)

Total fabrication cost of the test setup of this innovative system and as shown in Table 3.

4.2.6.2 Lifetime of the System (LT)

This is the time period over which the system is expected to provide the output and represented in terms of years of service [40-41]. For this developed system life span is taken as 30 years.

4.2.6.3 System Salvage Value (SV)

The cost of the system after its lifetime (LT) represents the salvage value (SV). For this system SV is taken as 20% of CC and is evaluated by "Eqs. (37) and (38)" [40-41].

$$SV=0.2 \times CC \quad (37)$$

"Eq. (33)" was used for the estimation of Annual salvage value (ASV).

$$ASV=SFF \text{ (Sinking Fund Factor)} \times SV \quad (38)$$

4.2.6.4 Sinking Fund Factor (SFF)

This indicates the amount that must be kept aside so that after the life time span one can developed the new system and it is calculated by "Eq. (39)" [40-41].

$$SFF = \frac{i}{(1+i)^{LT} - 1} \quad (39)$$

Where

i = interest rate (%) and LT is the life time in years

Table 3 Capital Cost of the system.

Sr. No	Component	Material	Cost (INR)
1	Parabolic Collector Side Sheets	MS	2500
2	Parabola Shape	MS	2200
3	Receiver Tube	MS	800
4	Receiver Tube Still Acrylic Sheet Cover	Acrylic	2200
5	Collector glass	Glass	2400
6	Receiver tube valves	MS	600
7	Rubber tube	Rubber	500
8	Collector stand	MS	1900
9	Other missing	--	3000
Total Cost of Equipment			16100
Labor Cost @ 35% of equipment cost			5635
Machining Cost @ 25% of equipment cost			4025
Transportation and other @ 15% of equipment cost			2415
Total Cost of Equipment			28175

4.2.6.5 Capital Recovery Factor (CRF)

To obtain the constant annual amount over certain period at certain interest it is important to obtain the capital recovery factor and it is calculated by "Eq. (40)" [40-41].

$$CRF = \frac{i(1+i)^{LT}}{(1+i)^{LT} - 1} \quad (40)$$

4.2.6.6 First Annual Cost

It is calculated by the "Eq. (41)" [40-41].

$$FAC=CC \times CRF \quad (41)$$

4.2.6.7 Annual Operational and Maintenance Cost (AOMC)

To maintain the system in terms of cleaning, mechanical maintenance, handling of the system, saline water and distillate collection it is important to obtain the annual operation and maintenance cost and is calculated by the "Eq. (42)" [40-41].

$$AOMC=0.15 \times FAC \quad (42)$$

4.2.6.8 Total Annual Cost

Total annual cost is given by the "Eq. (43)".

$$TAC=FAC+AMC-ASV \quad (43)$$

4.2.6.9 Distillate Production Cost

The distilled water output is measured by the measuring flask in L. Output of the desalination water is calculated by the "Eq. (44)" [40-41].

$$CPL = \frac{TAC}{M_y} \quad (44)$$

4.2.6.10 Payback Period

Payback period is the time taken to recover the invested cost and is given by the equation (45) [40].

$$\text{Payback Period} = \frac{\text{Investment}}{\text{Net Earning}} \quad (45)$$

Table 4 represents the summary of the above economic analysis, Payback period and the carbon credit earned with the renewable energy utilization [40-41].

5. Conclusions

Experimental analysis was conducted to analyze the performance of an inbuilt solar PTC Still. This study was conducted with an aim of improving the performance of conventional solar stills. Following conclusions are drawn.

- Conventional solar still has a low rate of evaporation. PTC has a good temperature rise because of line focus arrangement with high concentration ratio and hence useful for desalination of water.
- Evaporation increases with decrease in water depth in solar still and use of porous material.
- PTC has high concentration ratio and results in increase in temperature of water. Hence it is possible to develop an active solar still coupled with solar PTC or flat plate collector.
- Large PTC system assisted solar still are easily affordable by the group of village peoples.
- Maximum temperature difference between the vapor and the glass cover was around 17 °C and the maximum temperature difference between the receiver tube vapor and ambient air is around 24.4 °C.
- It was observed that the temperature difference between the outer and inner acrylic sheet is around 1 °C and the maximum water temperature in case of conventional solar still is 64.6 °C and for the PTC coupled solar still is 74.4 °C.
- PTC coupled solar still is having averagely 37% higher production rate. This is because of higher energy

absorption rate compare with the conventional solar still.

- PTC coupled still system has nearly 35% more heat absorption. Hence it would be better to propose the direct steam generation and condensation system for further studies.

Table 4 Summary of Economic analysis, Payback Period and Carbon Credit.

Sr. No	Cost	Value
1	Capital Cost (CC)	28175 INR
2	Life Time (LT)	30 Years
3	Salvage Value (SV)	5635 (INR)
4	Interest rate (i)	12 (%)
5	Sinking Fund Factor (SFF)	4.58×10^{-33}
6	Salvage Value (SV)	2.58×10^{-29}
7	Capital Recovery Factor (CRF)	12
8	First Annual Cost (FAC)	338100 (INR)
9	Annual Operation and Maintenance Cost	33810 (INR)
10	Annual Cost (TAC)	371910 (INR)
11	Annual output of pure water (My)	900 (L.)
12	Cost of Production (Cost of distillate)	1.132 (INR)
13	Net Sale Value	20 (INR)
14	Annual Earning	18000 (INR)
15	Payback period	1.565 (Years)
16	Embodied energy	896.87 (kWh)
17	Energy Output (Eout) Annual	564.25
18	Payback time of Energy	1.589 (Years)
19	Daily useful energy (Qu)	313.472 (W)
20	Total incident solar radiation (average of the year)	600 (W/m ²)
21	Area of the collector	1.5 (m ²)
22	Thermal efficiency	34.83 (%)
23	CO ₂ Emission per year for equivalent electricity consumption	67.58
24	CO ₂ Mitigation (Climate change potential)	26.25
25	Carbon credit earn	2165.38 (INR)

Nomenclature

A_a	Aperture area (m ²).
A_r	Receiver area (m ²).
A_g	Glass cover area (m ²).
A_{ir}	Inside cross sectional area of the absorber tube (m ²).
C	Concentration ratio.
C_p	Specific heat (kJ/kg.K).
D_{ci}	Inner diameter of a glass cover (m).
D_{co}	Outer diameter of a glass cover (m).
D_{ri}	Inner diameter of absorber (receiver) tube (m).
D_{ro}	Outer diameter of absorber (receiver) tube (m).
D_{es}	Distance between sun and earth.
d_n	Day number of the year.
E	Radiation energy.
f	Focal length (m).
F'	Collector efficiency factor.
F''	Collector flow factor.
F_R	Collector heat removal factor.
h_{fi}	Heat transfer coefficient for the HTF inside the tube (W/m ² .K).
h_w	Wind heat transfer coefficient (W/m ² .K).
I_b	Beam radiation (W/m ²).
I_b	Diffuse radiation (W/m ²).
I_G	Global radiation (W/m ²).

I_o	Extraterrestrial solar radiation (W/m ²).
I_{SC}	Solar constant (W/m ²).
k_c	Thermal conductivity of a glass cover (W/m.K).
L	Collector length (m).
Pr	Prandtl number.
Q_{abs}	Solar radiation absorb by the receiver tube (W).
Q_u	Net energy transfer to the HTF inside the receiver tube (W).
S	Solar radiation absorbed by receiver (W).
T_a	Ambient Temperature (°C).
T_i	Receiver inner surface temperature (°C).
T_{co}	Outer surface temperature of a glass cover (°C).
T_{ci}	Inner surface temperature of a glass cover (°C).
T_{fi}	HTF temperature at inlet of the receiver (°C).
T_{fm}	Mean fluid temperature (°C).
T_{sky}	Sky temperature (°C).
U_L	Receiver overall heat transfer coefficient based on receiver outside surface area (W/m ² .K).
U_o	Receiver overall heat transfer coefficient based on receiver outside tube diameter (W/m ² .K).
W	Width of parabola (m).
Wa	Parabola's aperture width (m).
X_{end}	Performance factor that accounts for losses from ends of heat collector element.

Greek Letters

α	Altitude angle (°).
α_r	Absorptance of receiver surface coating.
δ	Declination angle (°).
γ	Surface azimuth angle (°).
γ_i	Intercept Factor.
σ	Stephan Boltzmann's Constant (5×10^{-8} W/m ² .K ⁴).
ϕ	Latitude location of the solar field.
μ	Absolute viscosity of heat transfer fluid.
η_o	Optical efficiency.
η_t	Thermal collector efficiency.
θ_a	Acceptance angle.
θ_i	Angle of incidence.
θ_r	Rim angle.
θ_z	Zenith angle.
ρ_a	Clear mirror reflectivity.
ρ_f	Density of heat transfer fluid (kg/m ³).
τ_g	Transmittance of glass cover.
ω	Hour angle.
ε_{ci}	Emissance of glass cover inner surface.
ε_{co}	Emissance of glass cover outer surface.
ε_r	Emissance of receiver.

Abbreviations

ANI	Aperture normal irradiance (W/m ²).
ANN	Artificial Neural Network.
CSP	Concentrating Solar Power.
CFD	Computational Fluid Dynamics.
DNI	Direct Normal Irradiance (W/m ²).
EES	Engineering Equation Solver.
HTF	Heat Transfer Fluid.
hr	Hour.
IAM	Incidence Angle Modifier.
INR	Indian National Rupees.
PTC	Parabolic Trough Collector.
SC	Solar Collector.
LF	Linear Fresnel Reflector Systems.
L	Liter.

References:




- [1] F. Birol, IEA Report, [iea.org](https://iea.blob.core.windows.net/assets/2571ae38-c895-430e-8b62-bc19019c6807/India_2020_Energy_Policy_Review.pdf), India 2020 Energy Policy Review, https://iea.blob.core.windows.net/assets/2571ae38-c895-430e-8b62-bc19019c6807/India_2020_Energy_Policy_Review.pdf, (Accessed Sept 12, 2022).
- [2] G. Tiwari, "Solar Collectors." in *Solar Energy-Fundamentals, Design, Modelling and Applications*, IIIrd ed. Alpha Science International Ltd., 2013, ch. v, pp. 130-145.
- [3] H. Price, E. Lupfert, D. Kearney, E. Zarza, G. Cohen, R. Gee, and R. Mahoney, "Advances in Parabolic Trough

- Solar Power Technology,” *J. of Sol. Energy Eng.*, 124, 109-125, 2002. doi: 10.1115/1.1467922
- [4] D. Kearney, U. Herrmann, P. Nava, B. Kelly, R. Mahoney, J. Pacheco, R. Cable, N. Potrovitza, D. Blake, and H. Price, “Assessment of a Molten Salt Heat Transfer Fluid in a Parabolic Trough Solar Field,” *J. of Sol. Energy Eng.*, 125, 170-176, 2003. doi: 10.1115/1.1565087
- [5] A. Fernández-García, E. Zarza, L. Valenzuela, and M. Pérez, “Parabolic-trough solar collectors and their applications,” *Renewable and Sustain. Energy Rev.*, 14, 1695-1721, 2010. doi: 10.1016/j.rser.2010.03.012
- [6] C. P. Kumar, Fresh water resources: a perspective, <http://www.angelfire.com/bc/nihhrrc/documents/fresh.html>, (Accessed on Sept 12, 2022).
- [7] R. Khanna, R. Rathore, C. Sharma, “Solar still an appropriate technology for potable water need of remote villages of desert state of India-Rajasthan,” *Desalination*, 220, 645–653, 2008. doi: 10.1016/j.desal.2007.01.060.
- [8] S. Gomkale, “Operational experience with solar stills in an Indian village and their contribution to the drinking water supply,” *Desalination* 69, 177–182, 1988. doi: 10.1016/0011-9164(88)80020-1.
- [9] R. Sathyamurthy, S. A. El-agouz, P. K. Nagarajan, J. Subramani, “A Review of integrating solar collectors to solar still,” *Renew. Sustain. Energy Rev.* 5, 1–28, 2016. doi: 10.1016/j.rser.2016.11.223.
- [10] G. Tiwari, “Demonstration plant of a multi wick solar still,” *Energy Convers. and Manage.*, 24, 313–316, 1984. doi: 10.1016/0196-8904(84)90011-6.
- [11] H. P. Garg, H. S. Mann, “Effect of climatic, operational and design parameters on the year round performance of single-sloped and double-sloped solar still under Indian arid zone conditions,” *Sol. Energy*, 18, 159–63, 1976. doi:10.1016/0038-092X(76)90052-9.
- [12] G. Tiwari, Madhuri, “Effect of water depth on daily yield of the still,” *Desalination*, 61, 67–75, 1987. doi: 10.1016/0011-9164(87)80007-3.
- [13] G. Tiwari, B. Rao VSV, “Transient performance of a single basin solar still with water flowing over the glass cover,” *Desalination*, 49, 231–241, 1984. doi: 10.1016/0011-9164(84)85035-3.
- [14] S. A. Lawrence, G. Tiwari, “Theoretical evaluation of solar distillation under natural circulation with heat exchanger,” *Energy Convers. and Manage.*, 30, 205–13, 1990. doi: 10.1016/0196-8904(90)90001-F.
- [15] S. K. Singh, G. Tiwari, “Analytical expression for thermal efficiency of a passive solar still” *Energy Convers. and Manage.* 32, 571–576, 1991. doi: 10.1016/0196-8904(91)90117-2.
- [16] A. Kumar, G. Tiwari, “Use of waste hot water in double slope solar still through heat exchanger,” *Energy Convers. and Manage.*, 30, 81–99, 1990. doi: 10.1016/0196-8904(90)90017-S.
- [17] P. Valsaraj, “An experimental study on solar distillation in a single slope basin still by surface heating the water mass” *Renew. Energy*, 25, 607–612, 2002. doi: 10.1016/S0960-1481(01)00094-5.
- [18] M. Sakthivel, S. Shanmugasundaram, “Effect of energy storage medium (black granite gravel) on the performance of a solar still,” *Int. J. of Energy Res.*, 32, 68–82, 2008. doi: 10.1002/er.1335.
- [19] M. S. Sodha, A. Kumar, G. Tiwari, R. C. Tyagi, “Simple multiple wick solar still: analysis and performance,” *Sol. Energy*, 26, 127–131, 1981. doi: 10.1016/0038-092X(81)90075-X.
- [20] G. Tiwari, S.B. Sharma, M. S. Sodha, “Performance of a double condensing multiple wick solar still,” *Energy Convers. and Manage.*, 24, 155–159, 1984. doi: 10.1016/0196-8904(84)90028-1.
- [21] N. Dhiman, G. Tiwari, “Effect of water flowing over the glass cover of a multi-wick solar still,” *Energy Convers. and Manage.*, 30, 245–250, 1990. doi: 10.1016/0196-8904(90)90006-K.
- [22] R. Gupta, S. Rai, G. Tiwari, “Transient analysis of double basin solar still intermittent flow of waste hot water in night,” *Energy Convers. and Manage.*, 28, 245–249, 1988. doi: 10.1016/0196-8904(88)90030-1.
- [23] A. Kumar, J. Anand, G. Tiwari, “Transient analysis of a double slope-double basin solar distiller,” *Energy Convers. and Manage.*, 31, 129–139, 1991. doi: 10.1016/0196-8904(91)90065-Q.
- [24] S. Rai, G. Tiwari, “Single basin solar still coupled with flat plate collector. *Energy Convers. and Manage.*, 23, 145-149, 1983. doi: 10.1016/0196-8904(83)90057-2.
- [25] S. Rai, D. Dutt, G. Tiwari, “Some experimental studies of a single basin solar still,” *Energy Convers. and Manage.*, 30, 149–153, 1990. doi: 10.1016/0196-8904(90)90026-U.
- [26] Y. Yadav, “Analytical performance of a solar still integrated with a flat plate solar collector: thermo siphon mode,” *Energy Convers. and Manage.*, 31, 255–63, 1991.
- [27] S. Kumar, G. Tiwari, “Optimization of collector and basin areas for a higher yield for active solar stills,” *Desalination*; 116, 1–9, 1998. doi: 10.1016/S0011-9164(98)00052-6.
- [28] H. Singh, G. Tiwari, “Monthly performance of passive and active solar stills for different Indian climatic conditions,” *Desalination*, 168, 145–50, 2004. doi: 10.1016/j.desal.2004.06.180.
- [29] S. Singh, V. Bhatnagar, G. Tiwari, “Design parameters for concentrator assisted solar distillation system,” *Energy Convers. and Manage.*, 37, 247–52, 1996. doi: 10.1016/0196-8904(95)00166-B.
- [30] F. Mohamed, M. Hassan and A. Salem, “Experimental study on the effect of coupling parabolic trough collector with double slope solar still on its performance,” *Sol. Energy*, 163, 54–61, 2018.
- [31] D. Subhedar, G. Dattatraya, K. Chauhan, K. Patel, and B. Ramani, “Performance Improvement of a Conventional Single Slope Single Basin Passive Solar Still by Integrating with Nanofluid-Based Parabolic Trough Collector: An Experimental Study,” *Materials*

- Today: Proceedings*, 26 (Part 2): 1478–1481, 2020. doi: 10.1016/j.matpr.2020.02.304.
- [32] J. Madiouli, A. Lashin, I. Shigidi, I. Badruddin, and A. Kessentini, "Experimental Study and Evaluation of single slope solar still combined with flat plate collector, parabolic trough and packed bed," *Sol. Energy*, 196, 358–366, 2020. doi: 10.1016/j.solener.2019.12.027.
- [33] N. Bhavsar, P. Dhruv, M. Patel, S. Vaghela, U. Bhargav, and A. Patel, "New technique for water desalination using novel solar still and parabolic trough collector," *J. of Emerg. Technol. and Innovative Res.*, 6 (5), 342–346, 2019.
- [34] S. Abdallah, O. Badran "Sun tracking system for productivity enhancement of solar still ", *Desalination*, 220, 669–676, 2008. doi:10.1016/j.desal.0000.00.000.
- [35] M. Iqbal, "An Introduction to Solar Radiation," Academic Press, Toronto, 1983.
- [36] J. Sheldon, "Optical and Thermal Effects in Linear Concentrating Collectors," Ph.D. dissertation, *Diss. George Institute of Technology*, Atlanta, US, 1979.
- [37] V. Dudley, G. Mahoney, A. Mancini, T. Matthews, C. Sloan, and D. Kearney, "Test Results: SEGS LS-2 Solar Collector," *Sandia National Laboratories*, SAND, 94, 1994.
- [38] E. Jacobson, N. Ketjoy, S. Nathakaranakule, and W. Rakwichian, "Solar parabolic trough simulation and application for a hybrid power plant in Thailand," *Sci. Asia*, 32, 187-199, 2006. doi: 10.2306/scienceasia1513-1874.2006.32.187.
- [39] V. Dudley, and R. Workhoven, "Performance testing of the Solar Kinetics T-700A Solar Collector", United States: N. p., 1982. Web. doi:10.2172/6589695.
- [40] P. Singh, K. Anil, N. Chayut, "Thermo-environmental and drying kinetics of bitter melon flakes drying under north wall insulated greenhouse dryer," *Sol. Energy*, 162, 205–216, 2018. doi: 10.1016/j.solener.2018.01.023.
- [41] V. Shrivastava and A. Kumar, "Embodied Energy Analysis of the Indirect Solar Drying Unit," *Int. J. of Ambient Energy*, 38, 280-285, 2015. doi: 10.1080/01430750.2015.1092471.
- [42] K. Subbarama, S. Kumar Natarajan, V. Ramesh, S. Mani, T. Pappala, A. Kurada, M. V. Praveen Lakamsani, "Energy, exergy, economic and environmental (4E) analyses of solar still with paraffin wax as phase change energy storage material," *Materials Today*, 90, 1-5, 2023, doi: 10.1016/j.matpr.2023.03.345.
- [43] S. Shoeibi, N. Rahbar, A. Abedini, H. Kargarsharifabad, "Energy matrices, economic and environmental analysis of thermoelectric solar desalination using cooling fan," *J. of Thermal Anal. and Calorimetry*, 147, 9645–9660, 2022. doi: 10.1007/s10973-022-11217-7.
- [44] K. Skillington, R. Crawford, G. Warren-Myers, K. Davidson, "A review of existing policy for reducing embodied energy and greenhouse gas emissions of buildings," *Energy Policy*, 168, 2022. doi: 10.1016/j.enpol.2022.112920.
- [45] Concentrating Solar Power Technology, Second Edition, Principles, Developments, and Applications Woodhead Publishing Series in Energy, Pages 219-266, 2021. doi: 10.1016/C2018-0-04978-6.

Research Article

Computational Fluid Dynamics Analysis of a Solar Dryer with Various Phase Change Materials

¹*C. Mamulkar , ²S. Ikhar , ³V. Katekar 

^{1,2} Dept. of Mechanical Engineering, Karamveer Dadasaheb Kannamwar College of Engineering, Nagpur, MH, India.

³ Centre for Technology Alternatives for Rural Areas, Indian Institute of Technology Bombay, Powai, Mumbai, MH, India.

E-mail: ¹*mechetan2016@gmail.com

Received 7 July 2023, Revised 20 October 2023, Accepted 22 October 2023

Abstract

A phase change material (PCM) is an organic (or inorganic) chemical that may store and release thermal energy in latent form as it changes physical states. This investigation aims to see how phase transition materials influence the thermal efficiency of the solar dryer. For the performance analysis, three PCMs were used: paraffin wax, lauric acid, and palmitic acid. As drying material, 5 mm thick potato slices were employed. According to the computational results, the total input thermal energy for the dryer for paraffin wax, lauric acid, and palmitic acid was about 17.36 MJ, 18.46 MJ, and 17.76 MJ, respectively, for 2 kg drying mass. When paraffin wax, lauric acid, and palmitic acid were utilized, the overall efficiency of the dryer increased by about 87%, 40.2%, and 12.4%, respectively, compared to the conventional dryer. By comparing the results of simulations and predictions, it is concluded that paraffin wax is the best-performing PCM for solar dryers as the energy storage material.

Keywords: *Computational fluid dynamics; heat transfer; lauric acid; palmitic acid; paraffin wax; phase change materials.*

1. Introduction

Since ages, food and agricultural harvests have been dried under the sun. On the other side, this procedure is troubled with issues, such as items hampered by weather conditions, including rain, wind, humidity, birds and dust. Besides this, the method is labor-intensive, time-consuming, and necessitates extensive product dispersion to dry. The alternative ways of drying those products using heat from electricity or burning biomass are expensive and not environmentally friendly. In this situation, solar drying can be applied. Small food processing businesses may employ solar dryer technology to create nutritious, premium food products. As per National Horticulture Database (3rd Advance Estimates) published by National Horticulture Board, during 2021-22, India produced 107.24 million metric tons of fruits and 204.84 million metric tons of vegetables [1-3].

Significant moisture levels may be found in various fruits and vegetables. The food sector uses high-tech drying apparatus, including ice cream, drum, and steam dryers, which control the market for food goods. Such dryers have a high market value. Thus, only substantial businesses can afford them. Most small-scale grocery businesses that work with the farmer cannot pay for the pricing owing to the hefty start-up expenses. As a result, such companies and farmers have started to favor low-cost and simple drying solutions. For thousands of years, farming and other foodstuffs have been dried in sunlight & air outside. In several developing nations, solar dryers are one of the most effective and efficient methods to use energy from the sun for drying and space heating. Solar dryers in emerging markets are widely

used for drying tobacco, tea, jaggery, coffee, grammes, grapes and spices [4-6].

Herbal and spice products are commonly dried in several South East Asian nations. However, because of weather circumstances, the application of sunlight for drying is restricted owing to loss due to the body's reaction on unpredictable wet days. It has been found that prolonged contact of agricultural goods with the sunlight on hot days might cause hardening. Hardening occurs without the use of crop goods. It traps humidity within the exterior layer, causing crops to be spoiled. For these reasons, solar drying emerges as a novel method for its preservation [7-9].

2. Literature Review

Lower thermal efficiency is the primary reason behind the unpopularity of solar drying in society. Hence, some arrangement is necessary to improve the solar dryer's thermal performance. Therefore, a literature review was conducted to understand methods for improving the thermal efficiency of solar dryers.

Hii et al., [1] showed that solar drying (placing the crops beneath direct sunlight) was feasible; however, the product obtained was of inferior quality due to contamination because of dirt, bugs, winged animals, dogs, and even precipitation. Furthermore, direct exposure to bright beams caused a depletion of vitamins and nutrients, dietary supplements, and have taken a long time to dry out.

Umogbai et al., [2] investigated the difference between solar drying and sunlight-based drying. They discovered that sunlight-based dryers produce greater temperatures, lesser relative humidity, less product wetness, and lesser

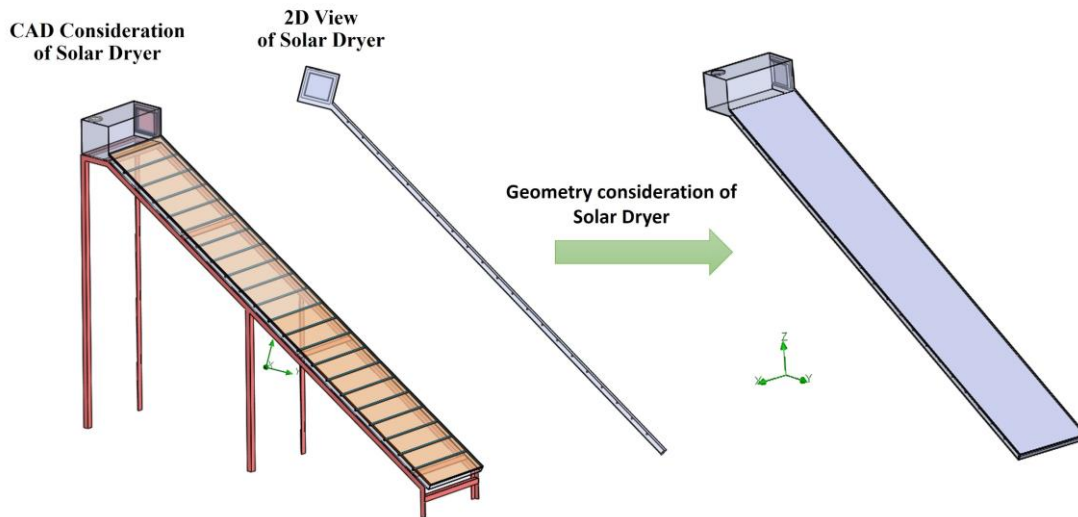


Figure 1. CAD modelling of solar dryer.

degradation throughout the drying process. Rajeshwari and Ramalingam [10] showed that when sun-oriented dryers were used instead of outdoor drying, drying time was reduced by roughly 20%, while the dried products were of a more excellent standard.

Some of the publications on tunnel dryers, halfway and half dryers and even, vertical dryers, multiple-pass dryers, and dynamically detached dryers are all investigated in various sizes and designs. They came up with common conclusions that their systems were energy efficient and will be effective for drying applications [11-18].

The effectiveness of an indirectly conduction-driven solar chilly dryer paired with a thermal storage material was constructed by Megha S. Sontakke and Sanjay P. Salve [19]. The chilies were dried in the bottom and upper containers, ranging from a starting humidity level of 72.8% to ending humidity levels of 9.2% and 9.7% (wet premise), respectively.

Toshniwal et al., [20] demonstrated the design and construction of a direct natural convection sun drier for drying tapioca in remote places. The study showed that an entire batch of 100 kg of cassava had been dried in 20 hours (2-day drying cycle), which requires a solar panel with a minimum size of 7.56 m². Seemingly, 79% and 10% moist basis were the first and ultimate moisture content rates. Given a peak everyday total radiation level from the sun on the ground's surface of 13 MJ/m²/day, the typical surroundings are 32°C air temperature and 74% relative humidity [21-22].

The primary goal of the current research is to maximize the efficiency of the solar dryer during off-sunshine hours. Using ANSYS flow simulation software, every aspect of assessment was completed.

The novelty of this research is that PCM tubes were kept horizontally at the bottom of the absorber copper plate instead of vertically at the top of the absorber copper plate, which was generally found in the literature.

3. Methodology

The various steps used to conduct the analysis were as follows:

- Design of solar dryer equipped with PCM.
- Finalize the dimensions.
- Drawing in Catia V5 software.

d) CFD simulations

e) Analyzing the results.

SolidWorks flow simulation V-2020 was used to analyse the solar dryer. The computations were necessary to design the model to investigate the interaction of liquids and gases with the surfaces determined by boundary conditions. Software enhanced the precision and speed of complicated modelling situations, including turbulent flows, as the result of continuing studies.

3.1 Design Model

SolidWorks structures from the analysis system have been selected; then, the properties of the materials have been added from engineering data or material library. The material chosen for analysis was copper plate mounted on mild steel as the base part, clear glass, which produced a greenhouse effect and paraffin wax, lauric acid and palmitic acid for energy storage. The 3-dimensional sketch was designed in geometry and open design modeler. Figure 1 shows the 3D structure of a solar dryer.

A CAD model based on the phase change characteristics of several materials was developed to conduct a CFD analysis of the solar dryer. The solar dryer has two parts, mainly duct and drying cabinet. The air channel consists of glass, copper absorber plate and copper tubes filled with PCM. On the other hand, the drying cabinet where materials to be dried located, consists of shelves and exhaust fan used to intake the air from the atmosphere through the duct channel and the drying cabinet.

The function of air heaters is to heat the air. Therefore, the hot air from the atmosphere enters the duct bottom area, which releases heat to the PCM tubes and furthers the air exhaust through the drying cabinet. Hence, in this way, PCM materials store heat from the hot air and release it during off-sunshine hours for drying. Palmitic acid, lauric acid, and paraffin wax were the investigated materials. They were placed in copper tubes on the underside of the absorber copper plate.

Properties of several materials used in the construction of solar dryer are depicted in Table 1.

The absorber tubes have been modelled for the material's types and boundary conditions. According to the fluid condition (hydraulic diameter and fluid velocity), turbulence conditions are applied for investigation. The mesh size in this

analysis is kept at standard state. The properties of PCMs used are listed in Table 2.

Table 1. Properties of solid materials used in a solar dryer.

Material	Density (Kg/m ³)	Specific heat (J/kgK)	Thermal conductivity (W/mK)
Copper	8954	383	386
Mild Steel	7680	445	45
Glass	2500	670	0.7443

Table 2. Characteristics of the specified materials.

SN	Thermo-physical properties	Units	PCM Material		
			Palmitic Acid	Lauric Acid	Paraffin Wax
1	Density	kg/m ³	860	880	900
2	Specific heat	kJ/kg K	2.4	2.3	2.5
3	Thermal conductivity	W/m K	0.2	0.18	0.23
4	Latent heat of fusion	kJ/kg	200	230	220
5	Melting temperature	°C	63	44	60

As seen in Table 2, lauric acid has a higher latent heat of fusion than palmitic acid and paraffin wax. In contrast, paraffin wax has a far higher density, specific heat, and thermal conductivity.

3.2 Boundary Conditions

The air input velocity is 1 m/sec at the atmospheric temperature of 25°C; the solar irradiation intensity is observed to be 733 W/m². The following Table 3 lists all boundary conditions.

Table 3. Boundary conditions of the Model.

Boundary conditions		
Parameters	Units	values
Solar Irradiation	W/m ²	733
<i>Inlet air conditions:</i>		
Temperature	°C	25
Humidity	%	50
Velocity	m/s	1
Ambient material temp	°C	25
<i>Outlet air conditions</i>		
Temperature	°C	52
Humidity	%	76
Pressure	bar	1.01325

3.3 Heat Transfer Rate

In a given system, heat transfer is the movement of heat across the system's boundaries due to a temperature difference between the system and its surroundings. As a result, it is an indicator of the particle's kinetic energy when there is a difference in temperature between a hot and cold body (or bodies). For a particular system, the rate of heat transfer relies on the mass (m) of the system, the specific heat capacity (c), and the temperature differential (ΔT) between the hot and cold bodies. As a result, the sensible heat transfer equation is as follows:

$$Q = mc\Delta T \quad (1)$$

However, the heat transfer rate is governed by the well-known three modes of heat transfer. They are described as below:

i) Heat transfer by conduction is the process of transmitting energy from one medium particle to another when the particles are in touch with each other.

$$Q = \frac{kA(T_{hot} - T_{cold})}{d} \quad (2)$$

This is called Fourier's law of heat conduction.

ii) Heat transfer by convection is described as the movement of fluid molecules from higher to lower temperature zones.

$$Q = hA(T_{hot} - T_{cold}) \quad (3)$$

The equation 3 is called Newton's law of cooling.

iii) Heat transfer by radiation refers to thermal radiation. The emission of electromagnetic waves produces thermal radiation. These waves carry away the energy from the producing body. Radiation is transmitted via a vacuum or a transparent material, whether solid or liquid. Thermal radiation is caused by the random movement of molecules in materials. The movement of charged electrons and protons causes the emission of electromagnetic radiation.

$$Q = \epsilon \sigma A(T_{Hot}^4 - T_{Cold}^4) \quad (4)$$

This equation is called Stefan Boltzmann's law.

4. Results & Discussions

This section illustrates the computational results obtained and its consequences on the performance of solar dryer.

4.1 Temperature Distribution for Different PCM

Figures 2 (2a, 2b, 2c) and 3 (3a, 3b, 3c) show the temperature distribution of lauric acid, palmitic acid and paraffin wax in the duct area. Nevertheless, Figure 4 (4a, 4b, 4c) shows that the temperature distribution of paraffin wax in the drying cabinet is satisfactorily greater than lauric acid and palmitic acid, respectively, because paraffin wax has higher thermal conductivity and specific heat than the other two.

4.2 Air Flow Velocity Contours Inside Chambers

Figures 5 (5a, 5b, 5c) and 6 (6a, 6b, 6c) show the airflow velocity contours inside the whole system and only inside the drying cabinet. It illustrated that although the air flow velocity is constant for all the three cases; the outlet temperature of air coming from duct fitted with paraffin wax has highest temperature as compared to other PCMs. The reason behind this is the superior thermo-physical properties of paraffin wax.

4.3 Temperature Distribution of Air

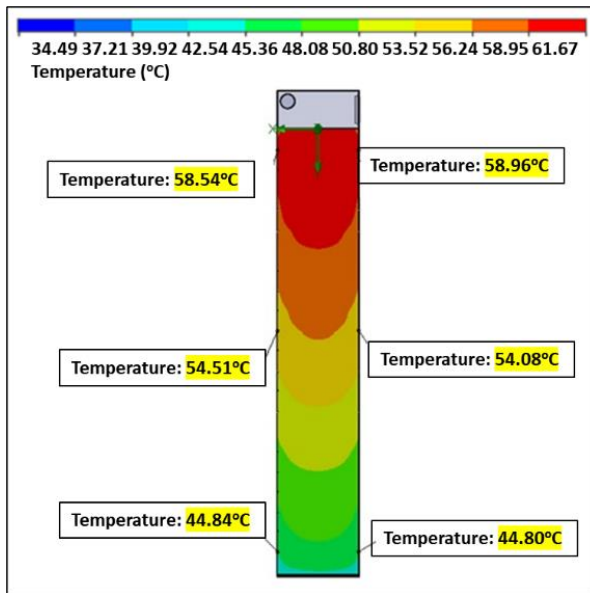
Figure 7 shows that the air temperature distribution in the entire system is better in paraffin wax compared to lauric acid and palmitic acid because it has high density and high thermal conductivity compared to the other two.

4.4 Temperature Distribution of Air at Chamber

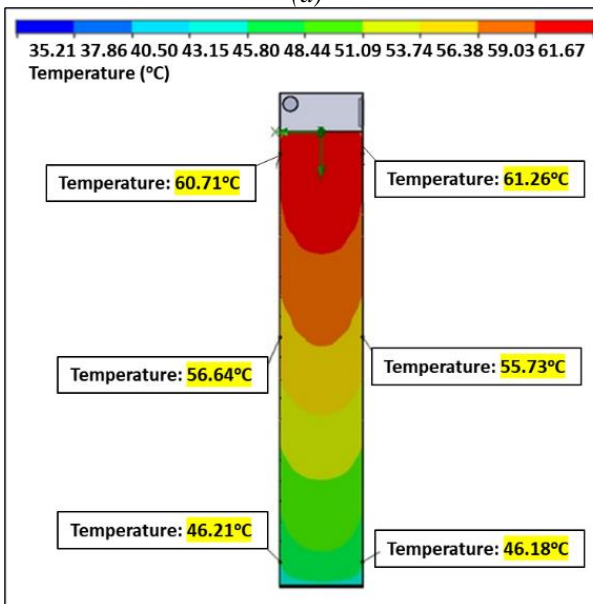
Temperature analysis of air on the fluid at the drying chamber for lauric acid was an average of 53.0°C, while in the case of palmitic acid, it was 51.20°C and for paraffin wax, it was 56.30°C as shown in figure 8.

4.5 Model Analysis

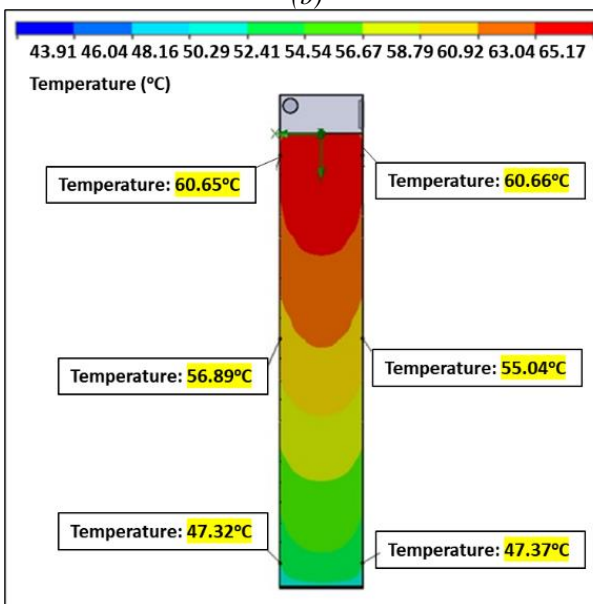
Overall airflow and temperature distribution results clearly show the results in comparison between all three materials for PCM during the experiment in the solar dryer in CFD. Air temperature at the exhaust surface is shown in



(a)



(b)

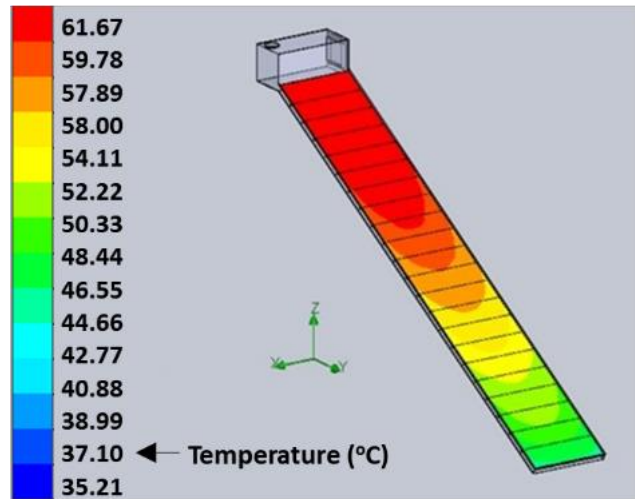


(c)

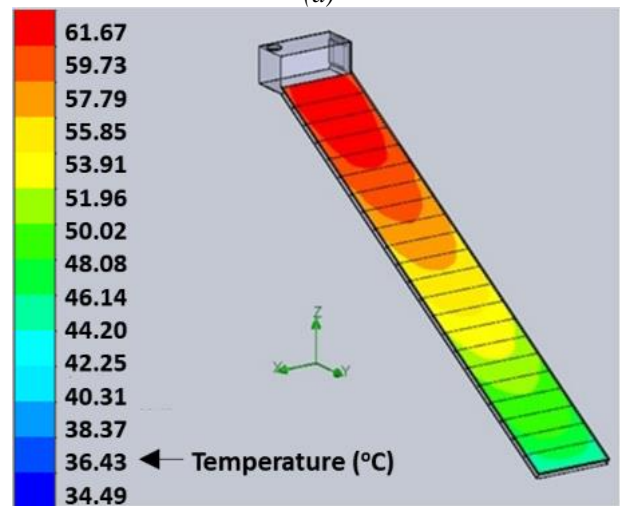
Figure 2. Temperature distribution of Copper Plate of Solar Dryer (Top View) in (a) Palmitic acid, (b) Lauric acid, (c) Paraffin.

Figure 9., where the Y axis denotes the change in temperature at 0° C. In contrast, the X axis indicates lauric acid, paraffin wax and palmitic acid. It has been concluded that paraffin wax has a much better temperature rise, as shown in Figure 9.

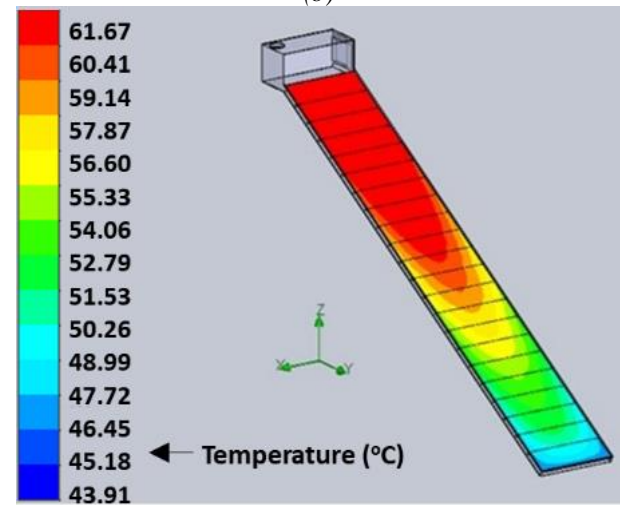
Heat transfer rate from paraffin wax has higher as compared to lauric acid and palmitic acid, respectively, shown in Figure 10.



(a)

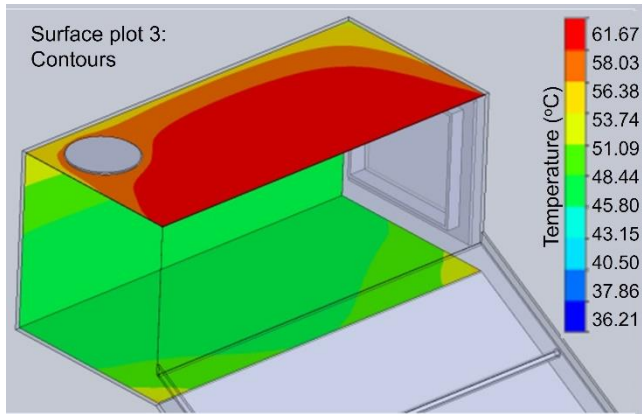


(b)

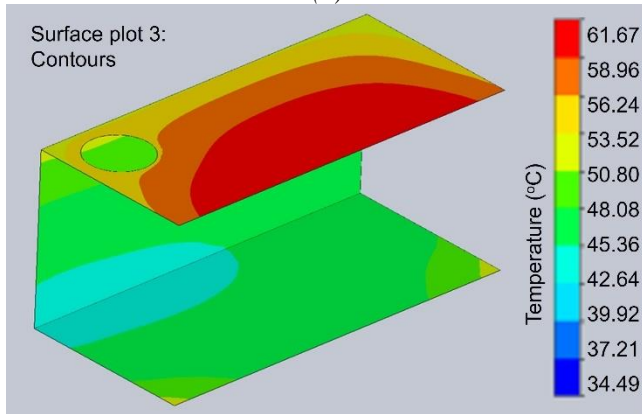


(c)

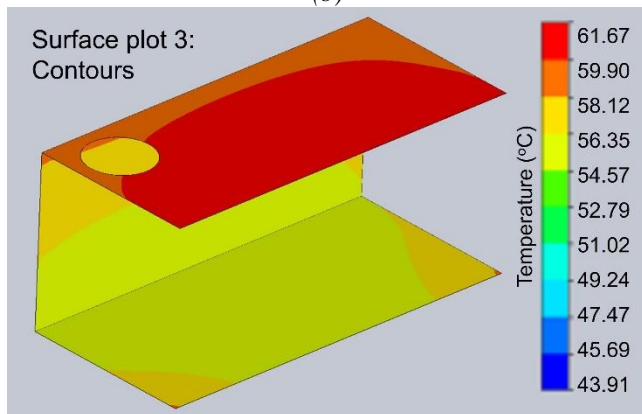
Figure 3. Temperature Distribution (Schematic View) in (a) Lauric acid (b) Palmitic acid & (c) Paraffin wax.



(a)



(b)



(c)

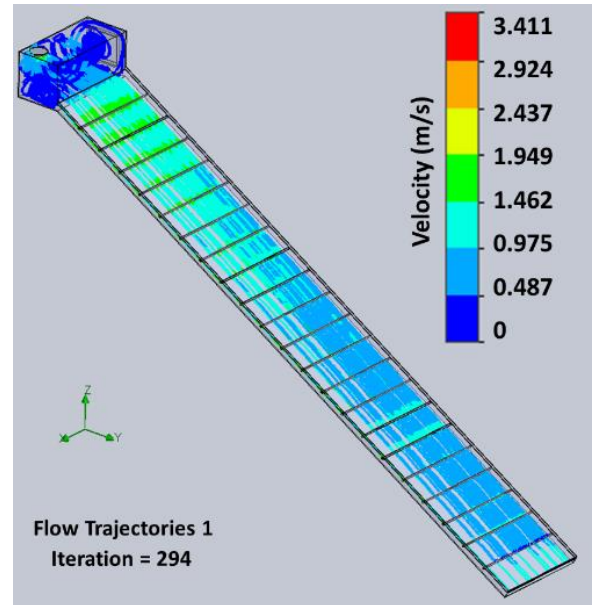
Figure 4. Temperature distribution in drying cabinet in (a) lauric acid (b) palmitic acid (c) paraffin wax.

The heat transfer rate observed during analysis is represented by the Figure 10. It shows that the heat transfer rate of the paraffin wax is 252W, much more significant than lauric acid having 225W and palmitic acid having 210W, since paraffin wax has higher thermal conductivity, specific heat and density.

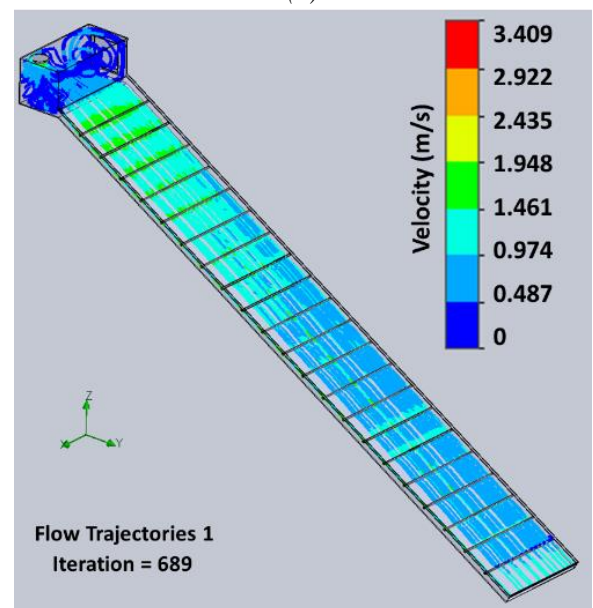
5. Conclusion

The present research investigates the best-performing PCM for solar dryers and air heaters. The three distinct PCMs, palmitic acid, lauric acid and paraffin wax, were analyzed using the latest simulation technology. From this investigation, the following conclusions are drawn:

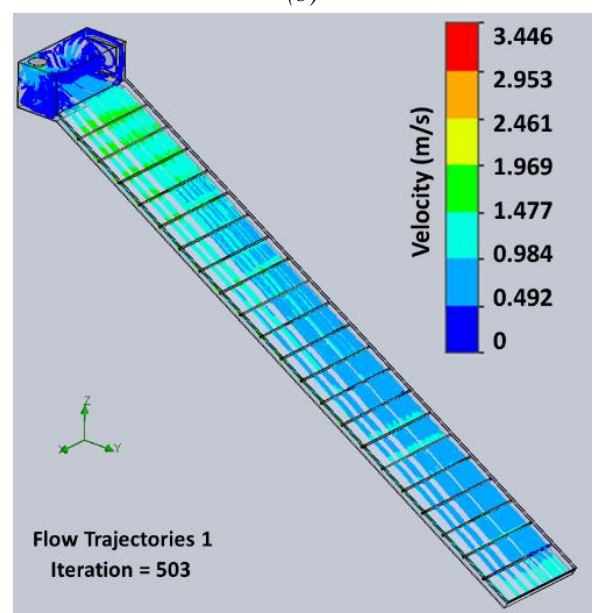
According to the computational analysis, the dryer needed about 17.36 MJ, 18.46 MJ, and 17.76 MJ of heat energy to dry 2 kg of potatoes using paraffin wax, lauric acid, and palmitic acid.



(a)

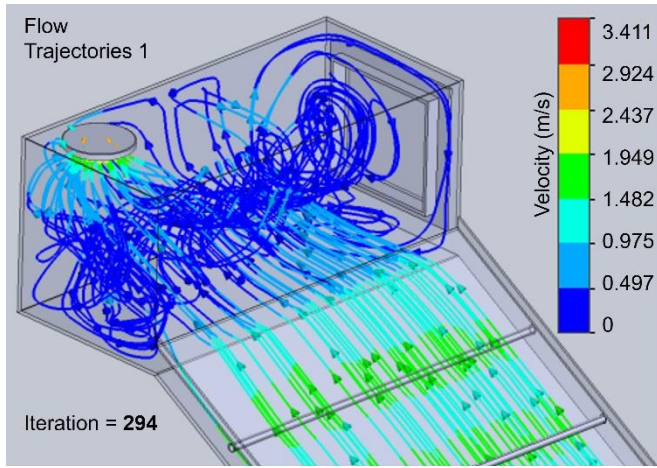


(b)

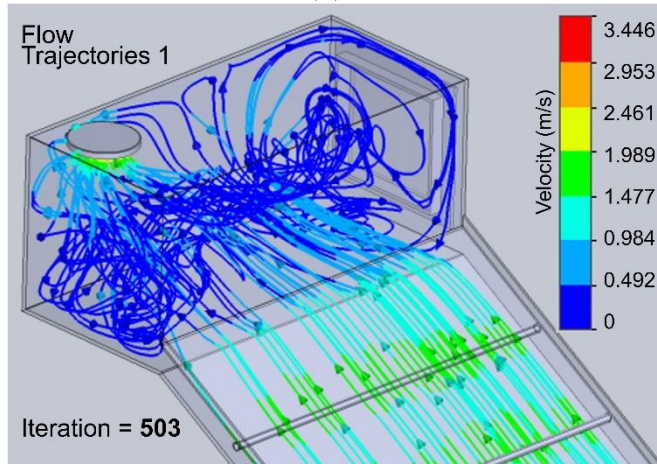


(c)

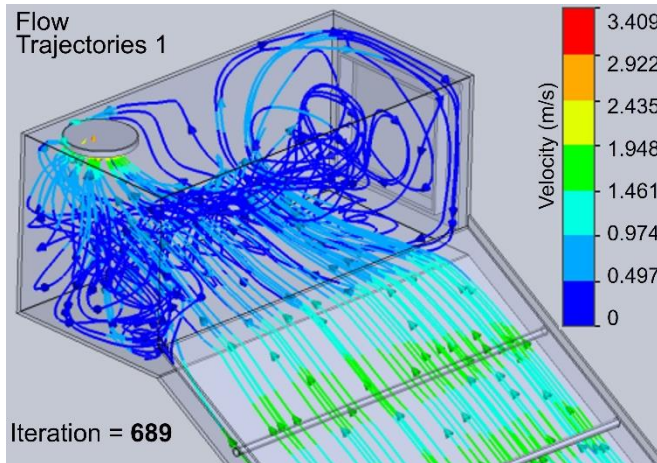
Figure 5. Air flow velocity contours (Top View) in (a) palmitic acid, (b) lauric acid, (c) paraffin wax.



(a)



(b)



(c)

Figure 6. Air flow velocity contours inside the chamber for (a) palmitic acid, (b) lauric acid (c) paraffin wax

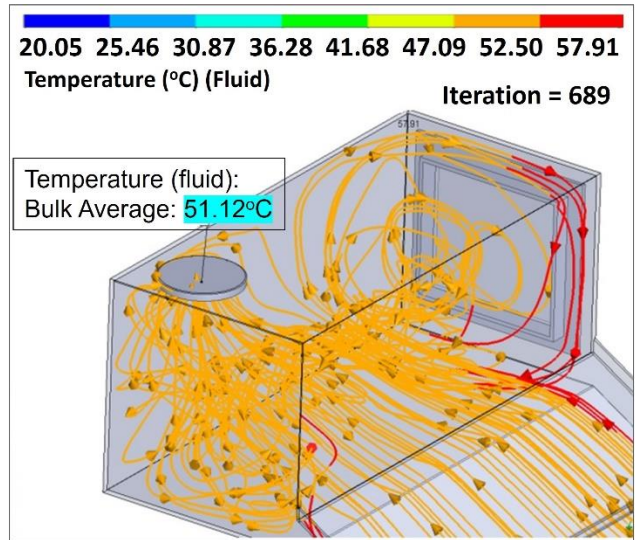
When paraffin wax, lauric acid, and palmitic acid were used, the dryer was 87%, 40.2%, and 12.4% more efficient than a traditional dryer.

Paraffin wax absorbs and transmits heat faster than lauric acid and palmitic acid.

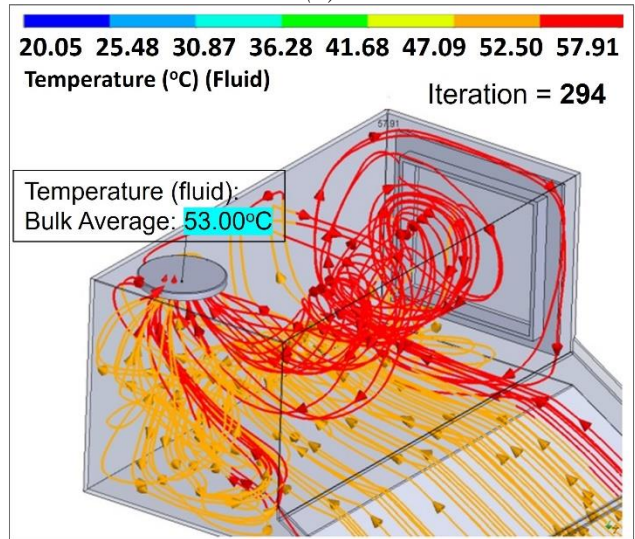
Hence, paraffin wax emerged as the best-performing phase change material for solar dryers as the energy storage system.

These research findings are helpful for researchers and industry personnel in designing effective heat storage systems to reduce heat loss from solar dryers and solar air heaters. In future, multi-objective optimization and thermo-

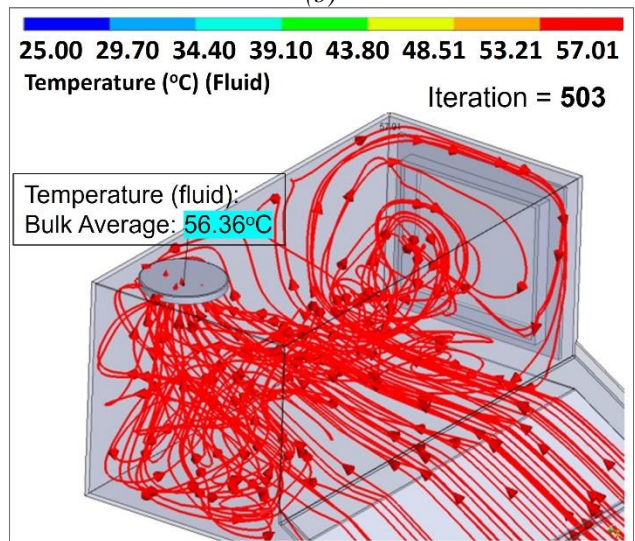
economic analysis will be required to estimate the precise quantity of PCM for further investigations.



(a)

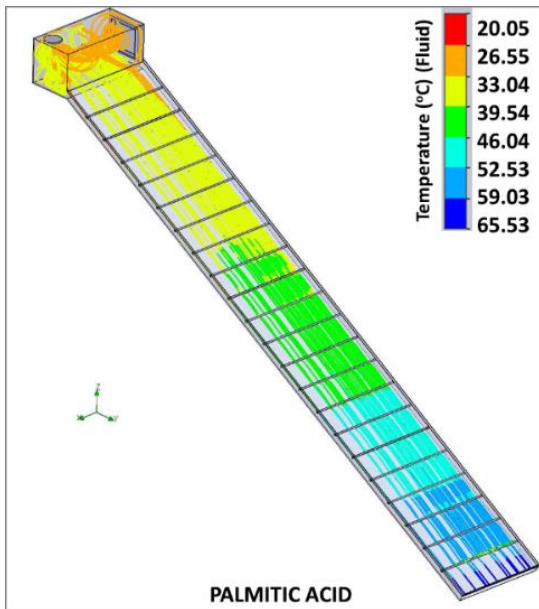


(b)

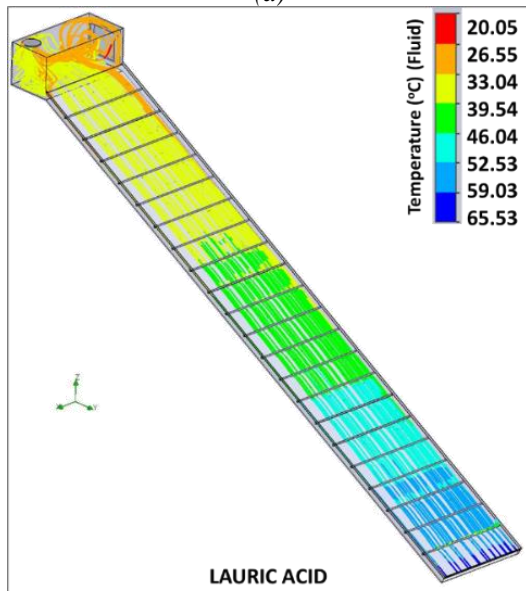


(c)

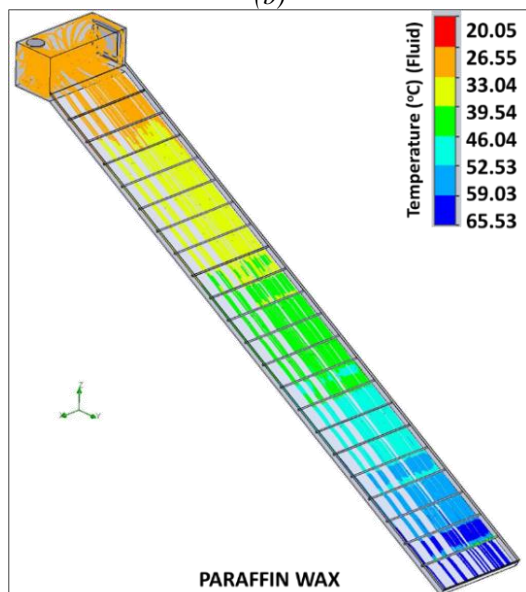
Figure 7. Temperature distribution of air at chambers for lauric acid, palmitic acid and paraffin wax respectively in (a) palmitic acid, (b) lauric acid, (c) paraffin wax.



(a)



(b)



(c)

Figure 8. Temperature distribution of air (top view) in (a) palmitic acid, (b) lauric acid (c) paraffin wax.

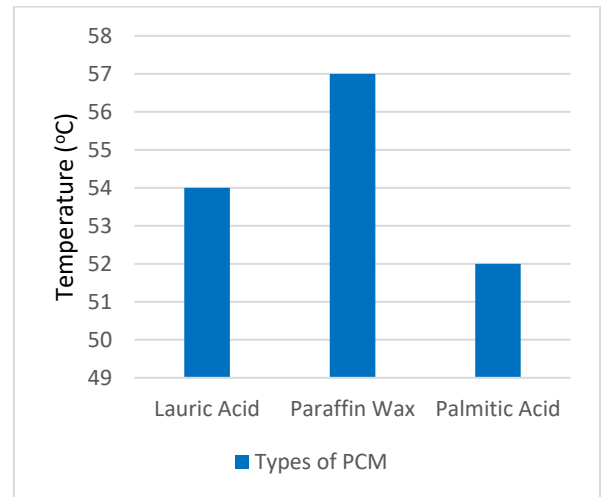


Figure 2. Air Temperature at the exhaust surface of the drying cabinet.

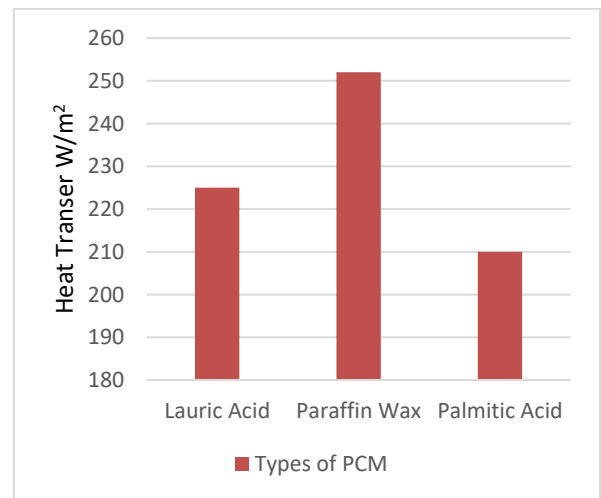


Figure 3. Heat transfer rate for PCMs.

Nomenclature

A	Surface area (m^2)
C	Specific heat capacity ($J/kg\ K$)
d	Thickness of copper plate (m)
h	Heat transfer coefficient ($W/m^2\ K$)
k	Thermal conductivity ($W/m\ K$)
m	Mass (kg)
Q	Heat transfer rate (W/m^2)
T	Temperature ($^{\circ}C$)
T_{cold}	Cold (fluid) temperature ($^{\circ}C$)
T_{hot}	Hot (surface) temperature ($^{\circ}C$)
σ	Stefan Boltzmann constant ($W/m^2\ K^4$)
ϵ	Emissivity

References:

- [1] C. L. Hii, S. V. Jangam, S. P. Ong, A. S. Mujumdar, "Solar drying: Fundamentals, applications and innovations," TPR Group Publication, vol. 1, no. 1, Singapore, 2012.
- [2] V. I. Umogbai, H. A. Iorter, "Design, construction and performance evaluation of a passive solar dryer for maize cobs," Afr J Food Sci Technol, vol. 5, no. 2, pp. 110-115, 2013.

- [3] C. Mamulkar, V. Katekar, "Performance Evaluation of Double Flow Solar Air Heater," in *Natl. Conf. Innov. Paradig. Eng. Technol.*, vol. 2, no. 3, pp. 5-6, 2012.
- [4] V. P. Katekar, M. Asif, S. S. Deshmukh, "Energy and Environmental Scenario of South Asia," in *Energy Environ. Secur. Dev. Ctries.*, 1st ed., Springer Nature Switzerland: Springer Nature Switzerland, vol. 3, no. 4, pp. 75-103, 2009.
- [5] V. P. Katekar, S. S. Deshmukh, A. Vasan, "Energy, drinking water and health nexus in India and its effects on environment and economy," *J. Water Clim Chang.*, vol. 10, no. 5, pp. 997-1022, 2021. doi: 10.2166/wcc.2020.340.
- [6] M. Durusoju, C. Goyal, I. Sheik, A. Dongre, L. Marbate, K. Rohit, et al., "Heat Transfer Enhancement Techniques for Solar Air Heater--A Review," *Int J Res Appl Sci Eng Technol*, vol. 4, no. 7, pp. 451-457, 2016.
- [7] V. P. Katekar, S. S. Deshmukh, "Energy-Drinking Water-Health Nexus in Developing Countries," in *Energy Environ. Secur. Dev. Countries, Adv. Sci. Technol. Secur. Appl.*, Springer, Cham., vol. 5, no. 2, pp. 411-445, 2021. doi: https://doi.org/10.1007/978-3-030-63654-8_17.
- [8] K. J. Khatod, V. P. Katekar, S. S. Deshmukh, "An evaluation for the optimal sensible heat storage material for maximizing solar still productivity: A state-of-the-art review," *J. Energy Storage*, vol. 11, no. 5, pp. 104622, 2022. doi: 10.1016/j.est.2022.104622.
- [9] V. P. Katekar, S. S. Deshmukh, "A review of the use of phase change materials on performance of solar stills," *J. Energy Storage*, vol. 30, no. 8, pp. 101398, 2020. doi: 10.1016/j.est.2020.101398.
- [10] N. Rajeshwari, A. Ramalingam, "Low-cost material used to construct effective box type solar dryer," *Arch Appl Sci Res*, vol. 4, no. 3, pp. 1476-1482, 2012.
- [11] G. Tiwari, V. K. Katiyar, V. Dwivedi, A. K. Katiyar, C. K. Pandey, "A comparative study of commonly used solar dryers in India," *Int J Current Eng Tech*, vol. 3, no. 2, pp. 1-6, 2013.
- [12] A. Madhlopa, S. A. Jones, J. D. Kalenga Saka, "A solar air heater with composite absorber systems for food dehydration," *J. Renewable Energy*, vol. 27, no. 1, pp. 27-30, 2002.
- [13] A. Brett, D. R. Cox, R. Simmons, G. Anstee, "A solar tunnel dryer for natural convection drying vegetables and other commodities in Cameroon," *J. Am. Med. Assoc.*, vol. 15, no. 4, pp. 31-35, 1996.
- [14] M. Isiaka, A. M. I. El-Okene, U. S. Muhammed, "Effect of selected factors on drying process of tomato in forced convection solar energy dryer," *Res. J. Appl. Sci. Eng. Technol.*, vol. 4, no. 7, pp. 1-4, 2012.
- [15] E. A. Arinze, S. Sokhansanj, G. J. Schoenau, F. G. Trauttmansdorff, "Experimental evaluation, simulation and optimization of a commercial heated-air batch hay drier," *J. Agric. Eng. Res.*, vol. 65, no. 3, pp. 301-314, 1996.
- [16] J. K. Afriyie, H. Rajakaruna, M. A. A. Nazha, F. K. Forson, "Simulation and optimization of the ventilation in a chimney-dependent solar crop dryer," *Sol. Energy.*, vol. 85, no. 7, pp. 1560-1573, 2011.
- [17] K. UmeshToshniwal, "A review paper on solar dryer," *Int. J. Eng. Res. Appl.*, vol. 3, no. 5, pp. 896-902, 2013.
- [18] B. M. A. Amer, M. A. Hossain, K. Gottschalk, "Design and performance evaluation of a new hybrid solar dryer for banana," *Energy Convers Manag*, vol. 51, no. 4, pp. 813-820, 2010.
- [19] Megha S. Sontakke, Prof. Sanjay P. Salve, "Solar drying technology: A review," *International Refereed Journal of Engineering and Science (IRJES)*, vol. 4, no. 8, pp. 29-35, 2015.
- [20] Umesh Toshniwal, S.R Karale, "A review paper on Solar dryer," *Int. J. Eng. Res. Appl.*, vol. 3, no. 5, pp. 896-902, 2013.

Research Article

Use the Thermodynamic State Equations to Analyze the Non-ideality of Gas Mixtures

¹N. Manuel , ²T.C.F.S. Major , ³S.M. Pedro , ^{4*}A.A.C. Barros 

^{1,2,3,4}Instituto Superior Politécnico de Tecnologias e Ciências (ISPTEC), Departamento de Engenharias e Tecnologias (DET) - Av. Luanda Sul, Rua Lateral Via S10, Talatona – Município de Belas, Luanda – Angola
E-mail: ^{4*}chivanga.barros@isptec.co.ao

Received 17 July 2023, Revised 8 September 2023, Accepted 27 September 2023

Abstract

The assessment of gas behavior in chemical engineering systems necessitates a profound understanding of thermodynamic principles that govern the interactions among the components within a given system. To this end, the deviation from ideality in a single gas or gas mixture is associated with the disparity between the actual behavior of the gas or gas mixture and the behavior anticipated by the ideal gas model. This study is aimed at scrutinizing the deviation from ideal behavior in a gas mixture composed of CH₄ and CO₂. The analysis employs the cubic equations of state: Van Der Waals, Soave-Redlich-Kwong, and generalized Virial equations, truncated to the third term. These equations are widely recognized for their utility in characterizing substance behavior under specific thermodynamic conditions. The investigation involves an evaluation of the mixture's behavior by assessing variations in the compressibility factor concerning pressure, volume, and pressure, using a thermodynamic calculator at 296.15 K and 15 bar. The findings of this study reveal the prevalence of attractive intermolecular forces at higher pressures and repulsive interactions at lower pressures. An analogous examination of the effect of altering the composition of CH₄ was undertaken using the Soave-Redlich-Kwong equation, which incorporates parameters allowing for an evaluation of the impact of molecule size and intermolecular interactions within the mixture. Furthermore, experimental data were employed to validate the results obtained in this study. Consequently, it can be inferred that these equations provide insight into the influence of pressure on molecular interaction forces, encompassing repulsive and attractive forces, which in turn can define the new volume of a real system. Thus, based on the corroboration established herein, these equations demonstrate a high degree of consistency and applicability, thereby expanding the realm of thermodynamic inquiry.

Keywords: Equation of state; real gas; ideal gas; compressibility factor.

1. Introduction

The instruction of Chemical Engineering is founded on the examination of predicting the thermodynamic properties of both pure substances and mixtures of components within a given phase, which play a crucial role in separation systems capable of achieving phase equilibrium. The majority of the properties under discussion here pertain to the behavior of pure components, disregarding molecular interaction forces among various constituents within a given mixture.

Furthermore, separation operations, notably distillation, absorption, and liquid-liquid extraction, entail mixing phases in equilibrium, with process performance heavily contingent on an understanding of the thermodynamic interactions between these phases. In such cases, employing equations of state for ideal gases (of the cubic, Virial-type, or generalized variety) is a common practice to enhance comprehension of the thermodynamic relationships at play. These equations establish a connection between the compressibility factor (Z) of either a pure substance or mixture and macroscopic, measurable parameters—Pressure, Volume, and Temperature, commonly referred to as PVT.

As posited by Muachia et al. [1], the thermodynamic relationships associated with PVT provide the means to assess the thermodynamic behavior of systems, as they offer

mechanisms for experimental determination that yield knowledge of various physical relationships linked to perturbations of each one. The authors contend that pressurized systems, characterized by elevated pressure levels, lead to a reduction in system volume, thereby intensifying molecular interactions and augmenting the attractive and repulsive forces between the system's molecules.

Consequently, an examination of thermodynamic systems should initially be grounded in an understanding of the behavior of an ideal gas—a theoretical gas characterized by the absence of intermolecular forces, where collisions are non-existent or negligible. These phenomena are rooted in the principles of conservation of momentum and kinetic energy [2].

To comprehensively determine the state of a system composed of a mixture of pure components, it is imperative to possess knowledge of the intensive variables, with particular emphasis on pressure (P), volume (V), and temperature (T), as well as an understanding of the composition of the constituent components of the mixture slated for separation. The relationships between these intensive properties remain constant within the system as long as the composition remains unaltered. These

relationships are predicated on the connections between volume, pressure, and work, as established by the principles of the first law of thermodynamics.

However, it is important to note that the behavior of most gas mixtures deviates from ideality, primarily due to the diverse interactions occurring among their constituent molecules. Moreover, variations in the shapes and sizes of the molecules within the mixture can also exert influence on the non-ideal behavior observed in gas-liquid mixtures.

In such cases, Mamedov et al. [3] posit that the ideal behavior of gases can be represented by Clapeyron's equation (Equation 1), which is grounded in the fundamental principles of physics and frequently applied to address a wide array of practical challenges, particularly in the domain of chemical engineering. Equation 1 establishes a direct correlation between its principal parameters, thus characterizing thermodynamic ideality.

$$PV = nRT \quad (1)$$

When analyzing the ideal gas equation (Equation 1), Costa [4] asserts that it describes a gas composed of numerous molecules represented as rigid spheres with a diameter 'd.' These molecules exhibit random or disordered motion, governed by Newton's Laws. The author further contends that these particles possess a non-zero mass 'm' while their individual volumes are negligible relative to the container's volume.

In this context, intermolecular interactions involving attraction and repulsion are considered negligible, except during collisions with each other and with the container walls. Within this analytical framework, it is evident that the internal energy of the involved molecules is associated with translational kinetic energy, which propagates in a linear fashion. Finally, according to Costa [4], the collisions among these molecules are perfectly elastic, as kinetic energy is not converted into other forms of energy.

In alignment with this analysis, Mahan & Myers [11] propose that the macroscopic properties of an ideal gas entail the independent motion of molecules, particularly evident when measurements of pressure, molar volume, and temperature deviate from the behavior described by the Clapeyron equation, which represents non-ideal behavior. Deviations from ideality are observed in pure gases and mixtures of unreacted gases. At room temperature and low pressures, deviations from ideality are nearly nonexistent. However, as pressure increases, gas behavior deviates from that of ideal gases.

Under known temperature and pressure conditions, a real or non-ideal gas comprises material particles engaged in chaotic motion, subject to forces of attraction and repulsion, with significant mass and volume [6].

To assess the PVT (Pressure-Volume-Temperature) behavior of real gases, cubic equations of state and generalized correlations are employed. These mathematical models account for intermolecular interactions and describe actual behavior across various pressure ranges. Notable among these equations of state are Van der Waals, Redlich-Kwong, and Soave-Redlich-Kwong, alongside the Pitzer and Virial correlations [7].

The fundamental premise underlying deviations from ideality is attributed to intermolecular forces, both attractive and repulsive, which exert a predominant influence on the PVT behavior of a given fluid (Equation 2).

$$P = P_R + P_A \quad (2)$$

In this scenario, repulsive forces contribute positively to pressure ($P_R > 0$), while attractive forces yield a negative contribution to pressure ($P_A < 0$). Consequently, the cubic Van der Waals (VDW) equation of state alters the ideal gas equation by incorporating the intermolecular forces present in a specific gas or gas mixture. Equation (3) characterizes this approach, taking into account intermolecular interactions, albeit with certain limitations. Nonetheless, Equation (3) proves valuable for depicting the behavior of real gases under conditions closely approximating those of ideal gases [8].

$$P = \frac{RT}{V-b} - \frac{a}{V^2} \quad (3)$$

Equation (2) can be applied to compute the thermodynamic parameters for gas mixing, which entails the utilization of the mixing parameters a_m and b_m , as detailed in Equation (3).

$$P = \frac{RT}{V-b_m} - \frac{a_m}{V^2} \quad (4)$$

Where P represents the pressure of the gas in atm, V is the molar volume of the gas in cm^3/mol , T is the temperature of the system in Kelvin (K), and R is the universal gas constant. Additionally, a_m and b_m are the Van der Waals constants, which are defined according to Equations 5, 6, 7, 8, and 9.

$$a = \frac{27(RT_c)^2}{64P_c} \quad (5)$$

$$b = \frac{RT_c}{8P_c} \quad (6)$$

$$a_m = \sum \sum y_i y_j a_{ij} \quad (7)$$

$$a_{ij} = (a_i a_j)^{0.5} \quad (8)$$

$$b_m = \sum y_i b_i \quad (9)$$

In the collision of gas molecules with any surface, the unopposed attractive forces of the molecules diminish the collision velocity. The additional term incorporated into the pressure equation serves to rectify the absence of counterbalancing attractive forces.

Conversely, the equation put forth in 1972 by Soave-Redlich-Kwong (SRK) represents one of the most extensively employed equations of state for elucidating the characteristics of both pure substances and gas mixtures (Equation 10). It is distinguished as an extension of the Van der Waals equation [6].

$$P = \frac{RT}{V-b} - \frac{a}{V^2 + Vb} \quad (10)$$

The utilization of Equation (10) is expanded to compute the thermodynamic properties of gas mixtures, encompassing the incorporation of mixing parameters a_m and b_m , as delineated by Equation (11).

$$P = \frac{RT}{V-b_m} - \frac{a_m}{V^2 + Vb_m} \quad (11)$$

In this context, P represents the gas pressure (in atm), V stands for the molar volume of the gas (in cm³/mol), T denotes the system's temperature (in K), while R signifies the universal gas constant. Additionally, a and b represent the substance-specific constants, and α serves as a temperature-dependent correction factor, in accordance with the descriptions provided in Equations (12), (13), (14), (15), and (16).

$$a_m = \alpha a_c \quad (12)$$

$$a_c = \frac{0,42748(RT_c)^2}{P_c} \quad (13)$$

$$\alpha = [1 + m(1 - T_r)^{0,5}]^2 \quad (14)$$

$$m = 0,048508 + 1,55171w - 0,15613w^2 \quad (15)$$

$$b = 0,008664 \frac{RT_c}{P_c} \quad (16)$$

For Van Wylen et al. [9], assessing the departure from gas ideality involves the computation of the compressibility factor. This thermodynamic property quantifies the deviation of real gas behavior from ideal gas behavior. It is defined as the ratio between the molar volumes of real and ideal gases under identical temperature and pressure conditions. A compressibility factor of 1 (one) indicates ideal gas behavior, while values different from 1(one) suggest non-ideal behavior.

Given the aforementioned complexity, numerous equations of state have been developed to study gas behavior. Prominent among these are the cubic equations, including Van Der Waals, Redlich-Kwong, and Soave-Redlich-Kwong, among others [10].

Notably, Pitzer's correlation stands out among various approaches. It expresses the compressibility factor (Z) as a function of temperature (Tr), reduced pressure (Pr), and the acentric factor (w) for each component.

The generalized Pitzer correlation serves as an empirical model that aids in comprehending molecular interaction forces, particularly in solutions where interactions occur between molecules of different sizes. Kenneth Pitzer introduced this correlation [10], which elucidates molecular or ionic interactions in solution using linear combinations of parameters in a Virial-type expansion of the excess Gibbs free energy.

Consequently, the virial-type equation with emphasis on the third coefficient is employed to calculate the compressibility factor, as defined in Equation (17).

$$Z = 1 + (B^0 + wB^1) \frac{P_r}{T_r} + (C^0 + wC^1) \frac{P_r^2}{T_r^2} \quad (17)$$

$$P_r = \frac{P}{P_c} \quad (18)$$

$$T_r = \frac{T}{T_c} \quad (19)$$

On the contrary, the generalized equation incorporates the acentric factor (w), a parameter inherent to the molecular structure of the gas, which exhibits a significant correlation with the system's pressure and temperature. This factor is also interconnected with the dimensions of the constituent molecules within the examined mixture [14]. All functions

herein are interdependent with the reduced pressure and temperature, as elucidated in Equations (20), (21), (22), and (23) [11].

$$B^0 = 0,083 - \frac{0,422}{T^{1,6}} \quad (20)$$

$$B^1 = 0,139 - \frac{0,172}{T^{4,2}} \quad (21)$$

$$C^0 = 0,01407 + \frac{0,02432}{T_r} - \frac{0,00313}{T^{10,5}} \quad (22)$$

$$C^1 = -0,02676 + \frac{0,05539}{T_r^{2,7}} - \frac{0,00242}{T^{10,5}} \quad (23)$$

Based on the provided theoretical framework, a thermodynamic assessment was conducted to analyze the behavior of the compressibility factor as a function of gas mixture pressure consisting of carbon dioxide (CO₂) and methane (CH₄). This investigation explored the influence of varying proportions of these gas components. The obtained results were evaluated within the context of attractive and repulsive forces under isothermal conditions, employing two distinct cubic equations of state and a generalized equation of state.

2. Procedure and Methodology

To carry out this study, a logical algorithm was developed for solving a sequence of equations essential for determining properties such as volume, compressibility factor, entropy, internal energy, enthalpy, Gibbs free energy, and Helmholtz free energy for a binary gas mixture. These calculations were performed under predefined conditions of temperature, composition, and pressure.

The algorithm incorporates a comprehensive database, facilitating the exploration of diverse gas mixtures with varying compositions and the assessment of concentration effects on the compressibility factor within a specified pressure range under isothermal conditions. Additionally, it permits an examination of the impacts of molecular size and attractive/repulsive forces on the behavior of the compressibility factor, irrespective of the equation of state or correlation utilized. Figure 1 illustrates the algorithm created.

For the implementation of this algorithm, a software program was developed using Microsoft Excel, creating a thermodynamic calculator with a user-friendly graphical interface. This interface enables adjustment of input parameters, evaluation of output conditions, and correlation of various types of equations of state, thereby enhancing comprehension of the parametric interactions involved in the evaluated cases.

The thermodynamic calculator investigated the cubic Van Der Waals equation, the Soave-Redlich-Kwong (SKW) equation of state and the generalized Virial-type equation truncated to its third term.

This exploration was conducted to assess the parametric attributes associated with each equation, elucidating the physical and molecular interactions within the system, and their impact on the mixing behavior.

2.1 Resolution Method

To derive the compressibility factor and molar volume using the cubic equations outlined in this study, the first step involved determining the constants 'a' and 'b' for each equation. These constants were calculated through the

correlations provided by Equations (5), (6), (13), and (16), respectively, as specified in the Van der Waals and Soave Redlich-Kwong equations.

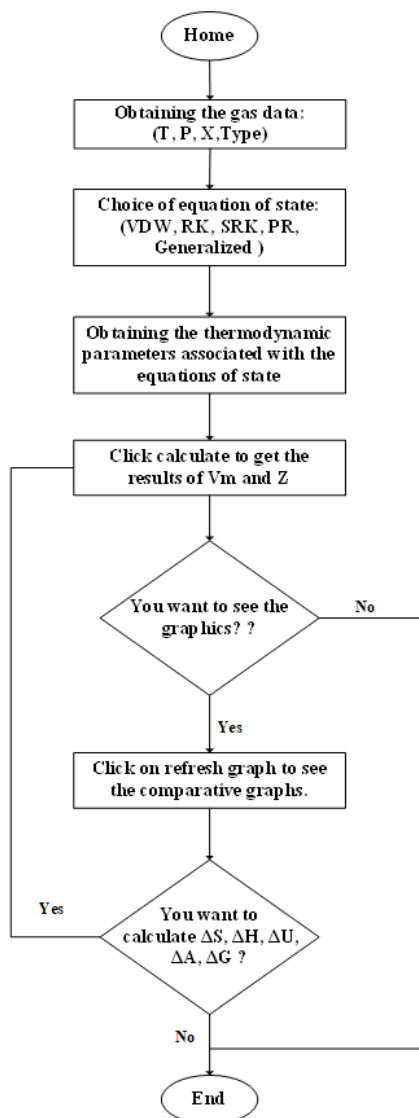


Figure 1. Proposed algorithm for determining the thermodynamic parameters of gas mixtures.

Subsequently, armed with the known operating conditions in terms of pressure (P) and temperature (T), the equations were restructured into a cubic equation format, with the molar volume (V_m) serving as the variable of interest.

Upon structuring the cubic equation, the Newton-Raphson method was employed to ascertain the mixture's volume using the Taylor series expansion. In this context, the maximum volume identified corresponds to the volume of the gas under examination. This value was employed in determining the compressibility factor (Z), as supported by Equation (24).

$$Z = \frac{P}{V_m RT} \quad (24)$$

Maxwell's relations were employed to compute the energy variation within the system. This process entailed utilizing the definitions stemming from the equations of the

first and second laws of thermodynamics. The outcomes obtained through these calculations provided valuable insights into the behavior of these parameters within the systems under investigation.

3. Results and Discussions

The thermodynamic calculator, developed in the context of this study, systematically investigates the parametric behavior of a mixture consisting of carbon dioxide (CO₂) and methane (CH₄) under the prescribed initial conditions, as detailed and specified in Table 1.

Table 1. CO₂ and CH₄ mixture conditions used in this article.

Components	Composition (%)	Temperature (K)	Pressure (Bar)
CO ₂	68	296.15	15
CH ₄	32		

The algorithm proposed (Figure 1) served as a foundation for the development of the Thermodynamic Calculator (Figure 2), which was utilized for data input and solution display for the specified problem. Under the operational conditions employed, the molar volumes and compressibility factors were determined under the prescribed conditions. Furthermore, the behavior of the compressibility factor was assessed over a predefined pressure range (0 to 1000 bar), utilizing the three aforementioned equations of state.

The acquired data exhibited notable similarity, yielding an average compressibility factor of 0.944 for the three equations, resulting in an average deviation of merely 0.5% from this computed average.

An analysis of the compressibility factor profile indicated analogous qualitative patterns: attractive forces were substantial up to 500 bar, with repulsive forces assuming greater significance beyond this pressure range. Conversely, when employing the cubic Van der Waals equation of state, attractive forces exhibited reduced significance, while repulsive forces became more pronounced. This discrepancy can be attributed to the absence of parameters related to molecular size in the Van der Waals equation.

In contrast, the Soave-Redlich-Kwong equation of state incorporates the acentric factor as a parameter, accounting for molecular sizes within the mixture. This leads to a diminished influence of both repulsive and attractive forces compared to the results obtained with the Van der Waals equation.

At lower pressures, molecules are generally distanced from one another in these scenarios, with negligible intermolecular forces at play, causing the fluid to behave akin to an ideal gas (Z=1). As pressure increases, molecules draw closer together, and attractive intermolecular forces dominate. Consequently, the gas's volume decreases more significantly than it would if no intermolecular attraction forces were present, resulting in Z<1.

Conversely, at very high pressures, molecules approach each other to an extent where repulsive forces become dominant, causing a more substantial increase in volume than expected in the absence of intermolecular repulsive forces, leading to Z > 1. While a value of Z=1 is attained at high pressures in all cases, it does not correspond to ideal gas behavior [9], [11], and [12].

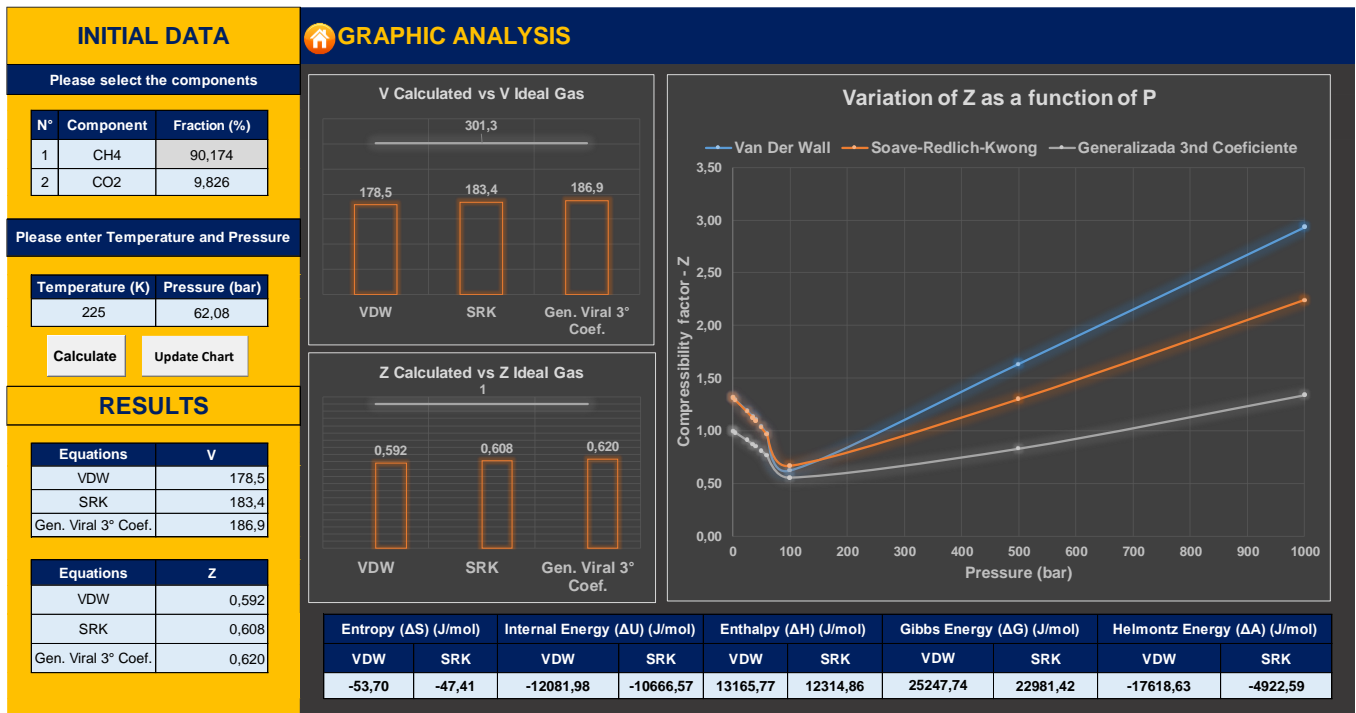


Figure 2. Thermodynamic calculator interface.

The examination of the results presented in Figure 2 and Table 1 unveils a level of molecular disarray characterized by the entropy change (ΔS). This observed molecular disarray emanates from the reduced operational pressures and temperatures taken into account under the assessed operating conditions. These factors significantly impact the stochastic movement of the molecules. A similar pattern is discerned when analyzing the changes in internal energy (ΔU) and Helmholtz free energy (ΔA), both of which exhibit negative values, as recorded in Table 2, acquired at 296.15 K and 15 bar.

Table 2. Thermodynamic energies evaluated in this paper.

Equation	Temperature (K)	Pressure (Bar)	ΔS (J/mol.K)	ΔU (J/mol)	ΔH (J/mol)	ΔG (J/mol)	ΔA (J/mol)
VDW	296.15	15.0	-4.81	-1432.64	1468.56	2901.2	-1545.81
SRK			-5.20	-1539.16	1583.21	3122.37	-1418.72

The analysis of enthalpy (ΔH) and Gibbs Free Energy (ΔG), which represent the energies associated with the system, provides insights into non-spontaneous processes. This analysis supports the molecular behavior of the system, which is influenced by both attractive and repulsive forces between the system molecules. It elucidates the disparities in values between the Van der Waals (VDW) and Soave-Redlich-Kwong (SRK) equations.

Numerical results derived from these equations reveal a deviation of approximately 7%. This deviation is noticeable when comparing data from these two equations, with the cubic Soave-Redlich-Kwong equation demonstrating greater accuracy. This enhanced accuracy is attributed to its consideration of the molecular size as a dominant factor in dictating the thermodynamic behavior of gas mixtures.

3.1. Non-ideality Analysis

The deviation from gas ideality can be observed through the analysis of the compressibility factor (Z), which is a dimensionless measure describing the behavior of a gas concerning its pressure and volume. According to Elechi et al. [9], when the compressibility factor (Z) deviates from the

ideal gas standard, the gas or gas mixture exhibits non-ideal behavior.

Figure 3 illustrates the behavior of the compressibility factor (Z) as a function of pressure (P) for the cubic Van Der Waals, Soave-Redlich-Kwong, and generalized Virial-type truncated equations of state at a temperature of 296.15 K.

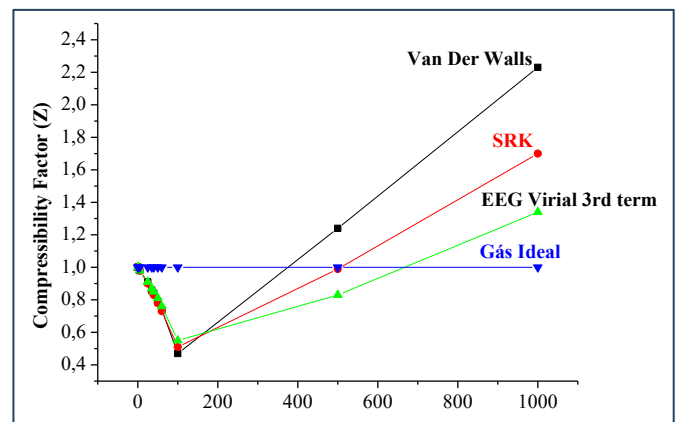


Figure 3. Behavior of the compressibility factor as a function of pressure mixture of 32% CH_4 and 68% CO_2 .

The operational conditions employed for the Z calculations (Figure 3) are elucidated within Table 1. The scrutiny of Figure 3 unveils that when subjected to elevated pressures, the methane (CH_4) and carbon dioxide (CO_2) gas amalgamation demonstrates non-ideal gas behavior, characterized by the preeminence of repulsive intermolecular forces.

Conversely, under reduced pressures, attractive forces hold sway, marked by their heightened efficacy in the intermolecular collisions between CH_4 and CO_2 molecules, manifesting as a counterintuitive phenomenon at lower pressures.

Furthermore, an examination was conducted to assess the pressure-volume relationship of the studied gas mixture. This analysis indicated that within the high-pressure regime, spanning from 600 to 1000 bar, negligible fluctuations in

volume were observed with incremental pressure increments within the stipulated range. Conversely, a conspicuous volume fluctuation was noted within the pressure range of 0 to 300 bar. This phenomenon is attributable to the increased intermolecular spacing induced by compression, leading to pronounced volume alterations within the system. Notably, for all three equations of state examined, a confluence in volume behavior as a function of system pressure was ascertained across the considered pressure spectrum.

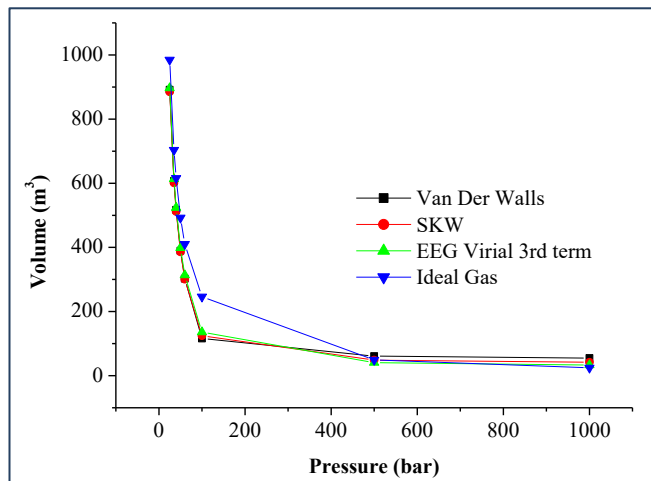


Figure 4. Volume profile as a function of pressure for a mixture of 32% CH₄ and 68% CO₂.

Nevertheless, the ideal gas model exhibited more pronounced deviations within the pressure range of 100 to 400 bar, possibly owing to its inherent gas properties.

Figure 4 presents an analysis of gas mixing, entailing the blending of two gases comprising 32% and 68% fractions of CH₄ and CO₂, respectively. These studies were conducted to gain deeper insights into the mixing phenomena across various compositional ratios.

3.2 Influence of Composition on the Compressibility Factor

For the analysis of the influence of the gas mixture composition, CH₄ and CO₂, data from the Soave-Redlich-Kwong equation were utilized due to the qualitative similarity in the behavior of the three equations studied and the incorporation of the acentric factor into this correlation.

Thus, the effects of mixture concentration were investigated, with an examination of systems containing pure CH₄ and the progressive increment of CO₂, up to maximum CO₂ purity. This analysis was conducted under isothermal conditions at 296.15K, as indicated in Figure 5.

In general, it is observed that the compressibility factor of pure CH₄ is higher than that of pure CO₂, indicating a greater prevalence of attractive forces in CO₂ gas compared to CH₄ gas.

Conversely, repulsion forces become more significant when analyzing the behavior of CH₄ gas, predominating above 300 bars. This phenomenon is also noted for pure CO₂ gas at pressures exceeding 580 bars.

The 25% CH₄ and 75% CO₂ mixture exhibits a pronounced influence of attractive forces, surpassing the behavior observed when analyzing the compressibility factor of the individual components, prevailing up to a pressure of 530 bars.

Beyond this threshold, it is observed that this parameter behaves more prominently than that of pure CO₂ but less so

than pure CH₄. The other curves obtained from this evaluation demonstrate mixing effects based on the proportions established in each analysis of this process.

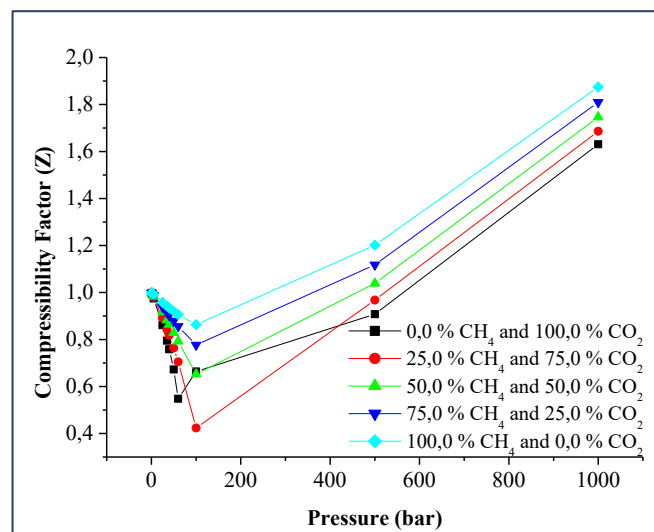


Figure 5. Behavior of Z as a function of pressure for the mixture of CH₄ and CO₂.

The evaluation depicted in Figure 5 illustrates the behavior of an ideal gas mixture comprising CO₂ and CH₄ at varying proportions as the system pressures approach zero. As pressure increases, the effects of attractive forces become increasingly apparent, irrespective of the gas fractions' composition within the mixture.

Conversely, when pressures exceed 400 bar, the influence of repulsive forces becomes dominant across all compositions considered and persists throughout the entire range of operating conditions investigated in this study. For all cases analyzed, a transition point is discernible, marking the shift from attraction to repulsion phenomena. This transition point is characterized by a calculated compressibility factor equal to 1 (one), indicating a departure from the conditions of an ideal gas.

3.3 Validation of State Equations

The consistency of the data derived from the state equations employed in this study was validated through a comparison with experimental data obtained by Hwang et al. [13]. This comparison was conducted for two distinct cases, with a focus on the specific weight of the gas mixture. In the first case, the data was extracted from experiments conducted at a temperature of 225K, utilizing a mixture composed of 9.826% CO₂ and 90.174% methane, respectively. In the second case, experiments were performed under different thermal conditions, specifically at 350K, while maintaining the same composition ratios for the components.

The results for the first case are presented in Figure 6, where a noteworthy approximation between the experimental data and the Soave-Redlich-Kwong (SRK) model data is observed, with an average deviation of 2.27%.

On the other hand, the comparison between experimental data and Van der Waals data in these analyses exhibited an average deviation of 11.59%. In this scenario, smaller deviations in specific mass values were observed for pressures exceeding 100 bar.

Regarding the data derived from the generalized Virial-type equation truncated to its third term (EEG), within the pressure range assessed in this study, the deviation was

10.68% when comparing experimental data with GEE-derived data.

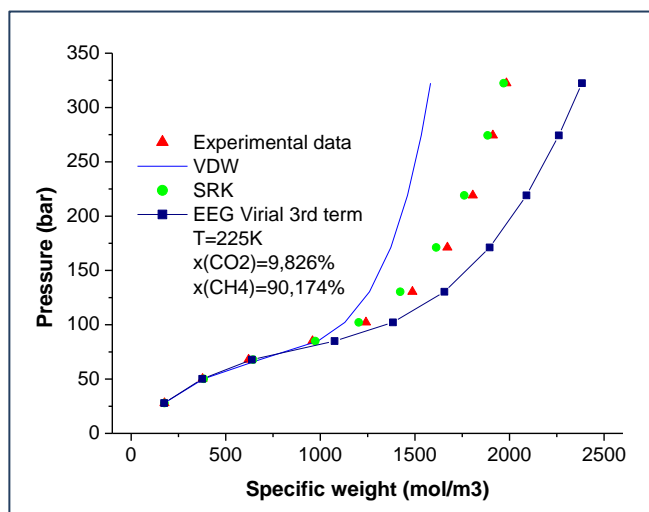


Figure 6. Behavior of specific weight as a function of pressure for the mixture of CH_4 and CO_2 with 225 K.

In the second case, when comparing experimental data with state equation data at 350 K, a significant approximation was observed for all cases evaluated, as depicted in Figure 7. Nevertheless, the Van der Waals equation displayed an average deviation of 3.69%, whereas the Soave-Redlich-Kwong (SRK) and EEG exhibited deviations of 1.78% and 1.74%, respectively.

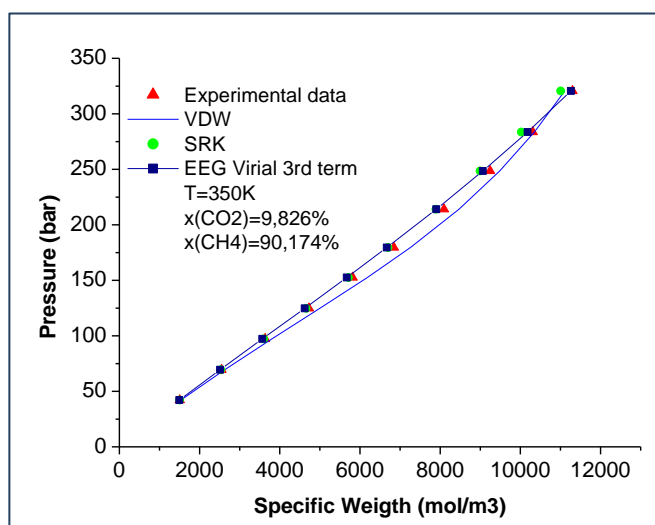


Figure 7. Behavior of specific weight as a function of pressure for the mixture of CH_4 and CO_2 with 350 K.

The results presented in Figure 7 demonstrate a high degree of consistency when utilizing state equations to evaluate the thermodynamic profiles of gas mixtures, particularly when employing the SRK equation.

On the other hand, both the EEG and SRK equations rely on the acentric factor, a parameter associated with molecular size, as a crucial determinant for assessing the thermodynamic characteristics of gas mixtures.

4. Conclusions

Based on the results obtained in this study, the following conclusions can be drawn:

a) Real gases exhibit ideal gas behavior as system pressures approach zero.

- b) The influence of gas mixtures can be assessed by examining the behavior of compressibility factors. These factors depend on the fractions of each component in the mixture and the specific type of gas involved in the process.
- c) The equations of state analyzed in this study demonstrate compatibility with the analysis of gas mixing behavior. They account for both attractive and repulsive forces between constituent molecules within the system and consider the size of molecules as predominant factors influencing the thermodynamic behavior of gases.
- d) The behavior of gases can be characterized by examining the relationship between pressure and volume. Under high pressures, significant changes in system volume are not observed due to the strong interaction between system molecules, resulting in their close proximity and alterations in the system's physical state.
- e) Experimental data corroborate the equations studied in this work, with the best consistency observed when employing the SRK equation within the evaluated temperature and pressure range.
- f) At low pressures, the impact of pressure on the system's volume becomes significant, primarily due to the increased distance between constituent molecules within the system under investigation.

Nomenclature:

P: pressure of the gas (bar);
V: molar volume of the gas (cm^3/mol);
 V_m : molar volume of the gas mixture (cm^3/mol);
T: temperature of the system (K);
R: universal gas constant;
 a_m and b_m : mixture constants of state equations;
 P_A and P_B : attractive and repulsive pressure;
SRK: Soave-Redlich-Kwong cubic equation;
VDW: Van Der Waals cubic equation;
 P_C : critical pressure (Bar);
 T_C : critical temperature (Kelvin);
a and b: pure constants of state equations;
W: acentric factor;
Z: compressibility factor;
 T_r : reduced temperature;
PVT: pressure, volume and temperature;
 ΔS : variation of entropy (Joule/(mol K));
 ΔU : variation of internal energy (Joule/mol);
 ΔA : variation of Helmholtz free energy (Joule/mol);
 ΔH : variation of enthalpy (Joule/mol);
 ΔG : variation of Gibbs Free Energy (Joule/mol).

Acknowledgements:

The authors of this paper express sincere appreciation for the collaboration of the Post-Graduation Coordination and the Undergraduate Coordination of the Chemical Engineering Program at ISPTEC for their unwavering dedication and support in the development of this research.

References:

- [1] A. Muachia, A. Manuel, J. Marques, M. Lemos and A. A. C. Barros. Uso das equações generalizadas de Pitzer para Avaliação termodinâmica de gases. *SAPIENTIAE: Revista de Ciências Sociais, Humanas e Engenharias*. vol. 1, pp. 35-43, 2020.
- [2] V. U. Elechi, S. S. Ikiensikimama and I. I. Azubuike. A

- correlation for estimating gas compressibility factor in the Niger Delta. *Festschrift for J. A. Ajiienka*, pp. 137–148, 2015.
- [3] B. A. Mamedov, E. Somuncu and I. M. Askerov. Theoretical assessment of compressibility factor of gases by using second virial coefficient. *Zeitschrift für Naturforschung*. Vol. 73, n° 2, pp. 121-125, 2018. doi:10.1515/zna-2017-0225.
- [4] Costa, M. A. (2006). *Análise do desvio de comportamento entre gás real e gás ideal*. (Master Dissertation), Centro Federal de Educação Tecnológica. Rio Grande do Norte, Brazil.
- [5] B. H. Mahan and R. J. Myers. *University Chemistry*. California, USA. University of California, 1076 pages, 2008.
- [6] P. Colonna, N. R. Nannan, A. A. Guardone and T. P. Van der Stelt. On the computation of the fundamental derivative of gas dynamics using equations of state. *Fluid Phase Equilibria*, vol. 286, n° 43, 2009.
- [7] D. Rowland and P. M. May. Comparison of the Pitzer and Hückel equation frameworks for activity coefficients, osmotic coefficients and apparent molar relative enthalpies, heat capacities and volumes of binary aqueous strong electrolyte solutions at 25°C. *J. Chem. Eng. Data*, 2015. doi:10.1021/acs.jced.5b00161.
- [8] Y. Adacid, I. Fijihara, M. Takamiya and K. Nakanishi. Generalized equation of state for Lennard-Jones fluids—
I. Pure fluids and simple mixtures. *Fluid Phase Equilibria Journal*. Vol. 39. pp. 1-38, 1988. doi:10.1016/0378-3812 (88)80001-3.
- [9] G. Van Wylen, R. Sonntag and C. Borgnakke, *Fundamentos da Termodinâmica Clássica*. 4ª edição. São Paulo, Brazil. Editora Edgard Blücher Ltda, 2003.
- [10] M. C. Simões, K. J. Hughes, D. B. Ingham, Lin Ma, and M. Pourkashanian. Estimation of the Pitzer parameters for 1–1, 2–1, 3–1, 4–1, and 2–2 single electrolytes at 25°C. *J. Chem. Eng. Data*. Vol. 61, n° 7, pp 2536 - 2554, 2016. doi: 10.1021/acs.jced.6b00236.
- [11] J. M. Smith, H. C. Van Ness and M. M. Abbott, *Introduction to chemical engineering thermodynamics*. 7th Edition. Rio de Janeiro, Brazil. LTC Editor, 2007.
- [12] P. M. S. Kalvelage, A. A. Albuquerque, A. A. C. Barros and S. L. Bertoli. (Vapor + Liquid) Equilibrium for Mixtures Ethanol + Biodiesel from Soybean Oil and Frying Oil. *International Journal of Thermodynamic*, vol. 20, pp. 159-164, 2017.
- [13] C. Hwang, G. A. Iglesias-Silva, J. C. Holste, K. R. Hall, B. E. Gammon and K. N. Marsh. Densities of carbon dioxide + methane mixtures from 225 K to 350 K at pressures up to 35 Mpa. *J. Chem. Eng. Data*, vol. 42, n° 5, pp. 897–899, September 1997, doi: 10.1021/je970042b.
- [14] M. S. Russel. *The Chemistry of Fireworks*. 2nd Edition. London, UK. Royal Society of Chemistry, 2009.

Research Article

Pressure Effect on Thermodynamic Quantities for the Solid-Liquid Phase Transition in n-tridecane, n-hexadecane and n-octadecane

¹O. Tari^{ORCID}, ^{2*}H. Yurtseven^{ORCID}

¹ Department of Electrical and Electronics Engineering, Istanbul Arel University, 34537 Büyükçekmece, Istanbul-TURKEY

² Department of Computer Engineering, Baskent University, 06790 Ankara – TURKEY
E-mail: ^{2*}hamit@metu.edu.tr

Received 4 August 2023, Revised 11 October 2023, Accepted 23 October 2023

Abstract

The pressure effect is investigated regarding the solid – liquid equilibria (SLE) in n-alkanes. Using the Landau phenomenological model, the pressure dependences of the thermodynamic functions are predicted and the phase diagrams are constructed for the solid – liquid transitions in the binary mixtures of n-alkanes. The experimental data from the literature are used for the phase diagrams in the mixtures.

Our fits for the phase diagrams are reasonably good. Regarding the cubic dependence of the concentration ($T - X$, $P - X$) and the linear dependence of the pressure ($P - T$) on the temperature, our results show that the n-tridecane is distinguished from the other mixtures due to its lowest freezing temperature ($T_1 = 291.08$ K) and correspondingly higher concentration ($x_1 = 0.1982$). It is found that the divergence behaviour of the heat capacity (C) with the critical exponent $1/2$ from the extended mean field model is in particular more apparent at the room temperature (293.15 K) at various pressures for the solid – liquid transition. This is accompanied with the pressure dependences of the order parameter, susceptibility, entropy and enthalpy for those mixtures as studied here.

Keywords: Phase diagrams; thermodynamic quantities; Landau model; n-tridecane; n-hexadecane; n-octadecane.

1. Introduction

Normal alkanes (n-alkanes) and their mixtures have been studied extensively over the years. In particular, studies on the phase boundary between the homogenous liquid phase and the two-phase liquid – solid phase domain, have been reported [1, 2]. Also, their specific rotator phases and intricate phase transition behavior have been the subject of various studies [3]. A number of studies [4-7] have been devoted to describe the structure and the phase transitions of the rotator phases, as indicated previously [3]. Small linear alkanes and their cyclic counterparts have been examined by molecular dynamic simulations and, thermodynamic, structural and dynamic behavior of liquids have been studied [8]. Among various mixtures of n-alkanes, confined crystallization behaviours of binary even-even normal alkane (n-alkane) mixtures of n-octadecane (n-C₁₈H₃₈) and n-eicosane (n-C₂₀H₄₂) have also been studied [9]. Melting curves of pure heavy paraffins were measured in earlier studies [10-13]. However, the pressure effect on the solid-liquid equilibria of complex mixtures of long-chain alkanes has not been investigated in those earlier studies. Later, a set of measurements were carried out on tridecane for the pressures up to 100 MPa in several synthetic mixtures, n-paraffins, ranging from n-C₁₃ to n-C₂₄ with various number of components [14]. The influence of pressure on the rotator phases was also studied within the Landau mean field theory [3]. Experimental phase diagram of the alkane system, namely, dodecane-tridecane was evaluated to study phase

change materials (PCMs) for freezing applications [13]. Also, experimental measurements and thermodynamic modeling for the binary mixtures of n-C₁₁H₂₄ have been carried out [15].

The pressure dependence of both the lattice distortion and the order of the rotator transitions has been discussed within the Landau theory in some details [16]. Also, rotator phases of n-heptane have been studied by Raman scattering and X-ray diffraction under high pressures [17]. For such a system, a liquid to solid transition has been predicted by the high pressure molecular dynamic (MD) simulations [18]. Rotator phases in alkane systems regarding bulk, surface layers and micro/nano confinements have been reviewed [19]. Experimentally, $T - X$ data at various pressures for binary mixtures of $(1 - x)n - C_{14} + xn - C_{16}$ (tetradecane + hexadecane) have been obtained [20, 21]. The temperature – dependent Raman spectra have been obtained for tetradecane, pentadecane and hexadecane [22]. $T - X$ phase diagram and the thermodynamic quantities were also calculated for this binary mixture [23-26] and for the n-tridecane [27] close to the liquid - solid phase transition using Landau phenomenological model in our recent studies.

Heat capacities of n-heneicosane and n-decosane have been measured and the thermodynamic properties such as entropy and enthalpy were calculated [28]. Also, by means of the molecular dynamic simulations, solid – liquid and solid – solid phase transitions in alkanes have been studied [29]. Regarding the heat capacity of the rotator phases of

alkanes, effect of silica nanoparticles has been studied theoretically by combining Flory-Huggins free energy (isotropic mixing) and Landau free energy [30]. Also, rotator phases in hexadecane have been studied experimentally [31].

Regarding the phase diagrams of binary mixtures of n-alkanes at high pressures, $T - X$ and $P - X$ (at constant temperatures) phase diagrams for n-tridecane + n-hexane were obtained from the experimental measurements [32]. Also, $T - X$ phase diagrams of n-alkane+cyclohexane where n-alkanes are n-hexadecane, n-octadecane and n-eicosane, were obtained at 300 MPa experimentally and the (solid + liquid) equilibria (SLE) of those n-alkanes were modelled [32]. The pressure effect on the physical and chemical properties of n-alkanes, has not been studied fully whereas the temperature effect on those properties was studied in a large scale as given in the literature. Mainly, the experimental measurements such as on tridecane up to 100 MPa [14] and the phase diagrams of n-alkanes [32], have been reported, as stated above. Theoretically, studies regarding the pressure effect on the phase diagrams and also on the thermodynamic functions, are relatively limited, as reported in the literature. Using the Landau mean field theory, in particular, the influence of the pressure has been studied for the rotator phases in n-alkanes [3, 16], as also stated above. From this point of view, the experimental measurements for the phase diagrams and for the thermodynamic properties at various pressures, require the theoretical analysis using some models. This present study by using the Landau phenomenological model, aims to fulfill this gap to describe the pressure effect on the thermodynamic properties for the solid – liquid equilibria in the binary mixtures (n-tridecane, n-hexadecane and n-octadecane). In order to describe the solid – liquid equilibria in n-alkanes, the thermodynamic properties have been studied mostly at various temperatures, as reported in the literature. Regarding our previous studies, $T - X$ phase diagram and also under high pressure for tetradecane + hexadecane [23, 26], $T - n$ (number of carbons) phase diagram of n-alkanes [24], and for n-tridecane [27] have been reported, as mentioned above. Additionally, the thermodynamic quantities have been calculated as a function of temperature [23, 26, 27] using Landau phenomenological model. However, the effect of the pressure on the transition mechanism for the solid – liquid equilibria, as studied for the phase diagrams of n-alkanes in our previous publications [25, 27], should also be studied for the thermodynamic quantities in those binary mixtures. From this point of view, the present study differs from the already published works in the sense that it uses the Landau phenomenological model and also it differs from our previous works [23-27] since in this study, thermodynamic functions are calculated as a function of pressure for the binary mixtures studied.

In this study, the $T - X$ phase diagrams (n-alkanes + n-cyclohexane) at 300 MPa, $P - X$ phase diagrams (n-alkanes + n-hexane) at constant temperatures and $P - T$ phase diagrams (n-alkanes + n-hexane) at constant concentrations (mole fractions) were calculated using the experimental data [32]. For this calculation, the phase line equations which were extracted from the free energy, are fitted to the experimental data [32]. As an original work, the $T - X$ phase diagram is represented by a single polynomial curve for n-hexadecane, n-octadecane and n-eicosane, whereas for n-tridecane the $T - X$ relation is obtained as linear from the Landau phenomenological model.

It has been shown in our previous study [26] that the extended mean field model can describe adequately the critical behavior of the heat capacity C and the other thermodynamic quantities as a function of temperature for the solid – liquid transition in the tetradecane + hexadecane. As an original study, the present paper aims to describe the solid – liquid equilibria in the binary mixtures of n-tridecane, n-hexadecane and n-octadecane by calculating the pressure dependence of the heat capacity C and also to predict the order parameter, susceptibility, entropy and enthalpy as a function of pressure at constant temperature by means of the extended mean field model. So that the pressure dependences of the order parameter, susceptibility and the thermodynamic quantities such as heat capacity, entropy and enthalpy were predicted for the solid-liquid transitions in these binary mixtures studied. Our motivation in the present study is to describe the liquid-solid equilibria and to investigate the phase change mechanism of the materials consisting of n-alkanes mixtures.

The present work illustrates the possibility of describing theoretically temperature – concentration – pressure phase diagrams and the pressure – induced phase changes in n-alkanes. This would lead to the fundamental understanding of the structural, physical and chemical properties of n-alkane molecules.

2. Theory

The pressure effect on the solid – liquid transition in n-alkanes can be investigated by the Landau mean field theory. Since this theory is applicable to the experimental measurements, by analyzing the observed data for the phase diagrams and the thermodynamic quantities, the first order solid – liquid equilibria (SLE) can be studied. This is done by expanding the free energy in terms of the order parameter. By obtaining the phase line equation from the free energy, the $T - X$, $P - X$ and $P - T$ phase diagrams can be constructed for n-alkanes on the basis of the experimental data. By means of the phase diagrams, the pressure dependence of the thermodynamic quantities can be predicted close to the solid – liquid transition in those mixtures. In this study, the pressure effect, in particular, on the mixtures of n-alkanes (1) + n-hexane (2), where n-alkanes (1) are n-tridecane (1), n-hexadecane (1) and n – octadecane (1) is investigated using the experimental data [32].

Various forms of the free energy in terms of the order parameters have been given in the literature. Thermodynamic model for a Landau model for the melting transition has been given [33]. The extended mean field model [34] has been introduced, mainly for the liquid crystals [35]. The coupled order parameters in the free energy expansion have been studied within the Landau phenomenological model [3, 16, 36, 37]. The free energy expansion with the coupled order parameters describing the solid – liquid transition in n-alkanes have been given in our recent studies [23 - 27]. In particular, the form of the free energy as given by the extended mean field theory [34], has been used in this study for the free energy of the solid phase (F_s) for the solid – liquid equilibria in terms of the order parameter η as

$$F_s = a_2\eta^2 + a_4\eta^4 + a_6\eta^6 \quad (1)$$

where the coefficients are assumed to depend on the temperature, pressure and concentration, in general. For the

solid – liquid equilibria, we have the first order condition that [38]

$$F_s = F_L = 0 \quad (2)$$

by considering the fact that in the liquid phase there is no ordering ($F_L = 0$). For the SLE, the coefficients are $a_2 > 0$, $a_4 < 0$ and $a_6 > 0$ for the first order transition as defined by the Landau mean field theory. Minimizing the free energy with respect to the order parameter ($\partial F_s / \partial \eta = 0$) as performed in our earlier studies [23 - 27], gives

$$a_2 + 2a_4\eta^2 + 3a_6\eta^4 = 0 \quad (3)$$

Using the first order condition (Eq. (2)), the order parameter can be written as

$$\eta^2 = -a_4/2a_6 = a_2/4a_4 \quad (4)$$

as also obtained previously [23, 26]. Substituting Eq. (4) into Eq. (1) and using Eq. (2), the phase line equation is obtained as

$$a_2a_6 = -2a_4^2 \quad (5)$$

for the SLE of the mixtures (n-alkanes) [23, 25, 26].

Thermodynamic quantities can also be calculated as a function of pressure for the SLE of the n-alkanes. As the order parameter η (Eq. (4)) was obtained, the inverse susceptibility using the definition

$$\chi_\eta^{-1} = \partial^2 F_s / \partial \eta^2 \quad (6)$$

can be predicted from the free energy F_s (Eq. (1)) as

$$F = a_2\psi^2 + a_3\psi^3 + a_4\psi^4 \quad (7)$$

similar to the calculation of χ_η^{-1} [23, 26].

For the thermodynamic quantities such as the heat capacity (C), entropy (S) and the enthalpy (H), the extended mean field model [34] is employed as applied to predict the heat capacity of the smectic A – smectic C (AC) transition in liquid crystals [35]. According to this model, the temperature dependence of the heat capacity is given by [35]

$$C = C_o T (T_1 - T)^{-1/2} \quad (8)$$

where T_1 denotes the melting temperature and C_o is a constant for the SLE in n-alkanes. This gives rise to the entropy difference $\Delta S = S - S_o$ from the definition $C/T = \partial S / \partial T$ as

$$\Delta S = \partial F / \partial T = -2C_o (T_1 - T)^{1/2} \quad (9)$$

where S_o is the entropy at the melting temperature ($T = T_1$). The enthalpy difference $\Delta H = H - H_o$ can also be obtained from the definition $C = \partial H / \partial T$ as

$$\Delta H = -C_o T (T_1 - T)^{1/2} \quad (10)$$

Similar calculation of the entropy (Eq. (9)) and the enthalpy (Eq. (10)) has been performed in our recent studies [23, 26]. In the derivation of Eq. (10), the $(T_1 - T)^{3/2}$ term is neglected as compared to the $(T_1 - T)^{1/2}$ term which is

dominant for the critical behavior of the enthalpy close to the solid – liquid transition in n-alkanes.

On the basis of the extended mean field model [35], the temperature dependence of the order parameter ψ (or η) can be obtained from the heat capacity as

$$\psi^2 = \int_T^{T_1} (C/T) dT \quad (11)$$

or by means of Eq. (8), ψ can be expressed as

$$\psi = \psi_0 (T_1 - T)^\phi \quad (12)$$

with the critical exponent $\phi = 1/4$ and the amplitude $\psi_0 = (2C_o)^{1/2}$.

3. Calculations and Results

The temperature, pressure and the concentration dependences of the phase line equation and the thermodynamic quantities studied, can be obtained by means of those dependences of the coefficients a_2 , a_4 and a_6 (Eq. (1)). By assuming that

$$a_2 = a_{20}(T - T_1) + a_{21}(P - P_1) \quad (13)$$

and

$$a_4 = a_{40} + a_{41}(x - x_1) + a_{42}(x - x_1)^2 \quad (14)$$

where T_1 , P_1 and x_1 represent the melting temperature, pressure and the mole fraction (concentration), respectively.

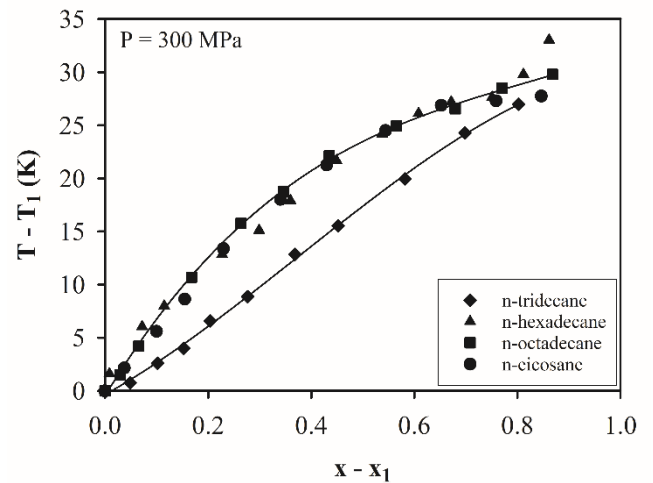


Figure 1. T - X phase diagrams calculated according to the phase line equation (Eq. (15)) which was fitted to the experimental data [32] for the solid – liquid transition of the mixtures of n-alkane (1) + n-cyclohexane (2) at $P=300$ MPa. Experimental data (within the range of temperatures) are also shown in the figure.

The coefficient a_6 in Eq (1) was considered as a constant ($a_6 = a_{60}$), independent of temperature, pressure and concentration in our treatment. The phase line equation (Eq. (5)) can then be obtained as follows:

$$T - T_1 = \alpha_0 + \alpha_1(x - x_1) + \alpha_2(x - x_1)^2 + \alpha_3(x - x_1)^3 + \alpha_4(P - P_1) \quad (15)$$

where α_0 , α_1 , α_2 , α_3 and α_4 are all constants. Those coefficients are defined as

$$\begin{aligned}
\alpha_0 &= -\frac{2a_{40}^2}{c} \\
\alpha_1 &= -4a_{40}a_{41}/c \\
\alpha_2 &= -2(a_{41}^2 + 2a_{40}a_{42})/c \\
\alpha_3 &= -4a_{41}a_{42}/c \\
\alpha_4 &= -a_{21}/a_{20}
\end{aligned}
\tag{16}$$

with the definition of $c = a_{20}a_{60}$.

In this study, the $T - X$ phase diagram was calculated for the mixtures of n-alkane (1) + cyclohexane (2) with the n-alkanes : n-tridecane (1), n-hexadecane (1), n-octadecane (1) and n-eicosane (1) at the pressure 300 MPa according to the $T - X$ phase line equation (Eq. (15)) from the Landau phenomenological model. Eq. (15) at $P = P_1 = 300$ MPa, was fitted to the experimental data [32] and the $T - X$ plots were obtained as shown in Fig. 1 for all those mixtures. Coefficients which were determined from the fits and the experimental [32] freezing temperatures T_1 with the mole fraction x_1 of n-alkanes considered, are given in Table 1.

In order to investigate the pressure effect on the solid – liquid transitions in n-alkane mixtures, $P - X$ phase diagrams at constant temperatures were constructed according to Eq. (15). For this study, Eq. (15) was fitted to the experimental data [32] at $T = T_1$ and the $P - X$ phase diagrams were obtained. Fig. 2 gives the $P - X$ phase diagrams at constant temperatures indicated for the composition x_1 for the a) n-tridecane (1) + n-hexane (2), b) n-hexadecane (1) + n-hexane (2) and c) n-octadecane (1) + n-hexane (2) systems. Coefficients determined, are given in Tables (2-4), respectively.

$P - T$ phase diagrams at constant mole fractions were also established for the solid – liquid equilibria (SLE) in the binary mixture of n-tridecane (1) + n-hexane (2) by Eq. (15) using the experimental data [32]. By choosing constant mole fractions at $x = x_1$ (Eq. (15)), the $P - T$ phase diagrams were predicted in this system, as plotted in Fig. 3(a). Values of the coefficients (Eq. (15)) which were determined for the n-tridecane (1) + n-hexane (2), are given in Table 5. Similarly, the $P - T$ phase diagrams were predicted for the systems of n-hexadecane (1) + n-hexane (2) and n-octadecane (1) + n-hexane (2) by fitting Eq. (15) to the experimental data [32] at constant mole fractions as shown in Figs. 3b and 3c, respectively, for the solid – liquid transition in those mixtures. Coefficients determined, are also given in Table 5.

Our assumption for the temperature and pressure dependence of the coefficient a_2 (Eq. (13)) represents the simplest form for the linear $T - P$ relation in the liquid – solid transition of the binary mixtures considering Eq. (5) where $a_6 = a_{60}$ as a constant. This is in accordance with the phase line equation (Eq. (5)) since we also assumed the coefficient a_4 which depends only on the concentration x (Eq. (14)). At the transition pressure ($P = P_1$), the temperature dependence of a_2 is simply $a_2 = a_{20}(T - T_1)$ which is the usual temperature dependence of the squared term in the order parameter (η^2) according to Eq. (1) in the Landau theory. From this point of view, a linear $T - P$ relation can be established in the phase diagram for the liquid – solid transition by assuming a_2 as in (Eq. (13)).

It was also assumed the quadratic dependence of the coefficient a_4 on the concentration (Eq. (14)). This assumption is also in accordance with the $T - P$ relation (Eq. 3.1) at the concentration of the first component in the binary mixture ($x = x_1$) in Eq. (14) regarding the phase line

equation (Eq. (5)) by ignoring the fourth order term in the concentration, $(x - x_1)^4$. As a result of this, cubic dependence of the temperature on the concentration (Eq. 3.3) was obtained for the $T - X$ phase diagram ($P = P_1$).

Our assumptions for the coefficients a_2 (Eq. (13)) and a_4 (Eq. (14)) can be demonstrated with the experimental measurements [32] on the n-alkanes studied here for a linear variation of pressure with the temperature at $x = x_1$ ($P - T$ phase diagrams), as shown in Fig. 3.

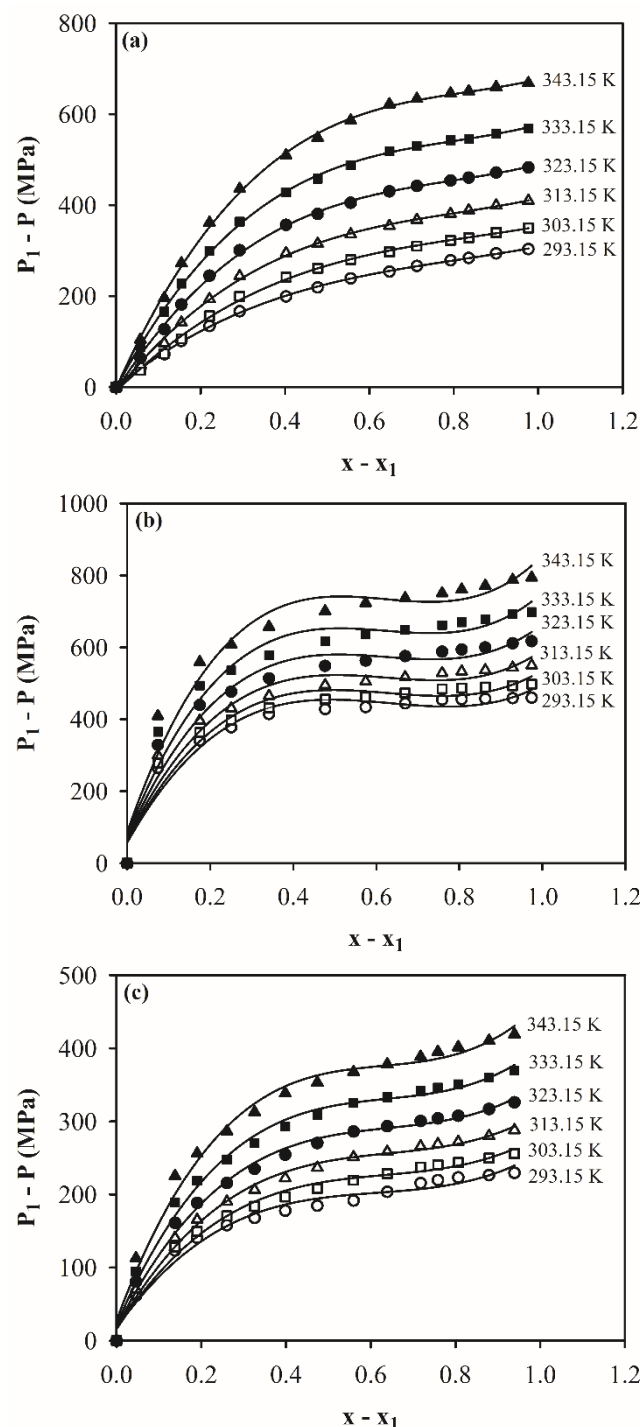


Figure 2. $P - X$ phase diagram calculated according to the phase line equation (Eq. (15)) which was fitted to the experimental data [32] for the solid – liquid transition of the mixtures a) n-tridecane (1) + n-hexane (2) b) n-hexadecane (1) + n-hexane (2) c) n-octadecane (1) + n-hexane (2) at constant temperatures indicated. Experimental data are also shown in the figure.

Table 1. Values of the coefficients determined for the solid – liquid transitions in the mixtures indicated according to the $T - X$ phase line equation (Eq. (15)) at $P=300$ MPa by using the experimental data [32]. Values of the freezing temperatures T_1 (within the range of experimental temperature) and the mole fraction x_1 of n-alkanes are also given.

T - X (Eq. 3.3)	n-tridecane (1) + cyclohexane (2)	n-hexadecane (1) + cyclohexane (2)	n-octadecane (1) + cyclohexane (2)	n-eicosane (1) + cyclohexane (2)
T_1 (K)	291.08	318.07	328.97	337.72
x_1	0.1982	0.1406	0.1340	0.1553
α_0 (K)	-0.3488	0.7428	-0.4523	-0.2115
α_1 (K)	27.22	67.44	79.78	64.58
α_2 (K)	29.75	-63.26	-80.17	-30.04
α_3 (K)	-26.49	31.39	32.65	-8.82

Table 2. Values of the coefficients determined for the solid – liquid transitions in the n-tridecane (1) + n-hexane (2) systems at constant temperatures indicated by using the experimental data [32] according to Eq. (15).

T (K)	293.15	303.15	313.15	323.15	333.15	343.15
P_1 (MPa)	436.17	547	675.17	820.69	983.54	1163.74
$(-\alpha_0/\alpha_4)$ (MPa)	0.246	9.639	8.609	7.282	1.801	2.236
$(\alpha_1/\alpha_4) \times 10^3$ (MPa)	0.752	0.925	1.158	1.446	1.740	2.070
$(-\alpha_2/\alpha_4) \times 10^3$ (MPa)	0.752	0.922	1.246	1.632	1.987	2.323
$(\alpha_3/\alpha_4) \times 10^2$ (MPa)	3.086	3.597	5.117	6.832	8.261	9.317

Table 3. Values of the coefficients determined for the solid – liquid transitions in the n-hexadecane (1) + n-hexane (2) systems at constant temperatures indicated by using the experimental data [32] according to Eq. (15).

T (K)	293.15	303.15	313.15	323.15	333.15	343.15
P_1 (MPa)	469.45	548.68	645.85	760.97	894.02	1045.01
(α_0/α_4) (MPa)	56.85	60.08	64.78	70.62	77.55	85.55
$(\alpha_1/\alpha_4) \times 10^3$ (MPa)	2.056	2.166	2.346	2.600	2.930	3.335
$(-\alpha_2/\alpha_4) \times 10^3$ (MPa)	3.424	3.603	3.897	4.319	4.862	5.529
$(\alpha_3/\alpha_4) \times 10^3$ (MPa)	1.808	1.913	2.078	2.313	2.606	2.963

Table 4. Values of the coefficients determined for the solid – liquid transitions in the n-tridecane (1) + n-hexane (2) systems at constant temperatures indicated by using the experimental data [32] according to Eq. (15).

T (K)	293.15	303.15	313.15	323.15	333.15	343.15
P_1 (MPa)	238.60	305.71	383.16	470.94	569.05	677.49
(α_0/α_4) (MPa)	17.47	15.85	16.10	18.22	22.19	28.02
$(\alpha_1/\alpha_4) \times 10^3$ (MPa)	0.818	0.892	1.002	1.149	1.333	1.553
$(-\alpha_2/\alpha_4) \times 10^3$ (MPa)	1.262	1.322	1.464	1.689	1.995	2.384
$(\alpha_3/\alpha_4) \times 10^2$ (MPa)	6.849	6.948	7.577	8.734	1.042	1.264

$T - X$ (at $P = P_1$) phase diagrams (linear and quadratic fits are also possible) (Fig. 1) and $P - X$ (at $T = T_1$) phase diagrams (Fig. 2) were also based on the experimental measurements [32].

In our previous studies [23, 25, 26] linear dependence of the coefficient a_2 on the temperature and concentration, and the quadratic dependence of a_4 on the concentration, have been assumed to describe the observed phase diagrams of tetradecane + hexadecane within the Landau phenomenological model. Recently, those dependences have

also been assumed for the solid – liquid equilibria in n-tridecane [27].

As studied for the $P - X$ and $P - T$ phase diagrams, the pressure effect was also investigated on the thermodynamic quantities for the solid – liquid phase transition in the mixtures considered in this study. For that purpose, the order parameter, susceptibility and the thermodynamic quantities of heat capacity, entropy and enthalpy were predicted as a function of pressure at constant temperatures by means of the Landau phenomenological model on the basis of the $P - X$ and $P - T$ phase diagrams for the mixtures studied here. For

the pressure dependence of the order parameter η , Eqs. (13) and (14) can be substituted into Eq. (4) at $T = T_1$ and $x = x_1$, which gives

$$\eta^2 = \eta_o^2 (P - P_1) \quad (17)$$

where $\eta_o^2 = a_{21}/a_{40}$. Using Eq. (17), the order parameter η was calculated as a function of pressure at constant temperatures and mole fractions, as indicated (Fig. 4) for the mixtures of n-tridecane (1) + n-hexane (1), n-hexadecane (1) + n-hexane (2) and n-octadecane (1) + n-hexane (2).

Similarly, for those three mixtures, the pressure dependence of the inverse susceptibility (χ_η^{-1}) was predicted at constant temperatures (and mole fractions), by means of Eq. (7). This was done by inserting Eq. (17) into Eq. (7) where the linear term in η was considered. Thus, the pressure dependence of the inverse susceptibility χ_η^{-1} is given by

$$\chi_\eta^{-1} = \chi_o^{-1} (P - P_1)^{1/2} \quad (18)$$

where the amplitude is defined as $\chi_o^{-1} = 4(a_{21}a_{40})^{1/2}$. χ_η^{-1} versus P plots are given in Fig. 4 for the mixtures of n-tridecane (1) + n-hexane (2), n-hexadecane (1) + n-hexane (2) and n-octadecane (1) + n-hexane (2).

Regarding the thermodynamic quantities of the heat capacity (C), entropy (S) and the enthalpy (H), those functions were also calculated as a function of pressure at constant temperatures (at constant mole fractions). By means of Eq. (15) at constant concentration (mole fraction, $x = x_1$), the pressure dependence of the heat capacity C through Eq. (8) is obtained as

$$C = C_o T [-\alpha_1 - \alpha_4 (P - P_1)]^{-1/2} \quad (19)$$

Also, the pressure dependence of the entropy difference $\Delta S = S - S_o$ can be expressed by using Eq. (9) in Eq. (15) as

$$\Delta S = \Delta S_o [-\alpha_1 - \alpha_4 (P - P_1)]^{1/2} \quad (20)$$

where $\Delta S_o = -2C_o$. The enthalpy difference $\Delta H = H - H_o$ which is given by Eq. (10), can be written as

$$\Delta H = \Delta H_o T [-\alpha_1 - \alpha_4 (P - P_1)]^{1/2} \quad (21)$$

with $H_o = -C_o$ by means of Eq. (15). Using Eqs. (19) - (21), respectively, for the solid – liquid transition in the mixtures studied as also indicated for the predictions of the order parameter and susceptibility. $C - P$, $S - P$ and $H - P$ plots at constant temperatures were predicted as given in Figs. (5-7), respectively. Those thermodynamic functions (C , ΔS and ΔH) were normalized. The α_0 and α_4 values of Eq. (15) (Tables 4 and 5) are also given for C , ΔS and ΔH functions in Table 6. On the basis of our assumptions for the coefficients a_2 (Eq. (13)) and a_4 (Eq. (14)), the pressure dependences of the order parameter η (Eq. (17)), the inverse susceptibility χ_η^{-1} (Eq. (18)), the heat capacity C (Eq. (19)), the entropy difference ΔS (Eq. (20)) and the enthalpy difference ΔH (Eq. (21)) were calculated for the solid – liquid transition in the binary mixtures studied. These dependences are also in accordance with the temperature dependences of

those functions based on our assumptions (a_2 and a_4) for the tetradecane + hexadecane as studied previously [23, 26].

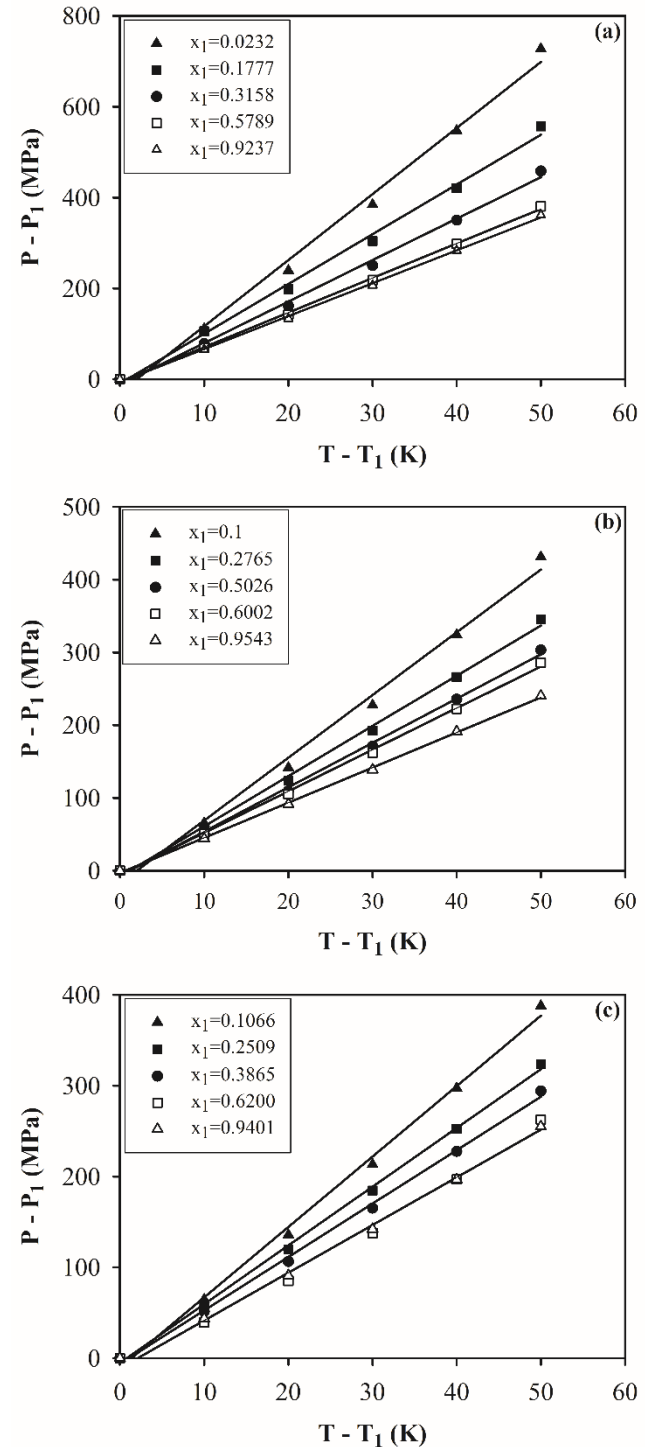


Figure 3. P - T phase diagrams calculated according to the phase line equation (Eq. (15)) which was fitted to the experimental data [32] for the solid – liquid transition of the mixtures a) n-tridecane (1) + n-hexane (2) b) n-hexadecane (1) + n-hexane (2) c) n-octadecane (1) + n-hexane (2) at constant mole fractions indicated. Experimental data are also shown in the figure.

This is because of the fact that the temperature T varies linearly with the pressure P for the binary mixtures studied here as measured experimentally [32]. In the case when T varies nonlinearly with the P , which can occur for some binary mixtures close to the solid – liquid transition, our assumption for the coefficient a_2 is no longer valid to

describe the $P - T$ phase diagram. However, the pressure dependence of η (Eq. (17)), χ_{η}^{-1} (Eq. (18)), C (Eq. (19)), ΔS (Eq. (20)) and ΔH (Eq. (21)) can still be used by ignoring some higher order terms to describe the solid - liquid transition in those binary mixtures.

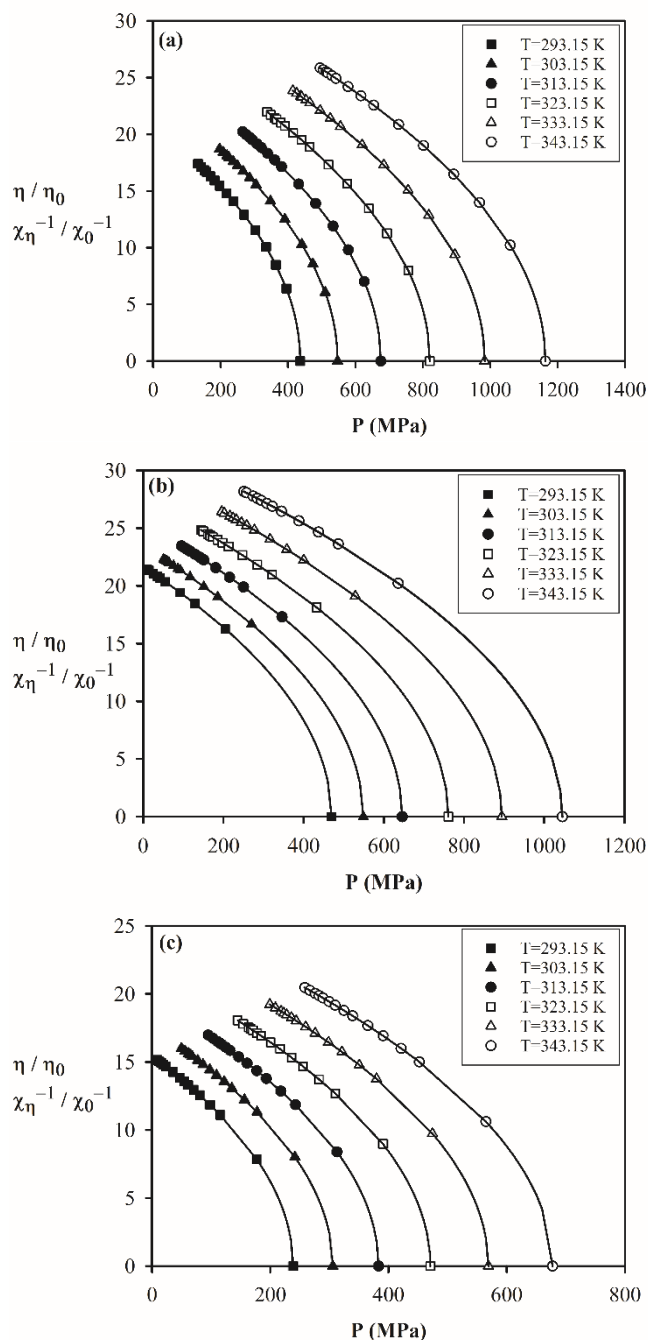


Figure 4. Pressure dependence of the order parameter η and the inverse susceptibility χ_{η}^{-1} (normalized) at constant temperatures within the experimental temperature intervals [32] according to Eqs. (17) and (18), respectively, for the solid - liquid transition in the mixtures a) *n*-tridecane (1) + *n*-hexane (2) b) *n*-hexadecane (1) + *n*-hexane (2) c) *n*-octadecane (1) + *n*-hexane (2).

4. Discussion

In this study, the temperature-concentration ($T - X$), the pressure-concentration ($P - X$) and the pressure-temperature ($P - T$) phase diagrams were described theoretically by the Landau mean field theory. Those phase diagrams involve the phase separation between the liquid and

solid phases. The Landau phenomenological model was used instead the Gibbs method of constructing of phase diagrams. Also, on this basis the thermodynamic functions of interest were calculated as a function of pressure for the binary mixtures studied, as stated above.

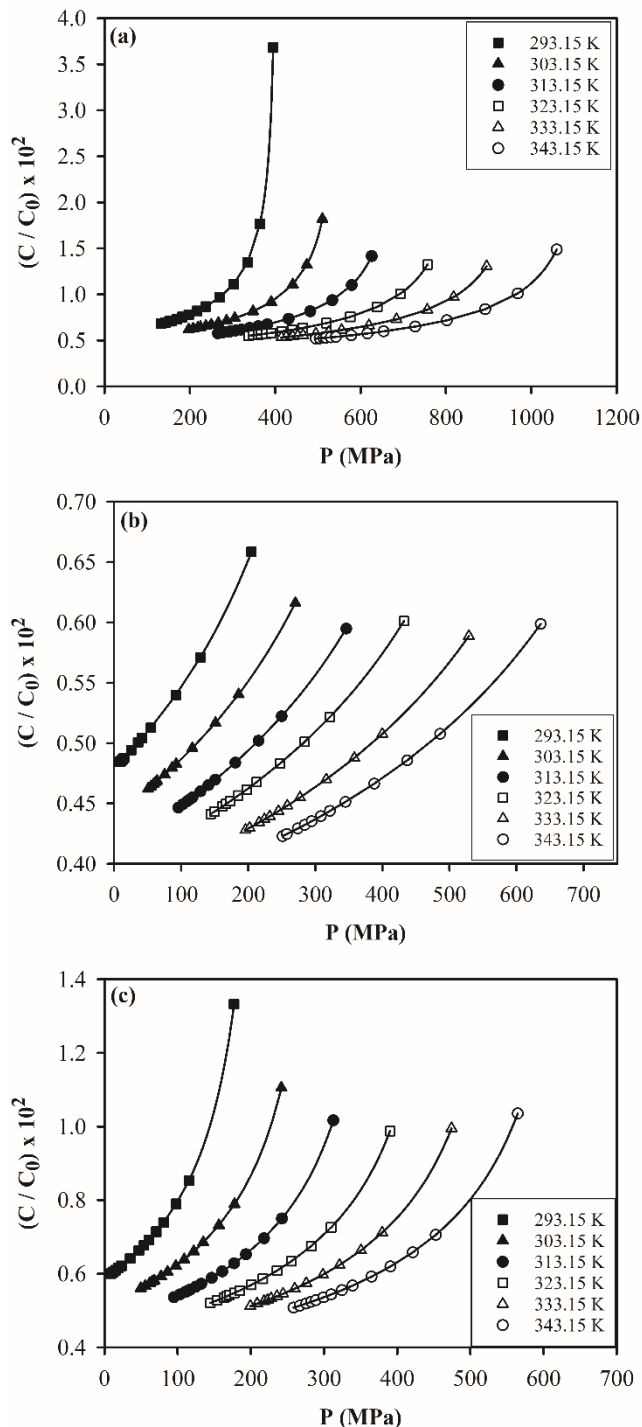


Figure 5. Pressure dependence of the heat capacity C at constant temperatures within the experimental temperature intervals [32] according to Eq. (19) for the solid - liquid transition in the mixtures a) *n*-tridecane (1) + *n*-hexane (2) b) *n*-hexadecane (1) + *n*-hexane (2) c) *n*-octadecane (1) + *n*-hexane (2).

$T - X$ phase diagrams of *n*-alkanes + *n*-cyclohexane at 300 MPa (Fig. 1), $P - X$ phase diagrams of *n*-alkanes + *n*-hexane at constant temperatures (Fig. 2) and $P - T$ phase diagrams of *n*-alkanes + *n*-hexane at constant concentrations (Fig. 3), which were obtained by fitting Eq. (15) to the

experimental data [32] are reasonably good. This shows that in the polynomial expansion (Eq. (15)), the cubic dependence of the concentration (mole fraction) on the temperature and pressure is adequate to describe the solid-liquid transition in those binary mixtures studied. This also confirms the functional form of the temperature and pressure dependence of the coefficient a_2 (Eq. (13)), and the concentration dependence of a_4 (Eq. (14)) for the phase line equation (Eq. (5)) in the expansion of the free energy F_s (Eq. (1)) which describes the solid-liquid transition in the binary mixtures of n-alkanes according to the Landau mean field theory. On the other hand, a linear dependence of some of the coefficients on the T and X variables to obtain, by a linear transformation, the phase diagram in the $T - X$ phase, has been assumed [39]. Also, a nonlinear dependence on concentration of the free energy coefficients has been considered for the liquid - solid transition to construct the temperature - concentration phase diagrams of binary eutectic mixtures [40], as was assumed in the present study. Another approach by representing an excess Gibbs energy model [41], the effect of pressure on the liquidus curve in a ($T - X$) phase diagram has been studied for the binary mixtures (tetradecane + pentadecane and tetradecane + hexadecane) [21]. By means of the Landau phenomenological model which explains the observed behaviour of the $T - X$ phase diagrams under pressure adequately, have been obtained for those binary mixtures in

our recent study [25]. This also shows that the Landau mean field model is satisfactory to obtain the $T - X$ phase diagram under high pressure, as we studied here for the binary mixtures of n-alkanes (1) + cyclohexane (2). As seen from the $T - X$ phase diagrams at 300 MPa (Fig. 1), the melting temperatures (T_1) increase with the small decrease in the composition x_1 of the cyclohexane for the n-alkanes namely, n-tridecane, n-hexadecane, n-octadecane and n-eicosane, respectively, on the basis of the experimental data [32]. Our $T - X$ phase diagrams (Fig. 1) show that the mixture of n-tridecane (1)+n-cyclohexane (2) is somehow different from the other three mixtures, namely, n-hexadecane, n-octadecane and n-eicosane, which follow almost the same phase line. This is mainly the variation of alkane molecule conformation and in -planar phase structure along with temperature. So that an increase in pressure can cause the composition and the structure of the different solid phases in this binary mixture. As noticed, the $T - T_1$ values of the n-tridecane are much lower than those three mixtures (Fig. 1). Similarly, as in the $T - X$ phase diagrams (Fig. 1), for the $P - X$ phase diagrams (Fig. 2) at constant temperatures, pressure increases as the concentration increases [32]. The melting pressure (P_1) increases as the temperature increases at a constant concentration (x_1) of n-hexane.

This is shown for example, at $x_1 = 0.0232$ (within the pressure range of 436.17 to 1163.74 MPa) for n-tridecane, $x_1 = 0.0260$ (pressure range of 469.45 to 1045.01 MPa) for

Table 5. Values of the coefficients determined for the solid - liquid transitions in the n-alkanes (1) + n-hexane (2) according to Eq. (15) which was fitted to the experimental data [32] at constant mole fractions indicated.

n-tridecane (1) + n-hexane (2)	x_1	0.0232	0.1777	0.3158	0.5789	0.9237
	α_0 (K)	2.159	0.967	1.391	0.764	0.881
	$\alpha_4 \times 10^{-2}$ (K/MPa)	6.82	9.09	10.91	13.12	13.79
n-hexadecane (1) + n-hexane (2)	x_1	0.1	0.2765	0.5026	0.6002	0.9543
	α_0 (K)	2.185	1.249	1.242	0.978	0.678
	α_4 (K/MPa)	0.115	0.144	0.164	0.175	0.207
n-octadecane (1) + n-hexane (2)	x_1	0.1066	0.2509	0.3865	0.6200	0.9401
	α_0 (K)	1.472	0.853	1.131	2.314	1.268
	α_4 (K/MPa)	0.128	0.154	0.170	0.189	0.196

Table 6. Values of the coefficients α_0 and α_4 according to Eq. (15) at $x = x_1$ for the n-alkanes (1) + n-hexane (2) as indicated at constant temperatures T_1 and pressure P_1 , which were determined to predict the pressure dependence of C (Fig. 5), S (Fig. 6) and H (Fig. 7).

n-tridecane (1) + n-hexane (2)	T_1 (K)	293.15	303.15	313.15	323.15	333.15	343.15	
	$x_1 = 0.0232$							
	P_1 (MPa)	436.17	547.00	675.17	820.69	983.54	1163.74	
$\alpha_4 = 6.821 \times 10^{-2}$ (K/MPa)	α_0 (K)	2.159	-0.282	-1.540	-1.614	-0.507	1.783	
	n-hexadecane (1) + n-hexane (2)	P_1 (MPa)	469.45	548.68	645.85	760.97	894.02	1045.01
		$x_1 = 0.0260$						
α_0 (K)		2.884	-0.321	-1.199	-2.115	-0.705	2.244	
$\alpha_4 = 8.576 \times 10^{-2}$ (K/MPa)	n-octadecane (1) + n-hexane (2)	P_1 (MPa)	238.60	305.71	383.16	470.94	569.05	677.49
		$x_1 = 0.0608$						
		α_0 (K)	2.131	-0.280	-1.521	-1.594	-0.499	1.764
$\alpha_4 = 1.131 \times 10^{-2}$ (K/MPa)								

n-hexadecane and $x_1 = 0.0608$ (pressure range of 238.60 to 677.49 MPa) for n-octadecane on the basis of the experimental data [32].

From our $P - X$ phase diagrams (Fig. 2), we also see that the variation of $P_1 - P$ with the $x - x_1$ is rather smooth for the n-tridecane (Fig. 2a) as compared to those of n-hexadecane (Fig. 2b) and n-octadecane (Fig. 2c). So that for the n-tridecane (1) + n-hexane (2), the quadratic dependence of the concentration on the pressure, $P_1 - P \propto (x - x_1)^2$, according to Eq. (15) can also describe the observed data [32]. Since the cubic dependence of concentration on the pressure (Eq. 15) was fitted at constant temperatures to the $P - X$ phase diagrams of binary mixtures studied (Fig. 2), the best curve-fitting was obtained although some experimental data points [32] do not coincide with the curve exactly in Fig. 2b. Of course, it is always possible to fit the data perfectly by choosing different functional forms (higher order polynomials or exponential functions). However, this contradicts with the theory outlined and the method of calculation given in this study. One possible explanation is that the method of analysis is not well satisfied in the case of n-hexadecane (1) + n-hexane (2) (Fig. 2b) as compared to the binary mixtures of n-tridecane (1) + n-hexane (2) (Fig. 2a) and n-octadecane (1) + n-hexane (2) (Fig. 2c).

Note that the fourth order term was also considered in the concentration, $(x - x_1)^4$, in the expansion (Eq. (15)) to get the best fit for the $T - X$ phase diagram (Fig. 2b). But, this did not change the curve-fitting and some data points were not exactly on the curve as before (Fig. 2b). Regarding the $P - T$ phase diagrams of those binary mixtures of n-alkanes (Fig. 3), pressure increases as the temperature increases at constant compositions, as stated above. In our plots (Fig. 3), some constant concentrations of the n-hexane (1) were arbitrarily chosen for the binary mixtures of n-tridecane, n-hexadecane and n-octadecane by using the experimental data [32]. For the other constant compositions (x_1) between 0 and 1 as given from the experimental measurements [32] of those mixtures, the same behavior can be expected in the $P - T$ phase diagrams for their solid-liquid transitions. Note that the $T - P$ phase diagram for the high-pressure solid - liquid phase equilibria in synthetic waxes, in particular, melting curve of n-tridecane, has been obtained by the Landau mean field model using the experimental data [14], in our very recent study [27]. As indicated in the experimental study [14], the $T - P$ variation is not too far from linearity and the average slope between atmospheric and 100 MPa was estimated (0.193 K/MPa), which also confirms our linear $T - P$ assumption in our study [27] and the present study.

Note that increase in $T - T_1$ with the $x - x_1$ at 300 MPa as the concentration of n-alkanes (x_1) increases (Fig. 1) and also increase in $P - P_1$ with the $T - T_1$ at various concentrations (Fig. 3), occur above the melting point (T_1, P_1) for the solid - liquid transition in the binary mixtures studied. On the other hand, as the x_1 increases at constant temperatures, the pressure difference ($P_1 - P$) increases below the melting pressure (P_1) for the solid - liquid transition as given in Fig. 2. In terms of the binary mixtures studied, when n-cyclohexane (2) is concentrated with the n-alkanes (1), the freezing temperatures (T_1) of these binary mixture increase at a constant pressure (300 MPa) (Fig. 1), whereas the transition pressure (P_1) decreases at constant temperatures (Fig. 2) for the binary mixtures as measured experimentally [32]. At constant concentrations of the n-

alkane (1) + n-cyclohexane (2) increasing the freezing temperature (T_1) requires higher pressures (P_1) (Fig. 3).

For the $T - X$ (Fig. 1), $P - X$ (Fig. 2) and $P - T$ (Fig. 3) phase diagrams, Eq. (15) with the cubic dependence of the concentration and linear dependence of the pressure on the temperature, is adequate to describe the observed behaviour of the phase diagrams for the binary mixtures studied, as stated above. Initially, Eq. (15) was fitted to the experimental data [32] for all those mixtures separately with the curves covering all the experimental data points (Figs. 1-3). Our fittings showed us in the case of the binary mixtures n-hexadecane, n-octadecane and n-eicosane, their $T - X$ phase diagrams exhibited similar behaviour for the solid - liquid transition, which was different from the mixture of n-tridecane (Fig. 1). On that basis, a single curve was obtained for those binary mixtures as shown in Fig. 1. This is the reason why some data points are not exactly on the curve. Thus, this single curve characterizes the observed behaviour of those binary mixtures regarding their solid - liquid phase transition.

Note that instead of $T - X_1$, $P - X_1$ and $P - T$ plots for the binary mixtures as given experimentally [32], $T - T_1$ versus $x - x_1$ (Fig. 1), $P_1 - P$ versus $x - x_1$ (Fig. 2) and $P_1 - P$ versus $T - T_1$ (Fig. 3) were plotted according to Eq. (15) in our treatment. This provides variation of the temperature (with respect to the freezing temperature T_1) with the mole fraction x of n-alkane (1) at $P = 300$ MPa (Fig. 1), variation of the pressure (with respect to the transition pressure P_1) with the $(x - x_1)$ at constant temperatures (Fig. 2) and the variation of the $P - P_1$ with the $T - T_1$ at constant concentrations (Fig. 3), as stated above. In particular, in the case of the $T - T_1$ versus $x - x_1$ plot (Fig. 1), Eq. (15) was fitted to the experimental data [32] above $x_1 = 0.2$ up to $x_1 = 1.0$ for the n-alkane (1) + cyclohexane (2), where n-alkanes (1) are n-tridecane, n-hexadecane, n-octadecane and n-eicosane. Thus, the two discontinuous phase lines (above and below $x_1 = 0.2$) which coincide at the triple points for those binary mixtures do not appear in our $T - T_1$ versus $x - x_1$ plot (Fig. 1).

Also, in the case of the variation of $P - P_1$ with the $T - T_1$, at constant concentrations (Fig. 3), our fit is not reasonably well, in particular at $x_1 = 0.0232$ (Fig. 3a), $x_1 = 0.1$ (Fig. 3b) and $x_1 = 0.1066$ (Fig. 3c), as shown by the symbol \blacktriangle for the n-alkanes (1) + n-hexane (2). Our fits are good starting from the high concentrations ($x_1 \cong 0.92 - 0.95$) of the n-alkanes (1). As the constant concentration (x_1) decreases, regarding the variation of $P - P_1$ with the $T - T_1$, it seems that Eq. (15) does not describe the $T - X$ phase diagram satisfactorily. This would mean that the mean field model studied here, is probably inadequate to explain the observed $P - T$ phase diagram of the n-alkanes (1) + n-hexane (2) at very low concentrations (x_1).

On the basis of the phase diagrams ($T - X$, $P - X$ and $P - T$) for the binary mixtures of n-alkanes which were calculated, the pressure dependence of the order parameter, and susceptibility with the thermodynamic quantities of the heat capacity, entropy and enthalpy, were also predicted for the liquid-solid transition in those mixtures. According to Eq. (17), pressure dependence of the order parameter η (quadratic) from the Landau mean field theory, is satisfactory at constant temperatures for the n-alkanes (n-tridecane, hexadecane and n-octadecane) + n-hexane, as shown in Fig. 4. The order parameter η (normalized) decreases to zero as the transition pressure (P_1) is approached

at constant temperatures as indicated and it shifts to higher pressure values with increasing temperature (Fig. 4). The pressure dependence of the order parameter η (Eq. (17)) is the same as the temperature dependence of ψ (order parameter) (Eq. (12)) since the pressure ($P - P_1$) is directly proportional to the temperature ($T - T_1$) as shown for the binary mixtures (Fig. 3) on the basis of the experimental measurements [32]. Since the liquid phase has no ordering, the order parameter η of the solid phase goes to zero as the temperature increases to the melting temperature (T_1) or the pressure increases to the melting pressure (P_1) for the solid – liquid transition, as obtained for the binary mixtures studied (Fig. 4).

Considering the quadratic dependence of the order parameter η on the pressure (Eq. (17)) or its temperature dependence (Eq. (4)) through Eq. (13) with the critical exponent $1/2$ according to $\eta \propto (T - T_1)^{1/2}$, the transition can change its character from the first order to a second order or vice versa within the extended mean field model [34] when the order parameter is calculated from the heat capacity (Eq. (11)) according to Eq. (12) with the critical exponent $\phi = 1/4$. This indicates that the discontinuous (first order) change can become a continuous one (second order), which is tricritical transition with the critical exponent value $1/4$ of the order parameter within mean field theory [42, 43]. Experiments can examine the critical behavior of the order parameter as measured at various temperatures and pressures for the binary mixtures studied here.

Similarly, the pressure dependence of the inverse susceptibility (χ_η^{-1}) that was obtained for the mixtures of n-alkanes at constant temperatures (Fig. 4), exhibits the behavior as expected from the Landau phenomenological model according to Eq. (7) where the order parameter η (Eq. (17)) was used. Since the functional form of the inverse susceptibility of the order parameter as a function of the pressure (Eq. (18)) is the same as the order parameter η (Eq. (17)), it decreases with the pressure and it approaches to zero at the transition pressure (P_1) for those binary mixtures studied. That is why we plotted η (normalized) and χ_η^{-1} (normalized) as a function of pressure in the same figure (Fig. 4) for the solid – liquid transition in the binary mixtures studied. As in the case of the order parameter η (Fig. 4), the normalized inverse susceptibilities increase in their values as the temperature increases (Fig. 4). When the order parameter (η) and the inverse susceptibility (χ_η^{-1}) of the order parameter are normalized according to Eqs. (17) and (18), respectively, as a function of pressure at constant temperatures they characterize the same solid – liquid transition in the binary mixtures studied (Fig. 4), as stated above.

Since the melting pressure increases as the temperature increases (Fig. 3), the susceptibility χ_ψ (response function) of the order parameter, increasing with the temperature also increases (or the inverse susceptibility decreases) with the pressure at constant temperatures. This occurs at constant temperatures from 293.15 to 343.15 K, accompanied with the increasing the melting pressure. This is shown also in the inverse susceptibility as the order parameter for the solid – liquid transition in the mixtures studied (Fig. 4). Note that for the variation of χ_η^{-1} with the pressure, only the linear term in η was considered with the critical exponent $1/2$ of η (Eq. (17)), which is the dominant term as compared to the η^3 term (Eq. (7)) with the exponent $3/2$.

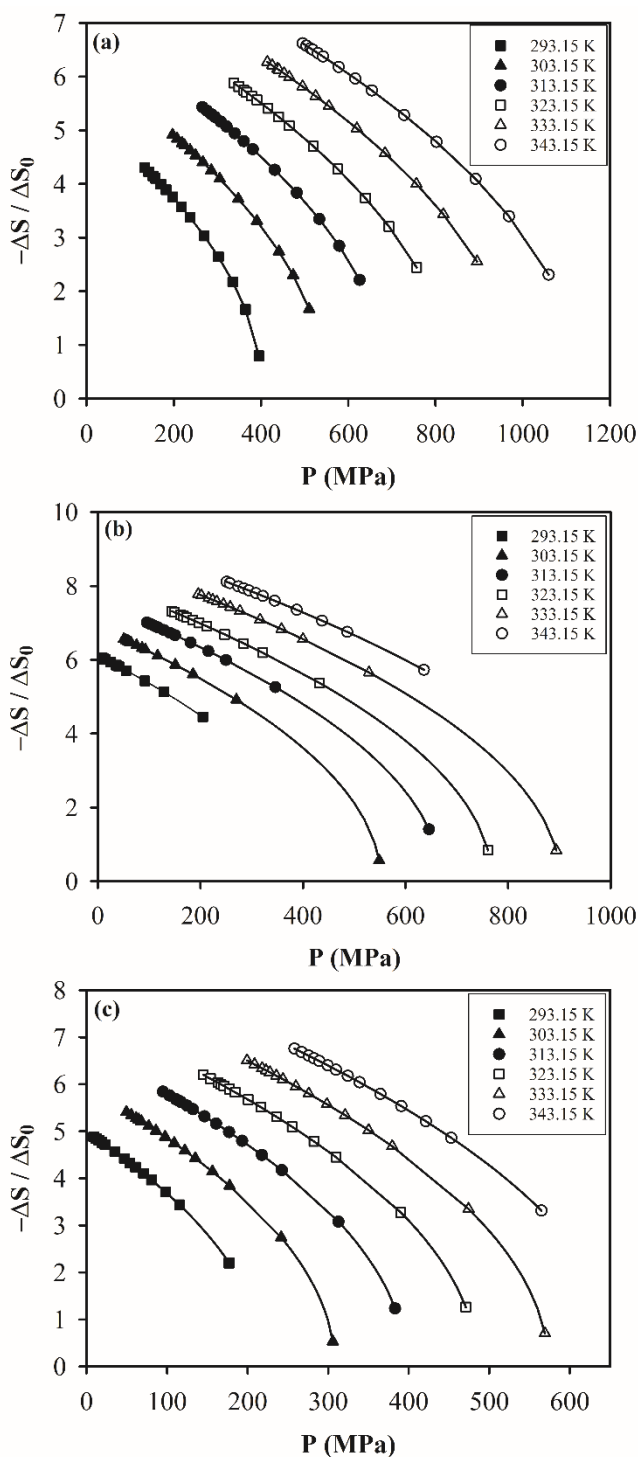


Figure 6. Pressure dependence of the entropy difference ΔS at constant temperatures within the experimental temperature intervals [32] according to Eq. (20) for the solid – liquid transition in the mixtures a) n-tridecane (1) + n-hexane (2) b) n-hexadecane (1) + n-hexane (2) c) n-octadecane (1) + n-hexane (2). ΔS is normalized ($\Delta S/\Delta S_0$) where $\Delta S_0 = 2C_0$ (Eq. (20)).

Regarding the thermodynamic quantities of the heat capacity (C), entropy (S) and the enthalpy (H), the extended mean field model [34] was employed according to Eqs. (8), (9) and (10), respectively, as stated above. The pressure dependence of the heat capacity which was calculated by means of Eq. (19), shows divergence behaviour with the critical exponent $\alpha = 1/2$, as expected from the extended mean field model [34]. This occurred at constant temperatures from 293.15 K to 343.15 K for the binary

mixtures of n-tridecane + n-hexane, n-hexadecane + n-hexane and n-octadecane + n-hexane (Fig. 5). As seen from this figure, variation of the heat capacity C (normalized) is considerably sharp with the pressure at 293.15 K as compared to the other constant temperatures for n-tridecane (Fig. 5a). Also, its magnitude is higher at this temperature ($T = 293.15\text{ K}$) in comparison with those at the other temperatures for all the three mixtures (Fig. 5).

It can be considered that in a very small temperature interval close to the freezing temperature T_1 , the heat capacity (C) diverges largely as a function of temperature at zero pressure ($P = 0$) according to Eq. (8) for the liquid – solid transition. Correspondingly, a large divergence behaviour of the heat capacity can occur in a very small pressure interval close to the transition pressure P_1 as a function of pressure at the room temperature ($T = 293.15\text{ K}$) under the experimental conditions ($P = 0$, $T = 293.15\text{ K}$) according to Eq. (19) for the liquid – solid transition. This is a possible explanation why the critical behaviour of the heat capacity (C) as a function of pressure at 293.15 K, is different from those at higher temperatures for the solid – liquid transition in the n-alkanes (1) + n-hexane (2) mixtures (Fig. 5). We see that the heat capacity (C/C_0) increases smoothly with the increasing pressure (except at 293.15 K) at the constant temperatures indicated for those binary mixtures as studied here (Fig. 5). Pressure dependence of the heat capacity exhibits similar critical behavior for those three mixtures close to their liquid-solid transition according to the extended mean field model which can be examined experimentally for those binary mixtures.

On the basis of the critical behavior of the heat capacity (C) at various pressures for constant temperatures (Fig. 5), the entropy difference ΔS and the enthalpy difference ΔH are also expected to exhibit similar behavior with the pressure (at constant temperatures), according to Eqs. (20) and (21), which are shown in Figs. 6 and 7, respectively, for the three binary mixtures, namely, n-tridecane + n-hexane, n-hexadecane + n-hexane and n-octadecane + n-hexane close to their solid-liquid transition.

This is due to the fact that the pressure dependences of the ΔS (normalized) and ΔH (normalized) are in the same functional form except that ΔH is divided by the temperature T (constant), as given by Eqs. (20) and (21), which were plotted in Figs. (6) and (7), respectively. Since both functions (ΔS and ΔH) were derived from the heat capacity C , their temperature (Eqs. (9) and (10)) or pressure (Eqs. (20) and (21)) dependences exhibit within the extended mean field model [34] similar solid – liquid transition for the binary mixtures studied. This was exemplified for the order parameter η and the inverse susceptibility χ_ψ^{-1} (Fig. 4) also in the present study. Note that similar to our treatment, entropy and enthalpy were calculated based on the heat capacity curve fitting for the experimental measurements of n-alkanes in a wide temperature range from 1.9 K to 370 K using differential scanning and adiabatic calorimetry method [36]. As indicated in our previous study [21], the difference in the enthalpy ΔH as the observed heat of fusion, increases with increasing temperature, which was observed experimentally for the tetradecane + hexadecane. Since T is directly proportional to the pressure as assumed here (Eq. (15)) with the $P - T$ phase diagrams (Fig. 3) for the binary mixtures studied here, enthalpy (ΔH) should be increasing with the pressure (or negative ΔH decreases with P), as given in Fig. 7 for those binary mixtures.

Similar behaviour of the ΔS and ΔH due to the critical behaviour of the heat capacity from the extended mean field model [34] which can be tested by the measurements of those quantities for the solid-liquid transitions of the binary mixtures as studied here.

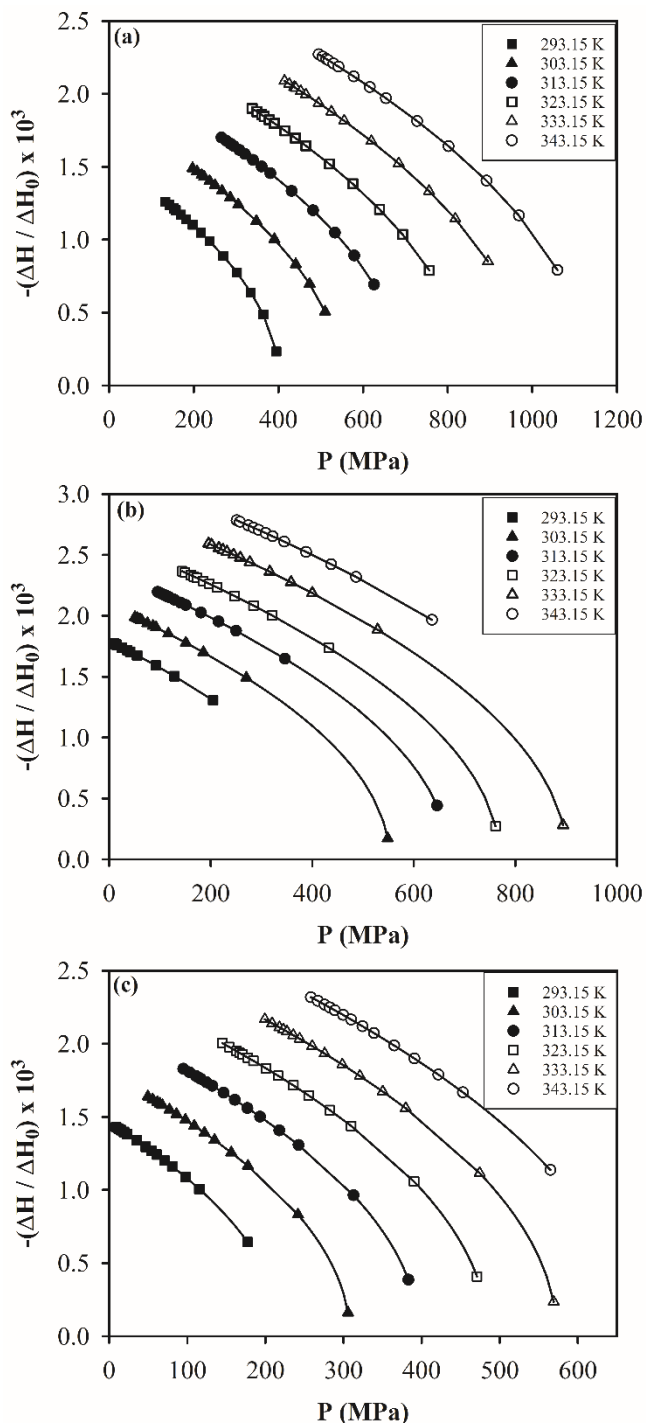


Figure 7. Pressure dependence of the difference ΔH at constant temperatures within the experimental temperature intervals [32] according to Eq. (21) for the solid – liquid transition in the mixtures a) n-tridecane (1) + n-hexane (2) b) n-hexadecane (1) + n-hexane (2) c) n-octadecane (1) + n-hexane (2). ΔH is normalized ($\Delta H / \Delta H_0$) where $\Delta H_0 = C_0$ (Eq. (21)).

5. Conclusions

The free energy of the solid phase was expanded in terms of the solid phase under pressure for the solid – liquid transition in the binary mixtures of n-alkanes within the

framework of the Landau phenomenological model. The $T - X$ (at 300 MPa), $P - X$ (at constant temperatures) and $P - T$ (at constant concentrations) phase diagrams were obtained for those binary mixtures by using the experimental data from the literature. Cubic dependence of the concentration on the temperature ($T - X$) and the linear dependence of the pressure on the temperature ($P - T$) were considered in our treatment. The $T - X$ phase diagram of n-alkanes (1) (n-hexadecane, n-octadecane and n-eicosane) + cyclohexane (2) was represented by a single non-linear curve, whereas for the n-tridecane (1) + cyclohexane (2) T varied almost linearly with x . The pressure dependences of the order parameter, susceptibility, heat capacity, entropy and the enthalpy, were also predicted for the mixtures studied. Those predictions studied as a function of pressure can be tested experimentally for the binary mixtures at constant temperatures and concentrations. This can explain the pressure effect on the phase diagrams and on the thermodynamic functions to describe the mechanism of the solid – liquid transition in the binary mixtures for future studies.

Nomenclature

T	temperature (K)
T_1	melting temperature (K)
x	concentration (mole fraction) (%)
x_1	melting concentration (%)
P	pressure (MPa)
P_1	melting pressure (MPa)
η	order parameter
χ_η	order parameter susceptibility
F	free energy (J/mol)
C, C_0	heat capacity (J/mol.K)
S, S_0	entropy (J/mol.K)
H, H_0	enthalpy (J/mol)

References:

- [1] D.S. Fu, Y.L. Su, B.Q. Xie, H.J. Zhu, G.M. Liu and D.J. Wang, “Phase change materials of n-alkane-containing microcapsules: observation of coexistence of ordered and rotator phases”, *Phys. Chem. Chem. Phys.*, *13*, 2021-2026, 2011.
- [2] D.S. Fu, Y.F. Liu, X. Gao, Y.L. Su, G.M. Liu, D.J. Wang, “Binary n-Alkane Mixtures from Total Miscibility to Phase Separation in Microcapsules: Enrichment of Shorter Component in Surface Freezing and Enhanced Stability of Rotator Phases”, *J. Phys. Chem. B*, *116*, 3099-3105, 2012.
- [3] P.K. Mukherjee, “Pressure effect on the rotator-II to rotator I transition of alkanes”, *J. Chem. Phys.*, *130*, 214906, 2009.
- [4] A. Craievich, J. Doucet and I. Denicolo, “Molecular disorder in even-numbered paraffins”, *Phys. Rev. B*, *32*, 4164-4168, 1985.
- [5] G. Ungar, N. Masic, “Order in the rotator phase of normal alkanes”, *J. Phys. Chem.*, *89*, 1036-1042, 1985.
- [6] E. B. Sirota, “Rotator phases of the normal alkanes: An x-ray scattering study”, *J. Chem. Phys.*, *98*, 5809-5824, 1993.
- [7] E. B. Sirota, “Remarks concerning the relation between rotator phases of bulk n-alkanes and those of langmuir

monolayers of alkyl-chain surfactants on water”, *Langmuir*, *13*, 3849-3859, 1997.

- [8] I. Koljanin, M. Pozar, B. Lovrinevic, “Structure and Dynamics of liquid linear and cyclic alkanes: A molecular Dynamics study”, *Fluid Phase Equilibria*, *550*, 113237, 2021.
- [9] D.S. Fu, Y.F. Liu, G.M. Liu, Y.L. Su, D.J. Wang, “Confined crystallization of binary n-alkane mixtures: stabilization of a new rotator phase by enhanced surface freezing and weakened intermolecular interactions”, *Phys. Chem. Chem. Phys.*, *13*, 15031-15036, 2011.
- [10] R.R. Nelson, W. Webb and J.A. Dixon, “First-order phase transitions of six normal paraffins at elevated pressures”, *J. Chem. Phys.*, *33*, 1756-1764, 1960.
- [11] B. Koppitz and A. Würflinger, “Differential thermal analysis at elevated pressure”, *Colloid Polym. Sci.*, *252*, 999-1000, 1974.
- [12] C. Josefiak, A. Würflinger and G.M. Schneider, “Differential thermal analysis under high pressure”, *Colloid Polym. Sci.*, *255*, 170-171, 1977.
- [13] S.N. Gunasekara, S. Kumova, J.N. Chiu, V. Martin, “Experimental phase diagram of the dodecane-tridecane system as phase change material in cold storage”, *Int. J. Ref.*, *82*, 130-140, 2017.
- [14] J.L. Daridon, J. Pauly and M. Milhet, “High pressure solid-liquid phase equilibria in synthetic waxes”, *Phys. Chem. Chem. Phys.*, *4*, 4458-4461, 2002.
- [15] T. Shen, H. Peng, X. Ling, “Experimental Measurements and Thermodynamic Modeling of Melting Temperature of the Binary Systems n-C11H24-n-C14H30, n-C12H26-n-C13H28, n-C12H26-n-C14H30, and n-C13H28-n-C-15 H-32 for Cryogenic Thermal Energy Storage”, *Ind. Eng. Chem. Res.*, *58*, 15026-15035, 2019.
- [16] P.K. Mukherjee and M. Deutsch, “Landau theory of the R-II-R-I-R-V rotator phases of alkanes”, *Phys. Rev. B*, *60*, 3154-3162, 1999.
- [17] C. Ma, Q. Zhou, F. Li, J. Hao, J. Wang, L. Huang, F. Huang, Q. Cui, “Rotator phases of n-heptane under high pressure: Raman scattering and X-ray diffraction studies”, *J. Phys. Chem. C*, *115*, 18310-18345, 2011.
- [18] M. Krishnan, S. Balasubramanian, “n-heptane under pressure: Structure and dynamics from molecular simulations”, *J. Phys. Chem. B*, *109*, 1936-1946, 2005.
- [19] D. Cholakova and N. Denkov, “Rotator phases in alkane systems: In bulk, surface layers and micro/nano-confinements”, *Adv. Colloid Interface Sci.*, *269*, 7-42, 2019.
- [20] B. He, V. Martin, F. Setterwall, “Liquid-solid phase equilibrium study of tetradecane and hexadecane binary mixtures as phase change materials (PCMs) for comfort cooling storage”, *Fluid Phase Equilibria*, *212*, 97-109, 2003.
- [21] M. Milhet, J. Pauly, J.A.P. Coutinho, M. Dirand, J.L. Daridon, “Liquid-solid equilibria under high pressure of tetradecane plus pentadecane and tetradecane plus hexadecane binary systems”, *Fluid Phase Equilibria*, *235*, 173-181, 2005.

- [22] S. Corsetti, T. Rabl, D. McGloin and J. Kiefer, "Intermediate phases during solid to liquid transitions in long-chain n-alkanes", *Phys. Chem. Chem. Phys.*, *19*, 13941-13950, 2017.
- [23] H. Yurtseven, T. Emirosmanglu, O. Tari, "Calculation of the Liquid-Solid Phase Diagram and the Thermodynamic Quantities of the Binary System of Tetradecane and Hexadecane Using the Mean Field Theory", *J. Sol. Chem.*, *50*, 1335-1362, 2021.
- [24] H. Yurtseven, E. Kilit Dogan, "Calculation of the phase diagram of n-alkanes (C_nH_{2n+2}) by the Landau mean field theory", *Fluid Phase Equilibria*, *556*, 113377, 2022.
- [25] O. Tari, H. Yurtseven, "Calculation of the T-X phase diagram of tetradecane+hexadecane and tetradecane+pentadecane under high pressure by the Landau mean field theory", *Fluid Phase Equilibria*, *559*, 113499, 2022.
- [26] H. Yurtseven and O. Tari, "Calculation of the T-X phase diagram and the thermodynamic quantities for the binary mixtures of tetradecane + hexadecane using the Landau mean field model", *Phys. Chem. Liq.*, *61*, 340-364, 2023.
- [27] O. Tari and H. Yurtseven, "Calculation of the phase diagrams (T - X and T - P) and the thermodynamic quantities for the solid - liquid equilibria in n-tridecane", *Int. J. Thermodynamics*, *26*, 37-45, 2023.
- [28] H. Yan, H. Yang, J. Luo, N. Yin, Z. Tan and Q. Shi, "Thermodynamic insights into n-alkanes phase change materials for thermal energy storage", *Chin. Chem. Lett.*, *32*, 3825-3832, 2021.
- [29] S. A. Burrows, I. Korotkin, S.K. Smoukov, E. Boek and S. Karabasov, "Benchmarking of Molecular Dynamics Force Fields for Solid-Liquid and Solid-Solid Phase Transitions in Alkanes", *J. Phys. Chem. B*, *125*, 5145-5159, 2021.
- [30] P.K. Mukherjee, "Effect of silica nanoparticles on the heat capacity of the rotator phase transitions of alkanes", *Phase Transit.*, *95*, 322-330, 2022.
- [31] D. Cholakova, D. Glushkova, Z. Valkova, S. Tsibranska-Gyoreva, K. Tsvetkova, S. Tcholakova and N. Denkov, "Rotator phases in hexadecane emulsion drops revealed by X-ray synchrotron techniques", *J. Colloid Interface Sci.*, *604*, 260-271, 2021.
- [32] P. Morawski, J. A. P. Coutinho, U. Domanska, "High pressure (solid + liquid) equilibria of n-alkane mixtures: experimental results, correlation and prediction", *Fluid Phase Equilibria*, *230*, 72-80, 2005.
- [33] G. Fritsch, "A Landau-type model for the melting transition", *Phys. Stat. Sol. (a)*, *31*, 107-118, 1975.
- [34] C.C. Huang and J.M. Viner, "Nature of the Smectic-A-Smectic-C phase transition in liquid crystals", *Phys. Rev. A*, *25*, 3385-3388, 1982.
- [35] S. Dumrongrattana, G. Nounesis and C.C. Huang, "Measurement of tilt angle and heat capacity in the vicinity of one smectic-A chiral smectic-C transition", *Phys. Rev. A*, *33*, 2181-2183, 1986.
- [36] P.K. Mukherjee, "Simple Landau model of the RIV-RIII-RV rotator phases of alkanes", *J. Chem. Phys.*, *129*, 021101, 2008.
- [37] P.K. Mukherjee, "Tricritical behavior of the RI-RV rotator phase transition in a mixture of alkanes with nanoparticles", *J. Chem. Phys.*, *135*, 134505, 2011.
- [38] P.K. Mukherjee and S. Dey, "Simple Landau Model of the Liquid-RII-RI Rotator Phases of Alkanes". *J. Mod. Phys.*, *3*, 80-84, 2012.
- [39] J.C. Toledano and P. Toledano, "The Landau theory of Phase Transition", World Scientific, Singapore, 1987.
- [40] D. Machon, "Phenomenological theory of the phase diagrams of binary eutectic systems", *Phys. Rev. B*, *71*, 024110, 2005.
- [41] A. Hammami and M. Raines, "Paraffin deposition from crude oils: comparison of laboratory results to field data", *SPE-38776*, 273-287, 1997.
- [42] H. E. Stanley, *Introduction to Phase Transitions and Critical Phenomena*, Clarendon, Oxford, 1971.
- [43] J.J. Binner, N. J. Dowrick, A. J. Fisher, M.E.J. Newman, *The Theory of Critical Phenomena, An Introduction to the Renormalization Group*, Oxford University Press, New York, Chapter 3, 1992.

Research Article

Thermodynamic Modeling of Solubility of Some Antibiotics in Supercritical Carbon Dioxide Using Simplified Equation of State Approach

¹G. Mahesh , ^{2*}C. Garlapati 

¹Department of Chemical Engineering, Birla Institute of Technology and Science (BITS) Pilani, Hyderabad Campus, Jawahar Nagar, Kapra Mandal, Hyderabad 500078, India.

^{2*}Department of Chemical Engineering, Puducherry Technological University (Erstwhile Pondicherry Engineering College), Puducherry 605 014, India.
E-mail: ^{2*}chandrasekhar@ptuniv.edu.in

Received 5 August 2023, Revised 18 November 2023, Accepted 7 January 2024

Abstract

Antibiotics are playing crucial role in the treatment of humans since the last few centuries. Their usage has several benefits along with side effects. The efficacy of antibiotics for the treatment of ailments may be retained by controlling the drug dosage. This may be achieved with supercritical fluid technology (SFT). The antibiotic drug solubility in supercritical carbon dioxide (scCO₂) is available only at specific temperature and pressure conditions, for effective utilization of SFT, solubility at various conditions are required. Equation of state (EoS) method is used for solubility data modeling and it requires critical properties of the solute, molar volume of the solute and sublimation pressure of the solute along with fugacity coefficient, pressure and temperature. These properties are estimated using group contribution methods. For antibiotics solute critical properties, molar volume and sublimation pressure are unavailable and existing group contribution methods are also not applicable due to the lack of functional group contributions in their techniques. Thus, there is a need to address EoS methodology without using solute properties. Hence, a new EoS methodology for solubility modeling is, proposed without using critical properties of the solute, molar volume of the solute and vapour pressure of the solute. Thus, this study focuses on the development of new solubility model that correlates antibiotics using equation of state (EoS). Importantly, the proposed solubility model does not use the critical properties of the antibiotics. Correlating ability of the proposed model is indicated in terms of regression coefficient and arithmetic average relative deviation percentage (AARD %).

Keywords: Antibiotics; equation of state; solubility; supercritical carbon dioxide.

1. Introduction

The use of carbon dioxide as a supercritical solvent has replaced various organic solvents in the pharmaceutical industry [1]. Particle formation steps depend on the ability to quickly change the solvent power of dissolved chemicals and, consequently, the rate of super saturation and nucleation [1-4]. This is possible due to the ease of tuning pressure, physical properties, and the solvent power. Additionally, scCO₂ is a perfect medium for pharmaceutical applications since it has a low critical temperature, is non-toxic and non-flammable, and it leaves the system residue-free after decompression [5,6]. Despite the high expenses involved in processing pharmaceutical compounds under high pressure, which significantly increases the value of the finished goods, this kind of technology is more environmentally friendly because it does not use organic solvents. The creation of new particle micronization techniques has increased over the last few decades, encouraging the implementation of supercritical technology to in the field of pharmaceutical industry [2]. Broadly, micronization techniques fall under two categories, namely, rapid expansion of supercritical saturated solution and its

extended methods as well as supercritical anti solvent process and its extensions [7,8]. These methods involve the creation of a supersaturated solutions which are exploited for crystallisation and thereby particle formation [6,7]. To understand and implement these processes, a thorough knowledge of the solubility of drug solute in the supercritical solvent is essential. But limited data is available only at specified conditions, thus, it is impossible to get experimental data at every desired condition. This creates the need for a good model that represents the solubility. Due to the high non linearity prevailing in the available solubility data, it is difficult to represent data in a single model effectively [9,10]. However, to address this complexity, several frameworks have evolved. Notable frameworks are, phase equilibrium models and density models [10,11,12,13]. Among the phase equilibrium models, Equation of state (EoS) models and expanded liquid models are effective in data correlation. To implement the phase equilibrium models, critical properties of the solute and the solvent are required [10,14,15,16]. Density models are quite simple and require only the pressure, temperature, and density of solvent. If all the

necessary data is available, both the methods perform satisfactorily for several solute-supercritical solvent combinations [10]. Unfortunately, the experimental and group contribution based critical properties of the drug solutes are unavailable [17]. Thus, usage of EoS methods for drug- supercritical solvent systems has become limited. Therefore, in this work, we have proposed a modification to EoS based solubility model that requires only the pressure, temperature, and density of the solvent like that of the density models [18-22]. More details can be seen in the following sections.

2. Modeling

The use of EoS modeling in correlation of solubility of drugs in supercritical carbon dioxide is sought-after in literature. Amongst the several EoSs available, Redlich-Kwong (RK) EoS, Soave-Redlich-Kwong (SRK) EoS and Peng-Robinson (PR) EoS are the vividly used equations of state [23,24]. Amid the three, PR EoS correlates better for the solubility modeling, thus, it is persuaded here [25,26].

2.1 Thermodynamic Modeling

Solubility is expressed as [23,24],

$$y_2 = \frac{p_2^S \hat{\phi}_2^S}{P \hat{\phi}_2^{scF}} \exp \left[\frac{(P-p_2^S)v_2}{RT} \right] \quad (1)$$

where the parameters have their usual definitions, the subscript 2 stands for the solute. For modeling, fugacity coefficient at saturation for the solid is assumed unity. $\hat{\phi}_2^{scf}$ is evaluated with PR EoS with the following thermodynamic relation as [20,21].

$$\ln(\hat{\phi}_2^{scf}) = \frac{1}{RT} \int_v^\infty \left[\left(\frac{\partial P}{\partial n_2} \right)_{T,v,n_1} - \frac{RT}{v} \right] dv - \ln(Z) \quad (2)$$

The obtained fugacity coefficient is

$$\ln(\hat{\phi}_2^{scf}) = \frac{\hat{b}}{b} (Z-1) - \ln \left(Z \left(1 - \frac{b}{v} \right) \right) + \frac{a}{2\sqrt{2}RT} \left[\frac{\hat{a}}{a} - \frac{\hat{b}}{b} \right] \ln \left(\frac{Z - 0.414b}{Z + 2.414b} \right) \quad (3)$$

vdW mixing rules are

$$a_{12} = (1 - k_{12}) \sqrt{a_{11} a_{22}} \quad (4)$$

$$b_{12} = (1 - l_{12}) \left(\frac{b_{11} + b_{22}}{2} \right) \quad (5)$$

The equations (1) and (5) are combined for the solubility evaluation as

$$y_2 = f(a_1, b_1, a_2, b_2, P, T, p_2^S, \hat{\phi}_2^{scf}, k_{12}, l_{12}) \quad (6)$$

More details about PREoS and vdW mixing rules is reported in literature [23,24]. The major limitations in evaluating equation (6) lie in the determination of critical properties, molar volume, and the sublimation pressure of the antibiotics (solute). These properties are estimated using group contribution methods. For antibiotics (solute) critical

properties, molar volume and sublimation pressure are unavailable and existing group contribution methods are also not applicable due to the lack of functional group contributions in their techniques [23]. Thus, there is a need to address EoS methodology without using solute properties. Hence, a new methodology in EoS frame work is inevitable. The following subsection deals with the new methodology and it can be used for any EoS along with suitable mixing rules.

2.2 New Methodology

The limitations mentioned in section 2.1 may be subjugated by treating the solute's parameters a_2 and b_2 as adjustable constants (keeping k_{12}, l_{12} as zero), replacing sublimation pressure with suitable temperature function, $f(T)$ (as it is a function of temperature), replacing molar volume of the drug with the suitable scCO₂ density function, $g(\rho_1)$ (since it can be expressed as a function of solvent density) and replacing $\hat{\phi}_2^{scf}$ estimated at infinite dilution with $\hat{\phi}_2^\infty$ [25-27]. Thus, the solubility expression is

$$y_2 = \frac{f(T)}{P \hat{\phi}_2^\infty} \exp \left(\frac{(P - f(T))g(\rho_1)}{RT} \right) \quad (7)$$

where, $f(T) = \exp(A - B/T)$; $g(\rho_1) = \exp(C \ln(\rho_1) + D)$

Optimization is done with the following objective function eq.(8) [25]

$$OF = \sum_{i=1}^N \left| \frac{y_{2i}^{\text{exp}} - y_{2i}^{\text{cal}}}{y_{2i}^{\text{exp}}} \right| \quad (8)$$

where N is the number of solubility data points. Evaluation was carried in MATLAB® platform with the help of built in function (*fminsearch*) that uses Nelder-Mead algorithm. The adjustable parameters in the solubility model are a_2, b_2, A, B, C and D . This study can be used conveniently when solute's properties such as molar volume, critical properties, and sublimation pressure are unavailable.

3. Results and Discussion

In this work, fourteen antibiotics' belonging to different classes with their solubilities in scCO₂ were considered [29-37]. These drugs are proved to be highly beneficial in the treatment of several ailments. On the other hand, these drugs have adverse effects too. The details of the drugs, their classes, chemical formulae, molecular structure along with their adverse effects are mentioned in the literature. The solubility, temperature, and pressure ranges for all the drugs considered in the study are shown in table 1. The proposed new methodology resulted in a simplified EoS solubility model (eq.7) and it is evaluated using an objective function (eq.8) with PREoS and vdW mixing rules without binary interaction parameters. The correlation constants are given in the table 2. The correlation results are quantified with statistical parameters namely square of coefficient of regression (R²) and absolute average relative deviation (AARD). The correlation results also provide information about the molar volume of the solute and sublimation pressure and they are presented in the table 3 and 4 respectively. Molar volume of the solute is calculated with $v_2 = \exp(C \ln(\rho_1) + D)$ and the sublimation pressure is calculated with $\ln(p_2^S) = A - B/T$. Figures 1-14 show the

correlating ability of the proposed EoS model for all the drug compounds considered in the work. It is evident that the correlating ability of the proposed method is good for seven systems namely Amoxicilin-scCO₂, ciprofloxacin-scCO₂, clarithromycin-scCO₂, clemastine fumarate-scCO₂, enrofloxacin-scCO₂, gatifloxacin-scCO₂ and penicillin V-scCO₂. For all these systems the corresponding R² values are more than 0.95 thus, they are considered as correlated well. For remaining 7 systems the R² values are less than 0.95 thus they are considered as poorly correlated. However, in terms of AARD % the error are in the range between 4.78- 25.1 for compounds considered in the study.

Table 1. Details of Antibiotic-scCO₂ systems.

Solute-Solvent[Ref]	T range K	P range bar	y ₂ range 10 ⁶
Amoxicilin-scCO ₂ [32]	308.15-338.15	160-400	10.8-7230
Azithromycin-scCO ₂ [33]	308-348	122-355	69-273
Cefuroxime Axetil-scCO ₂ [29]	308-328	80-250	0.22-11.2
Ciprofloxacin-scCO ₂ [37]	313-333	120-360	0.0265-0.189
Clarithromycin-scCO ₂ [33]	308-348	122-355	131-328
Clemastine Fumarate-scCO ₂ [36]	308-338	120-270	1.61-9.41
Clindamycin-scCO ₂ [33]	308-348	122-355	177-1146
Enrofloxacin-scCO ₂ [37]	313-333	120-360	0.061-5.61
Erythromycin-scCO ₂ [33]	308-348	122-355	54-312
Gatifloxacin-scCO ₂ [37]	313-333	120-360	0.106-1.61
Metronidazole Benzoate-scCO ₂ [35]	308-348	122-355	70-4550
Naproxen-scCO ₂ [35]	308-348	122-355	10-120
Penicillin G-scCO ₂ [30]	313.15-333.15	100-350	4.2-63.3
Penicillin V-scCO ₂ [31]	314.15-334.15	80.76-280.45	54.5-576

Table 2. Correlation parameters.

Solute-Solvent	Correlation parameters a ₂ , b ₂ , A, B, C, D, R ² , AARD%
Amoxicilin-scCO ₂	1.9816×10 ⁻³ ; 2.5422×10 ⁻³ ; 58.604; 39417; 0.36186; -8.3132; 0.987; 18.6.
Azithromycin-scCO ₂	1.9708×10 ⁻⁴ ; 3.1006×10 ⁻⁴ ; 14.422; 4621.2; 0.29283; -9.7727; 0.953; 5.94.
Cefuroxime Axetil-scCO ₂	7.6968×10 ⁻⁴ ; 1.3046×10 ⁻³ ; -15.049; 6672.7; -0.30725; -4.1811; 0.992; 2.51.
Ciprofloxacin-scCO ₂	2.1401×10 ⁻³ ; 5.3582×10 ⁻⁴ ; 17.654; 8733.4e+03; 0.32084; -10.688; 0.971; 8.72.
Clarithromycin-scCO ₂	9.4354×10 ⁻⁵ ; 2.3627×10 ⁻⁴ ; 14.159; 3778.9; 0.48557; -11.257e+01; 0.944; 4.78.
Clemastine Fumarate-scCO ₂	1.0560×10 ⁻⁴ ; 1.5823×10 ⁻⁴ ; 14.579; 4718.6; 0.48706; -11.139e+01; 0.945; 7.32.
Clindamycin-scCO ₂	2.5866×10 ⁻⁴ ; 3.3511×10 ⁻⁴ ; 20.7; 6480.8; 0.53272; -11.346e+01; 0.93; 10.8.
Enrofloxacin-scCO ₂	1.6022×10 ⁻³ ; 2.3258×10 ⁻³ ; -11.509; 17995; 0.43952; -2.8189; 0.971; 9.04
Erythromycin-scCO ₂	4.7026×10 ⁻⁵ ; 3.7179×10 ⁻⁴ ; 16.484; 6243.7; 0.32607; -9.6460; 0.924; 12.2.
Gatifloxacin-scCO ₂	3.7132×10 ⁻⁴ ; 9.1555×10 ⁻⁴ ;

	1.7970; 9276.6; -0.527; -2.9693; 0.964; 9.42
Metronidazole Benzoate-scCO ₂	2.2778×10 ⁻⁴ ; 9.1954×10 ⁻⁴ ; 2.4213; 7480.8; 0.53416; -2.8445; 0.85; 19.5
Naproxen-scCO ₂	6.1199×10 ⁻⁵ ; 7.0094×10 ⁻⁴ ; 1.1112; 6124.1; 0.66991; -2.0872; 0.918; 12.7
Penicillin G-scCO ₂	6.7693×10 ⁻⁴ ; 3.2338×10 ⁻⁴ ; 21.066; 7325.8; 0.52116; -11.379; 0.935; 21.9
Penicillin V-scCO ₂	4.8247×10 ⁻⁴ ; 2.9869×10 ⁻⁴ ; 17.927; 4971.4; 1.0657; -15.302; 0.989; 5.65

Table 3. Computed solid drug average molar volume.

Drug	Molar volumem ³ /mol
Amoxicilin	2.84×10 ⁻³
Azithromycin	4.05×10 ⁻⁴
Cefuroxime Axetil	1.95×10 ⁻³
Ciprofloxacin	2.00×10 ⁻⁴
Clarithromycin	3.34×10 ⁻⁴
Clemastine Fumarate	3.73×10 ⁻⁴
Clindamycin	4.19×10 ⁻⁴
Enrofloxacin	3.05×10 ⁻³
Erythromycin	5.75×10 ⁻⁴
Gatifloxacin	1.45×10 ⁻³
Metronidazole Benzoate	1.62×10 ⁻³
Naproxen	1.40×10 ⁻³
Penicillin G	3.88×10 ⁻⁴
Penicillin V	2.83×10 ⁻⁴

Table 4. Computed drug vapour pressure.

Drug	Sublimation pressure expression, ln(p ₂ ^s) is
Amoxicilin	58.604 – 39417/T
Azithromycin	14.422 – 4621.2/T
Cefuroxime Axetil	-15.049 – 6672.7/T
Ciprofloxacin	17.654 – 8733.4/T
Clarithromycin	14.159 – 4718.6/T
Clemastine Fumarate	14.579 – 4718.6/T
Clindamycin	20.7 – 6480.8/T
Enrofloxacin	-11.509 – 17995/T
Erythromycin	16.484 – 6243.7/T
Gatifloxacin	1.797 – 9276.6/T
Metronidazole Benzoate	2.4213 – 7480.8/T
Naproxen	1.1112 – 6124.1/T
Penicillin G	21.066 – 7325.8/T
Penicillin V	17.927 – 4971.4/T

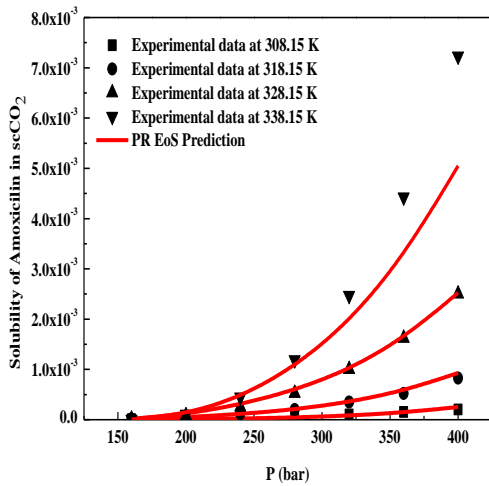


Figure 1. Solubility of Amoxicilin in $scCO_2$, y_2 vs P . Symbols are experimental data points from literature [32]. Lines are PR EoS model prediction.

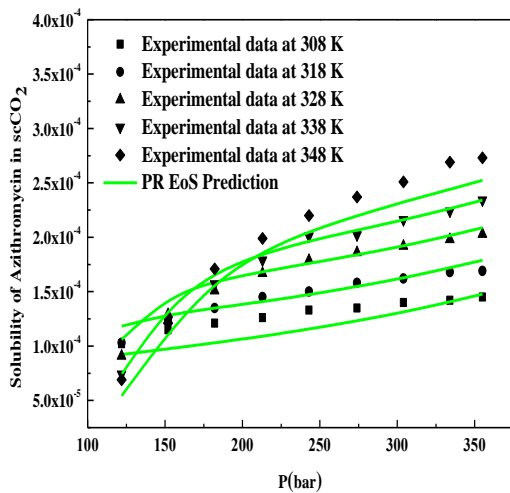


Figure 2. Solubility of Azithromycin in $scCO_2$, y_2 vs P . Symbols are experimental data points from literature [33]. Lines are PR EoS model prediction.

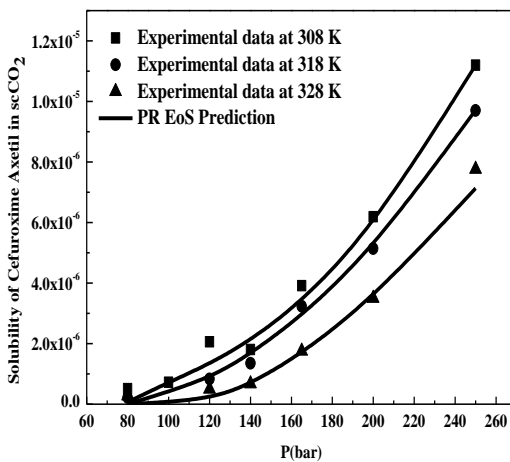


Figure 3. Solubility of Cefuroxime Axetil in $scCO_2$, y_2 vs P . Symbols are experimental data points from literature [29]. Lines are PR EoS model prediction.

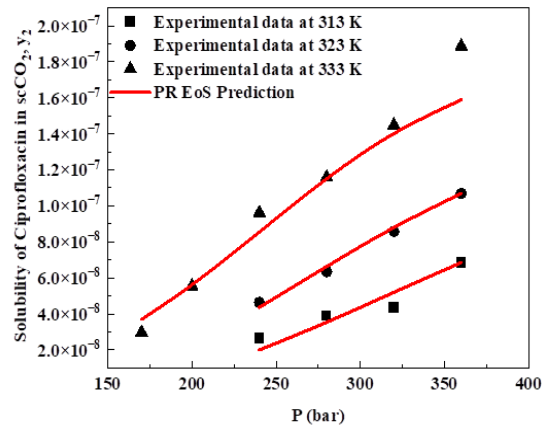


Figure 4. Solubility of Ciprofloxacin in $scCO_2$, y_2 vs P . Symbols are experimental data points from literature [37]. Lines are PR EoS model prediction.

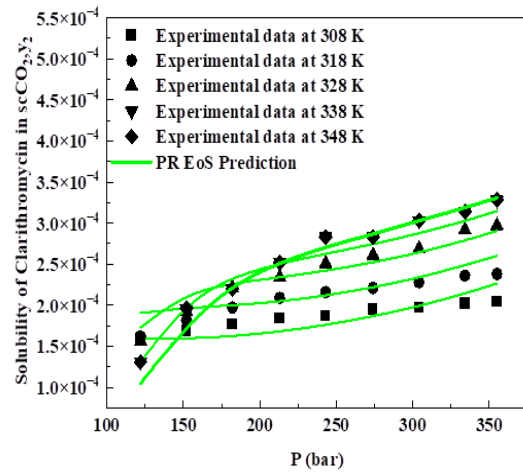


Figure 5. Solubility of Clarithromycin in $scCO_2$, y_2 vs P . Symbols are experimental data points from literature [33]. Lines are PR EoS model prediction.

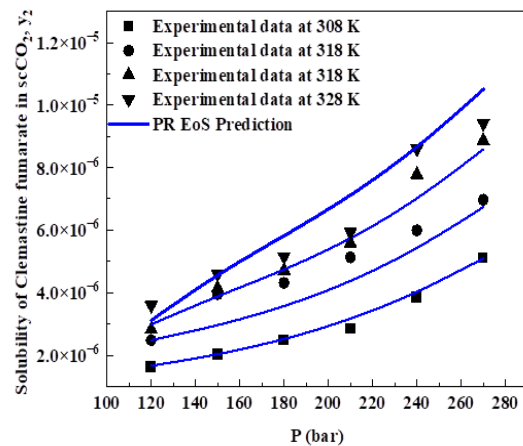


Figure 6. Solubility of Clemastine fumarate in $scCO_2$, y_2 vs P . Symbols are experimental data points from literature [33]. Lines are PR EoS model prediction.

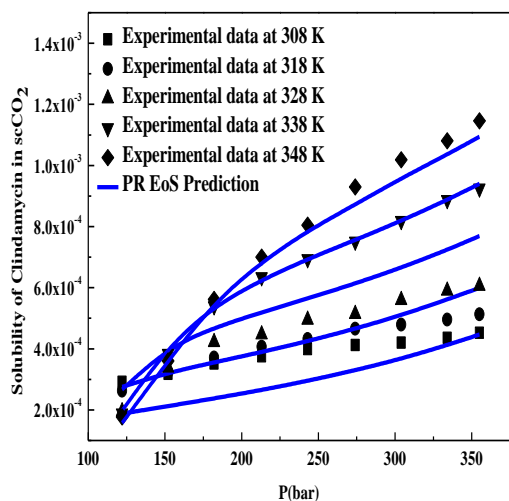


Figure 7. Solubility of Clindamycin in $scCO_2, y_2$ vs P . Symbols are experimental data points from literature [33]. Lines are PR EoS model prediction.

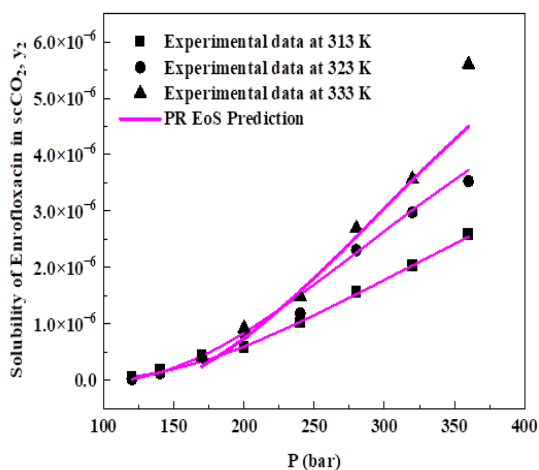


Figure 8. Solubility of Enrofloxacin in $scCO_2, y_2$ vs P . Symbols are experimental data points from literature [34]. Lines are PR EoS model prediction.

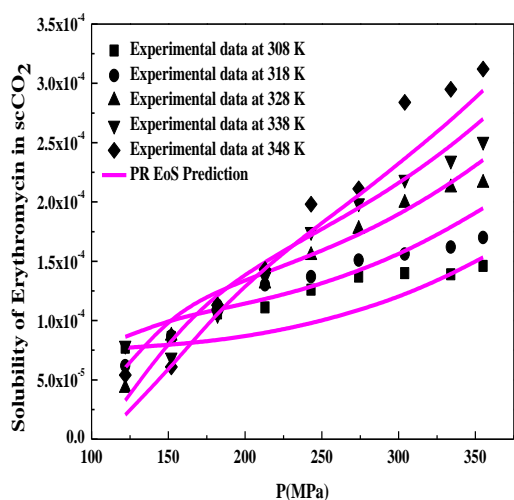


Figure 9. Solubility of Erythromycin in $scCO_2, y_2$ vs P . Symbols are experimental data points from literature [34]. Lines are PR EoS model prediction.

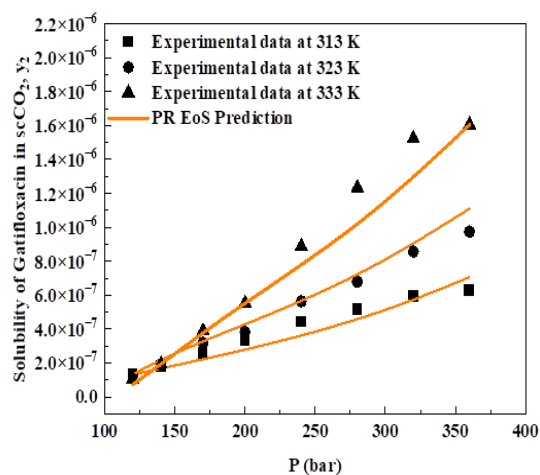


Figure 10. Solubility of Gatifloxacin in $scCO_2, y_2$ vs P . Symbols are experimental data points from literature [34]. Lines are PR EoS model prediction.

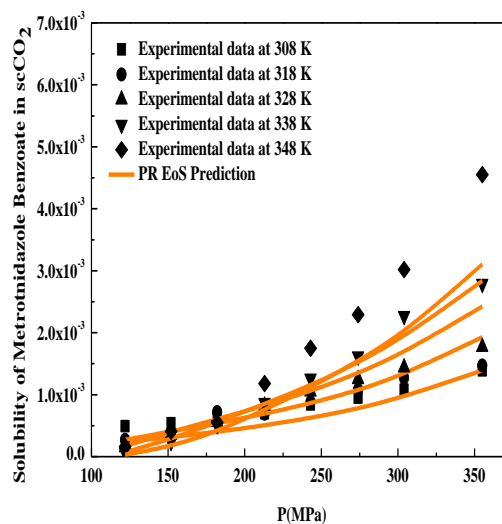


Figure 11. Solubility of Metronidazole Benzoate in $scCO_2, y_2$ vs P . Symbols are experimental data points from literature [30]. Lines are PR EoS model prediction.

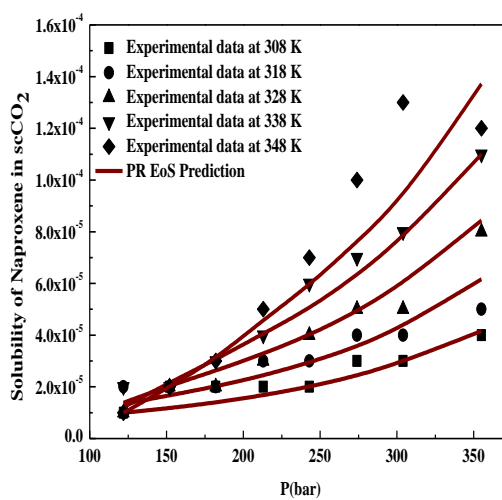


Figure 12. Solubility of Naproxene V in $scCO_2, y_2$ vs P . Symbols are experimental data points from literature [28]. Lines are PR EoS model prediction.

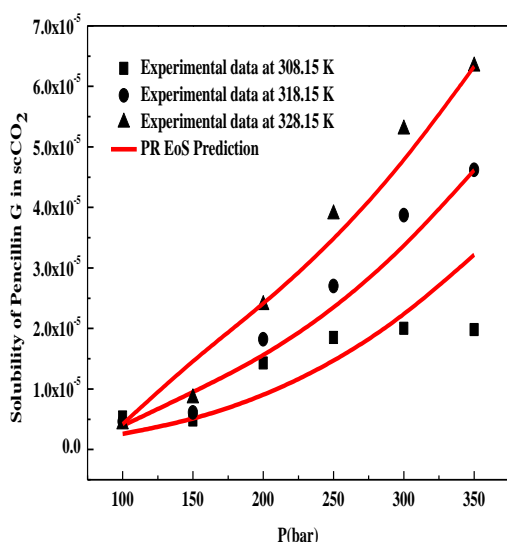


Figure 13. Solubility of Penicillin G in $scCO_2$, y_2 vs P . Symbols are experimental data points from literature [28]. Lines are PR EoS model prediction.

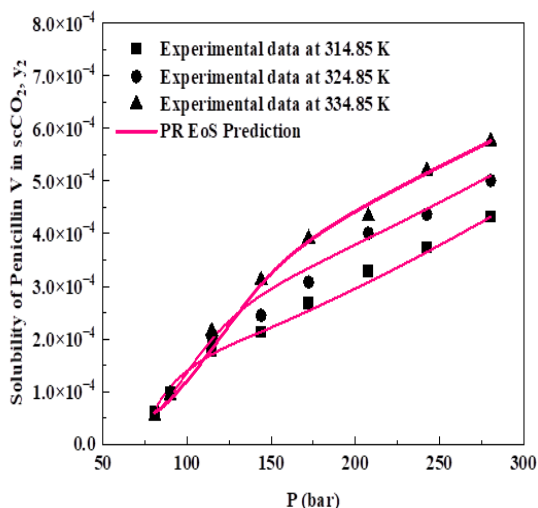


Figure 14. Solubility of Penicillin V in $scCO_2$, y_2 vs P . Symbols are experimental data points from literature [28]. Lines are PR EoS model prediction.

4. Conclusion

In this work, a simplified solubility model is proposed based on EoS as a function of pressure, temperature and density of $scCO_2$, which resembles density models. The proposed model is validated with the solubility data of fourteen antibiotics in supercritical carbon dioxide and it is observed to fit data with AARD % ranging between 4.78-25.1 %. Clarithromycin and cefuroximeaxetil are observed to have the least and the highest AARD % respectively. Sublimation pressures and solute molar volume were also computed for all the drugs.

Acknowledgements:

Corresponding Author (Prof. Dr. Chandrasekhar Garlapati) would like to thank Prof. Dr. Giridhar Madras, Department of Chemical Engineering, IIT Hyderabad, Telangana, India for the inspiration and support.

Nomenclatures

a – PREoS parameter ($J\ m^3\ mol^{-1}$)
 A – Vapour pressure parameter (bar)
 b – PREoS parameter (m^3/mol)
 B – Vapour pressure parameter
 C – Molar volume parameter
 D – Molar volume parameter
 f – Vapor pressure function
 g - Solute molar volume function
 n - Moles
 N – Total data points
 P – Total pressure (bar)
 p – Sublimation pressure
 R – Gas constant ($J\ mol^{-1}\ K^{-1}$)
 T – Temperature (K)
 v - Molar volume (m^3/mol)
 y – Mole fraction
 Z – Compressibility factor
 Greek letters
 $\hat{\phi}$ – Fugacity coefficient
 ρ – density ($kg\ m^{-3}$)
 Subscript and superscript
 1 – Solvent
 2 – Solute
 $scCO_2$ – Supercritical carbon dioxide
 exp - Experimental
 calc - Calculated
 ∞ - Infinite

References:

- [1] A. Tabernero, E. M. del Valle and M. A. Galán, “Supercritical fluids for pharmaceutical particle engineering: Methods, basic fundamentals and modelling,” *Chem. Eng. Process*, vol. 60, pp. 9-25, October 2012. doi:10.1016/j.cep.2012.06.004.
- [2] B. Subramaniam, R.A. Rajewski and K. Snavely, “Pharmaceutical processing with supercritical carbon dioxide,” *J. Pharm.Sci.* vol. 86, no. 8, pp. 885-890, August 1997. doi:10.1021/js9700661.
- [3] M. Mukhopadhyay, “Partial molar volume reduction of solvent for solute crystallization using carbon dioxide as antisolvent,” *J Supercrit Fluids*, vol. 25, no. 3, pp. 213-223, April 2003. doi:10.1016/S0896-8446(02)00147-X.
- [4] N. Elvassore, I. Kikic, “Pharmaceutical processing with supercritical fluids,” In *High Pressure Process Technology: Fundamentals and Applications*, A. Bertucci, A. Better (Ed.) Elsevier Science, 2001, pp 612-625.
- [5] R. B. Gupta and P. Chattopadhyay, “Method of forming nanoparticles and microparticles of controllable size using supercritical fluids and ultrasound,” US pat., 20020000681, March 2002.
- [6] E. Reverchon, R. Adami, G. Caputo and I. de marco, “spherical microparticles production by supercritical antisolvent precipitation: Interpretation of results,” *J. Supercrit Fluids*, vol. 47, no. 1, pp. 70-84, November 2008. doi:10.1016/j.supflu.2008.06.002.
- [7] G. Sodeifian, S. A. Sajadian, N. S. Ardestani and F. Razmimanesh, “Production of Loratadine Drug Nanoparticles Using Ultrasonic-Assisted Rapid Expansion of Supercritical Solution into Aqueous

- Solution (US-RESSAS),” *J Supercrit Fluids*, vol. 147, pp. 241-253, May 2019. doi:10.1016/j.supflu.2018.11.007.
- [8] J. F. Brennecke and C. A. Eckert, “Phase equilibria for supercritical fluid process design,” *AIChE Journal*, vol. 35, no. 9, pp. 1409-1427, September 1989. doi:10.1002/aic.690350902.
- [9] G. Mahesh and C. Garlapati, “Modelling of solubility of some parabens in supercritical carbon dioxide and new correlations,” *Arab. J. Sci. Eng.*, vol. 47, pp. 5533-5545, May 2022. doi:10.1007/s13369-021-05500-2.
- [10] T.A. Reddy and C. Garlapati, “Dimensionless Empirical Model to Correlate Pharmaceutical Compound Solubility in Supercritical Carbon Dioxide,” *Chem. Eng. Technol.* vol. 42, no. 12, pp. 2621–2630, December 2019. doi:10.1002/ceat.201900283.
- [11] P.Subra, S. Castellani, H. Ksibi and Y. Garrabos,” Contribution to the determination of the solubility of β -carotene in supercritical carbon dioxide and nitrous oxide: experimental data and modeling,” *Fluid Phase Equilib.* vol. 131, no. 1-2, pp. 269-286, May 1997.
- [12] R. Hartono, G. A. Mansoori and A. Suwono, “Prediction of solubility of biomolecules in supercritical solvents” *Chem. Eng. Sci.* vol. 56, no. 24, pp. 6949-6958, December 2001, doi:10.1016/S0009-2509(01)00327-X.
- [13] A. Issaoui, A. B. Moussa and H. Ksibi, “Correlation of the binary interaction factor for polar solutes dissolved in supercritical carbon dioxide” *In. J. of Thermodynamics*, vol. 14, no. 1, pp. 37-42, March 2011, doi:10.5541/ijot.342.
- [14] R. S. Alwi and C. Garlapati, “New correlations for the solubility of anticancer drugs in supercritical carbon dioxide,” *Chem.Pap.* vol. 76, no. 3, pp. 1385–1399, March 2022. doi:10.1007/s11696-021-01943-x .
- [15] G. Sodeifian, C. Garlapati , F. Razmimanesh and H. Nateghi. “Experimental solubility and thermodynamic modelling of empagliflozin in Supercritical Carbon Dioxide,” *Sci. Rep.* vol. 12, no. 9008, May 2022. doi:10.1038/s41598-022-12769-2
- [16] G. Sodeifian ,C. Garlapati , S. M. Hazaveie and F Sodeifian, “Solubility of 2,4,7-Triamino-6-phenylpteridine (Triamterene, Diuretic Drug) in supercritical carbon dioxide: Experimental data and modeling,” *J. Chem. Eng. Data* vol. 65, no. 9, pp. 4406-4416, August 2020. doi:10.1021/acs.jced.0c00268
- [17] G. Sodeifian, C. Garlapati, F. Razmimanesh, H. Nateghi, “Solubility measurement and thermodynamic modelling of Pantoprazole sodium sesquihydrate in supercritical carbon dioxide,” *Sci. Rep.* vol. 12, no. 7758, May 2022. doi:10.1038/s4159-022-11887-1.
- [18] X. Bian, Z. Du, Y. Tang, “An improved density-based model for the solubility of some compounds in supercritical carbon dioxide,” *Thermochimica Acta*, vol. 519, no.1-2, pp. 16-21, May 2011. doi:10.1016/j.tca.2011.02.023.
- [19] C. Garlapati, G. Madras, “Solubilities of Some Chlorophenols in Supercritical CO₂ in the Presence and Absence of Cosolvents,” *J. Chem. Eng.Data.* vol. 55, no.1, pp. 273-277, January 2010, doi:10.1021/je900328c.
- [20] C. Garlapati, G. Madras, “New empirical expressions to correlate solubilities of solids in supercritical carbon dioxide,” *Thermochimica Acta*, vol. 500, no.1-2, pp. 123-127, March 2010. doi:10.1016/j.tca.2009.12.004.
- [21] J. Chrastil, “Solubility of solids and liquids in supercritical gases, *J.Phys.Chem.*,” vol. 86, no.15, pp. 3016-3021, July 1982. doi:10.1021/j100212a041.
- [22] K. D. Bartle, A. A. Clifford, S. A. Jafar and G. F. Shilstone, “Solubilities of Solids and Liquids of Low Volatility in Supercritical Carbon Dioxide,” *J. Phys. Chem. Ref. Data*, vol. 20, no. 4, pp.713-756, July 1991. doi:10.1063/1.555893.
- [23] J. M. Prausnitz, R. N. Lichtenthaler and E. G. de Azevedo, *Molecular thermodynamics of fluid-phase equilibria*, 3rd Ed, New York:Pearson Education, 1998.
- [24] H. Orbey and S.I. Sandler, *Modeling Vapor-Liquid Equilibria: Cubic Equations of State and Their Mixing Rules*, New York: Cambridge University Press, 1998.
- [25] W. J. Schmitt and R. C. Reid, “Solubility of monofunctional organic solids in chemically diverse supercritical fluids,” *J. Chem. Eng. Data*, vol. 31, no. 2, pp. 204-212, April 1986. doi:10.1021/je00044a021.
- [26] L. A. Estévez, F. J. Colpas and E. A. Müller. “A Simple Thermodynamic Model for the Solubility of Thermolabile Solids in Supercritical Fluids,” *Chem. Eng. Sci.* vol. 232, no.116268, March 2021. doi:10.1016/j.ces.2020.116268.
- [27] Y. Iwai, Y. Koga, T. Fukuda and Y. Arai, “Correlation of Solubilities of High-Boiling Components in supercritical carbon dioxide,” *J. Chem. Eng. Jpn.* vol. 25, no. 6 pp.757–760, April 1992. doi: 10.1252/jcej.25.757.
- [28] J. O. Valderrama and V. H. Alvarez. “Correct Way of Reporting Results when Modelling Supercritical Phase Equilibria using Equations of State,” *Can. J. Chem. Eng.* vol. 83, no. 3, pp. 578-581, May 2005. doi:10.1002/cjce.5450830323.
- [29] K. Ongkasin *et al.*, “Solubility of cefuroxime axetil in supercritical CO₂: Measurement and modelling,” *J Supercrit Fluids*, vol. 152, p.104498, October 2019. doi: 10.1016/j.supflu.2019.03.010.
- [30] M.D. Gordillo, M.A. Blanco, A. Molero and E. Martinez de la Ossa, “Solubility of the antibiotic Penicillin G in supercritical carbon dioxide,” *J Supercrit Fluids* vol.15, no.3, pp.183–190, July 1999. doi:10.1016/S0896-8446(99)00008-X.
- [31] M. Ko, V. Shah, P. R. Bienkowski and H. D. Cochran, “Solubility of the antibiotic penicillin V in supercritical CO₂,” *J Supercrit Fluids*, vol. 4, no.1, pp. 32-39, March 1991. doi:10.1016/0896-8446 (91) 900 28-5.
- [32] M. A. Sabegh, H. Rajaei, A. Z. Hezave and F. Esmailzadeh, “Amoxicillin Solubility and Supercritical Carbon Dioxide,” *J. Chem. Eng. Data*, vol. 57, no. 10 ,pp. 2750–2755, September 2012. doi:10.1021/je3006826.

- [33] H. Asiabi, Y. Yamini, F. Latifeh and A. Vatanara, "Solubilities of four macrolide antibiotics in supercritical carbon dioxide and their correlations using semi-empirical models," *J. Supercrit. fluids.* vol.104, pp. 62-69, September 2015. doi:10.1016/j.supflu.2015.05.018.
- [34] C. Garlapati, G. Madras, "Temperature independent mixing rules to correlate the solubilities of antibiotics and anti-inflammatory drugs in SCCO₂," *Thermochimica Acta* vol. 496, no.1-2, pp. 54–58, December 2009. doi:10.1016/j.tca.2009.06.022.
- [35] A. Garmroodi, J. Hassan and Y. Yamini, "Solubilities of the Drugs Benzocaine, Metronidazole Benzoate, and Naproxen in Supercritical Carbon Dioxide," *J. Chem. Eng. Data* vol. 49, no. 3, pp.709-712, April 2004. doi: 10.1021/je020218w.
- [36] G. Sodeifan, C. Garlapati, F. Razmimanesh, M. Ghanaat Ghamsari, "Measurement and modeling of clemastine fumarate (antihistamine drug) solubility in supercritical carbon dioxide," *Sci. Rep.* vol.11, no. 24344, December 2021. doi:10.1038/s41598-021-03596-y.
- [37] K. Shi, L. Feng, L. He and H. Li, "Solubility determination and correlation of Gatifloxacin, Enrofloxacin, and Ciprofloxacin in supercritical CO₂," *J. Chem. Eng. Data*, vol. 62, no.12, pp.4235-4243, November 2017. doi:10.1021/acs.jced7b00601.